Thermal Characterization of High-Power Diode Lasers Using Thermoreflectance

by

Aman Kumar Jha

A dissertation submitted in partial fulfillment
of the requirements for the degree of
Doctor of Philosophy
(Mechanical Engineering)
in The University of Michigan
2021

Doctoral Committee:

Professor Kevin P. Pipe, Chair
Professor Pallab K. Bhattacharya
Dr. Robert J. Deri, Lawrence Livermore National Lab
Professor Katsuo Kurabayashi
Dr. Paul O. Leisher, Freedom Photonics LLC

Aman Kumar Jha
amankj@umich.edu
ORCID iD: 0000-0001-8078-4439

Dedication

To my parents and sisters.

Acknowledgments

The work presented in this thesis would not have been possible without contributions from several people to whom I am deeply indebted. First and foremost, I would like to thank my research advisor Prof. Kevin Pipe. I joined Kevin's lab as a master's student in September 2016. Although my knowledge in the fields of solid-state physics and thermal sciences was very limited at the time, Kevin graciously agreed to advise me as part of a research-based course. Since then Kevin has provided me with invaluable advice regarding research, classes, and career. Kevin's ability to explain complicated concepts in a clear and concise way, and his ingenious approach to thinking about problems, have guided and inspired me throughout my time at Michigan.

I am also extremely thankful to Dr. Paul Leisher and Dr. Robert Deri. As our collaborators from the Lawrence Livermore National Lab, they shared their vast knowledge and insights which kept me on track and made this thesis possible. Our weekly meetings were essentially brainstorming sessions where we discussed problems ranging in their impact from trivial to catastrophic, and I left each meeting a little more knowledgeable than I was before. They created an atmosphere which was conducive for such discussions and I never had to worry about sharing results which showed a lack of progress. It was a privilege to work under their guidance.

I would also like to thank my fellow lab mates in Kevin's lab. Chen Li was the first person who I worked with on the laser project, and he explained the concepts of laser physics, thermoreflectance and lab work to me with infinite patience. We spent countless hours working in the lab and I learnt a lot from him. I also enjoyed working with Connie Lee on a variety of projects which never made it to this thesis but taught me a lot, nevertheless. It was an absolute pleasure working with Connie. I would also like to thank Shantonio Birch who helped me out with an experiment when I had totally lost hope of getting any good results. I will miss our long-winded discussions on organic charge transport phenomena and the amazing potlucks with the best Chinese food I've ever had. Luyang Wang recently joined our lab and I have really enjoyed working with him. I also worked closely with Vahid Rashidi and Da Seul Yang and learnt a great deal from them. I could not have asked for a better set of people to work with.

I must thank all my friends for their unwavering support and belief in me. They made this journey so much easier and enjoyable. There are too many to name, but each one of you was crucial and I truly appreciate all of you. I would like to express my deep love and gratitude to my parents, Anjani Kumar Jha and Nisha Jha, and to my sisters, Ankita and Arpana, who first motivated me to join the doctoral program and then stood by me through all the tough times.

Thank you for your unconditional love and support, and for believing in me and my decisions. I am truly blessed to have you all as my family.

TABLE OF CONTENTS

LIST OF FIGURES

FIGURE

LIST OF TABLES

TABLE

ABSTRACT

Optoelectronic devices are pervasive in our daily lives and have seen incredible progress in recent years leading to significant improvements in efficiency and applicability. Temperature is an important parameter which dictates the performance, lifetime and reliability of optoelectronic devices. As these devices scale to smaller sizes, the impact of heating becomes increasingly severe while the measurement of thermal properties becomes challenging. Thermal considerations are particularly important for modern high-power diode lasers which have found widespread use in materials processing and as pump sources in high energy laser systems.

In this work, we show how CCD camera-based thermoreflectance temperature measurements can be successfully applied to characterize the thermal response of high-power diode lasers with high spatial and temperature resolution. Diode lasers can undergo thermal failure through several different routes. One of the primary routes to diode laser failure is through absorption of light at the outcoupling facet. Here we have explored two ways through which light absorption occurs at the facet: back-reflection of laser emission onto the facet and the absorption of outgoing emission within the active region at the facet.

Back-reflection (back-irradiance) of laser emission onto the facets of high-power diode lasers is a known consequence of the deployment of these devices in some diode-pumped laser systems and is known to accelerate device failure. We use thermoreflectance imaging to measure the temperature rise near the quantum well at the facet, for diode lasers emitting at several wavelengths, and for a wide range of back-irradiance beam positions. We find that two critical locations exist on the diode laser facet within a few microns of the epitaxial layers, such that when the back-irradiance is positioned at these locations, it leads to a peak in the temperature rise near the quantum well.

With $\sim 7.5\%$ optical feedback positioned at a critical location, the active region temperatures at the facet were found to be nearly three times higher compared to the no back-irradiance case at the rated current. Moreover, these critical locations are found to be a function of the device emission wavelength and polarization. It was found that for GaAs-based diode lasers, TM-polarized devices emitting around 800 nm are the most susceptible to back-irradiance induced failure while TE-polarized devices emitting around 1000 nm are the most robust.

Under regular operation, the maximum optical power of high-power diode lasers is primarily limited by catastrophic optical mirror damage which refers to the damage caused to the outcoupling facet triggered by severe surface heating at a high injection current. The surface heating is believed to be caused primarily by non-radiative recombination of carriers generated by partial absorption of outgoing emission at the facet. We devised a technique to quantify the degree of this absorption using a combination of thermoreflectance imaging and a heat transport model of the chip. Using this technique, we carried out device degradation studies for diode lasers by analyzing the change in facet optical absorption with device age across a range of emission wavelengths and facet passivation conditions. We found that the facet absorption more than doubled after 200 hours of aging for all devices under test. The non-passivated devices exhibited a small decrease in facet absorption after further 200 hours of aging which suggests that facet degradation is rapid over the first few hundred hours and saturates thereafter. Passivated devices exhibited four times lower facet absorption compared to the non-passivated devices.

High-power diode lasers also undergo gradual degradation primarily through point defect creation and migration which leads to a slow decline in the output power. In our efforts to better understand the dynamics of device degradation with aging, we measured detailed two-dimensional thermal maps of the active region of these devices at the facet for a wide range of operating currents as the device ages. These maps were found to exhibit high repeatability, fine spatial structure, and large thermal gradients which result from a complex interplay between current distribution, optical emission profile and defect density distribution at the facet and within the cavity. We analyzed the detailed thermal profiles and their evolution at high temporal granularity as the device ages. The

mean temperature rise at the facet nearly doubles after 200 hours of operation at the rated current. Moreover, the temperature distribution was found to be highly non-uniform along the slow axis with large temperature gradients of $\sim$ 1.3 K/μm and local temperature spikes with characteristic widths of $\sim$ 5 μm. The non-uniformity in temperature distribution was found to grow with device age as evidenced by a three-fold increase in the standard deviation of temperature for operating currents larger than 3 A, after 200 hours of aging. The size and position of local temperature spikes were found to depend strongly on the operating current and correlate to a small degree with the optical intensity profile.

CHAPTER 1

Introduction

1.1 Thermal Challenges in Optoelectronic Devices

Optoelectronic devices such as LEDs, OLEDs and diode lasers are ubiquitous in our daily lives with applications in general lighting, display systems, fiber-optic communication, barcode readers, sensors and medical devices. Recent advancements in epitaxial design, thin film growth and nanofabrication technologies have resulted in devices emitting over a wide range of wavelengths, with ever smaller dimensions alongside a dramatic increase in the efficiency and maximum output power, and an exponential decrease in costs (Fig. 1.1). For instance, group-III-nitride-based LEDs have been engineered to emit over the entire visible spectrum with efficiencies close to 60% at low injection currents [15, 16]. A single modern high-power diode laser (HPDL) emitting in the infrared regime can output 20 W of optical power over a tiny emission region of 200 μm × 2 μm with an electrical-to-optical conversion efficiency of ∼70% [17]. Stacks of diode laser bars coupled with state-of-the-art cooling technologies have enabled generation of output powers exceeding 20 kW in multi-mode systems [3] (Fig. 1.2). The high brightness and efficiency of HPDLs makes them a key component in solid-state and fiber laser systems as pump sources.

However, most high-power optoelectronic devices suffer from rollovers in efficiency when operating at high injection currents. [4, 18, 19, 20, 21]. Figure 1.3 depicts the external quantum efficiency (EQE) of a 450 nm light emitting diode (LED) as a function of the operating current measured for various temperatures [4]. The dramatic decrease in EQE with increasing operating currents is a trend observed consistently across III-nitride LEDs and is referred to as the 'efficiency

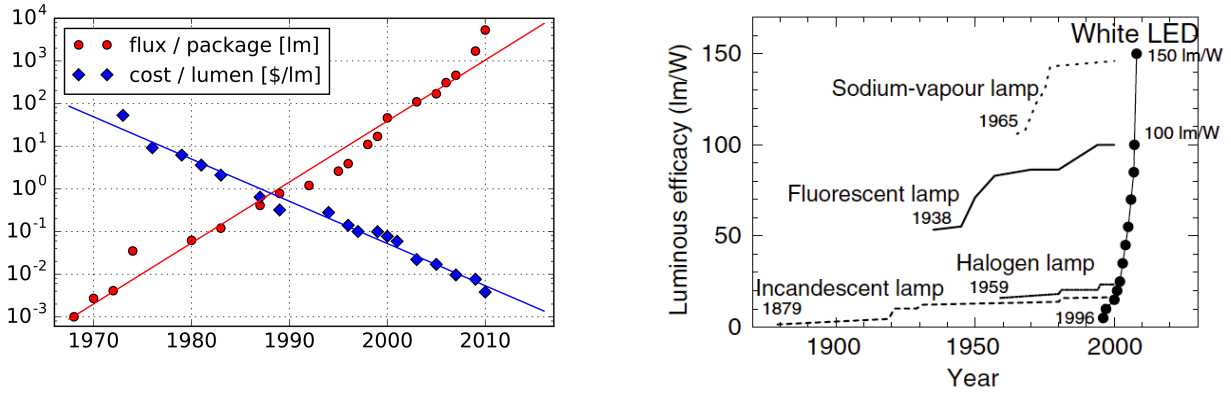

(a) (b)

Figure 1.1: (a) Illustration of Haitz's law depicting the exponential increase in optical power output per package alongside an exponential decrease in the cost per unit brightness for LEDs. Image courtesy of ref. [1] (b) Comparison of the evolution in luminous efficacy for a variety of optical sources. The increase in efficiency of white LEDs has been dramatic over the past 20 years. Image courtesy of ref. [2].

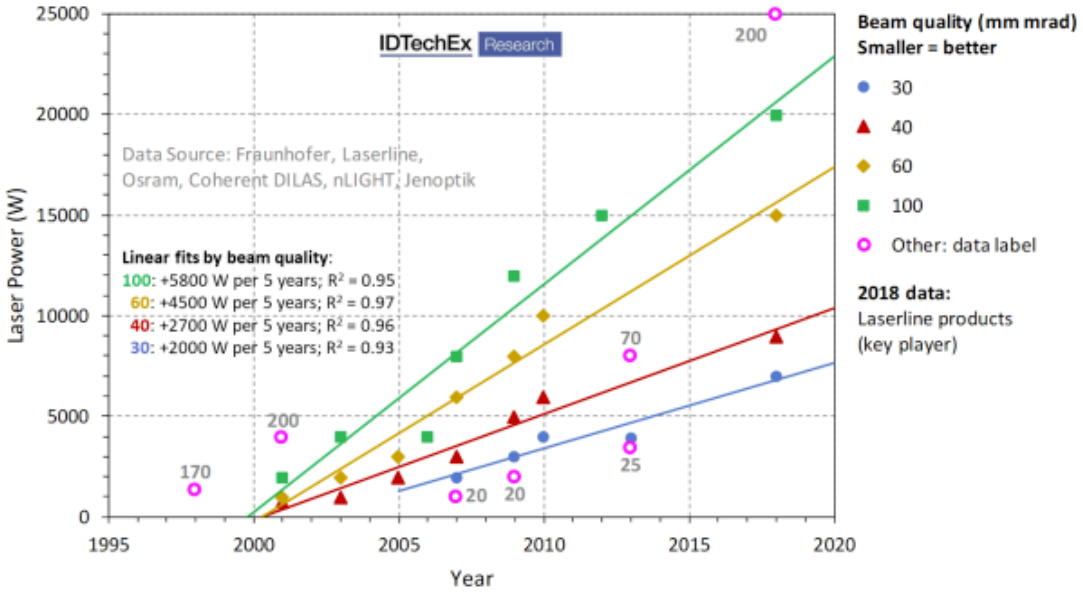

Figure 1.2: The evolution of output power and beam quality in high-power direct diode lasers (integrated systems comprised of several diode laser bars, cooling solutions and control electronics) at an emission wavelength of 1000 nm, based on data collected from several diode laser manufacturers. Image courtesy of [3]

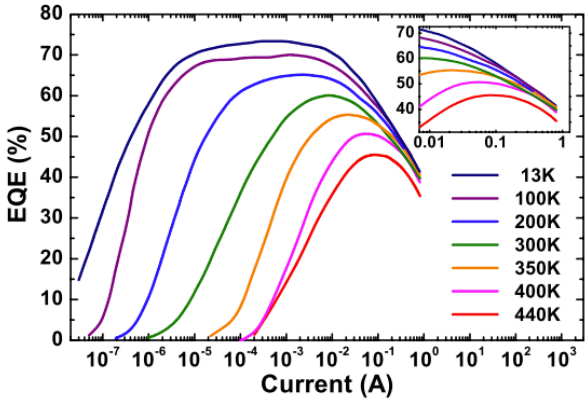

Figure 1.3: External quantum efficiency (EQE) vs operating current for a 450 nm LED for various temperatures. Inset shows the behavior at large currents in more detail. Elevated temperatures as well as large injection currents lead to significant reduction in the efficiency of LEDs. The EQE reduction at high injection currents is partly thermally induced. Image courtesy of ref. [4].

droop' [4, 18, 19, 22], a phenomenon which limits the maximum output power of high-power LEDs. Efficiency droop is caused by an increase in non-radiative carrier loss mechanisms such as Shockley-Read-Hall (SRH) recombination, Auger recombination and carrier leakage, at large injection currents [19]. Carrier leakage itself encompasses several distinct issues such as poor hole injection efficiency, ineffective electron blocking layer and incomplete carrier capture within the quantum well region. These issues are exacerbated at elevated temperatures (as evident from Fig. 1.3) due to the temperature-dependence of the recombination rates associated with the non-radiative processes. SRH recombination rate increases with an increase in temperature which leads to a lower peak efficiency as temperature increases [19]. The radiative recombination and Auger recombination constants can be expressed empirically through power laws as descending functions of temperature [23], although there is some evidence of a weak increase in Auger recombination with temperature in InGaN-based LEDs [24]. Moreover, the light extraction efficiency in LEDs has also been observed to decrease with increasing temperature due to an increased rate of photon absorption by both free and bound carriers [4].

In the case of high-power diode lasers, a saturation or rollover in the power-current characteristics is commonly observed when the laser is operated far above the threshold current of the device.

[20, 21, 25] The rollover (decrease in slope efficiency) is caused by thermally induced carrier and photon loss, and can be described in a simple manner by assigning exponential temperature dependencies to threshold current and slope efficiency with characteristic temperatures T_0 and T_1 [26]. The mechanisms which leads to this effect can be described as follows. Due to the finite thermal resistance of the package, an increment in the injection current leads to an increment in the device temperature. The elevated temperature results in an increase of the free carrier absorption cross-section for electrons and holes [20], which leads to higher optical loss and larger threshold gain, which translates into an increased carrier density at threshold. This feeds into a positive feedback loop where increased carrier density leads to larger optical loss and ultimately to a lower slope efficiency [27]. In fact, the slope efficiency is not only lowered due to an increase in optical loss, but also due to the increase in carrier density which leads to larger rates of SRH and Auger recombination, and carrier leakages. In addition, high carrier density increases the effect of longitudinal spatial hole burning [28] and reduces internal efficiency [27].

In high-power diode lasers, elevated temperatures are associated with not just efficiency drops, but also with significant physical damage to the device. The problem of degradation of diode lasers was identified soon after the achievement of continuous wave (CW) operation of heterostructure diode lasers in the 1960s. Studies on dark line defect growths in the active region [29], elongation of dislocation networks [30], photo-assisted facet oxidation [31] and effectiveness of facet coatings for suppression of facet degradation [32], have helped in rapid improvement of lifetime and reliability of high-power diode lasers over the last 50 years. However, the degradation mechanisms which currently limit the maximum brightness and lifetime of these devices are believed to be primarily thermal in nature.

Figure 1.4 (a) depicts the optical power output as a function of injection current for a 900 nm high-power diode laser rated at 3.75 A. The rollover in the slope of the curve beyond the rated current is caused by an increase in the rate of non-radiative processes and carrier leakages which are driven in part by the increase in temperature due to self-absorption of optical emission. At even higher injection currents, the diode laser fails completely, and dark regions can be observed

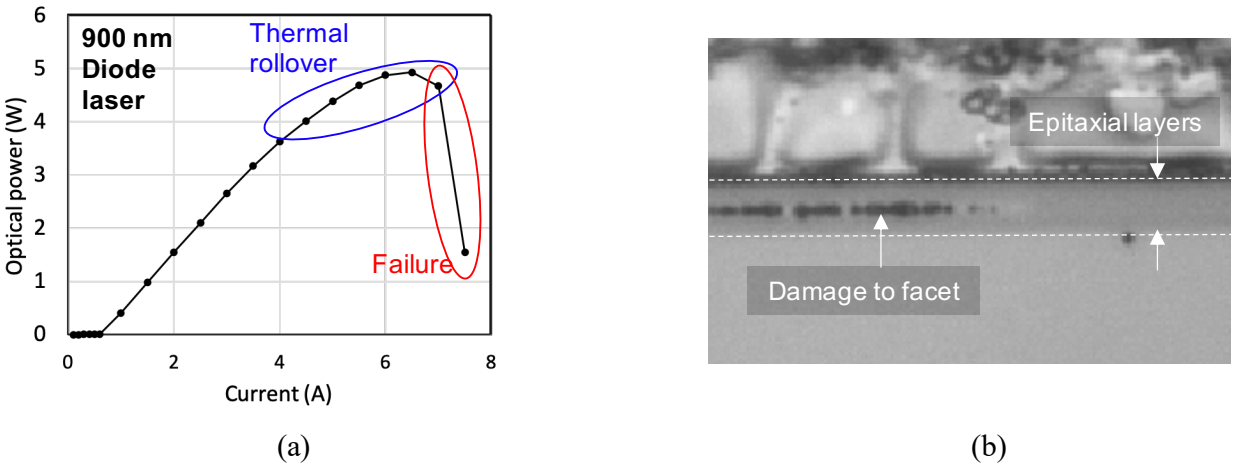

(a) (b)

Figure 1.4: (a) Optical power as a function of injection current for a 900 nm diode laser rated at 3.75 A. The decrease in slope efficiency above 4 A current is a consequence of an increase in non-radiative recombination processes induced by elevated temperatures. (b) At large injection currents, the laser can undergo severe damage seen here as dark regions within the epitaxial lasers.

within the epitaxial layers of the active region (Fig. 1.4 (b)) where significant damage occurs due to severe local heating.

Modern applications of high-power diode lasers demand reliable device operation over long lifetimes. Hence, the degradation modes of high-power diode lasers have been studied extensively in view of improving their reliability and extending the range of their applications. The degradation modes in a high-power diode laser under regular operation can be classified in terms of the time scale over which they affect the device characteristics [33, 34].

1. Rapid degradation is typically observed within the first 100 hours of device operation, and manifests as a rapid decrease in power output (or a rapid increase in threshold current). Threading dislocations can be introduced within the device heterostructure during the crystal growth process, or during the handling and/or mounting of the device. These dislocations can undergo elongation and develop into dark line defects due to interactions with injected charge carriers and those generated by re-absorption of laser emission [35, 36]. Dark line defects appear as dark oriented structures within the emission region and lead to significant reduction in device output power.

2. Gradual degradation occurs over several thousand hours of device operation and is observed as a slow decrease in output power resulting from a gradual decrease in the quantum efficiency. Such degradation is associated with an increase in non-radiative recombination caused by point defect creation and migration over long time scales [37, 38]. Essentially, non-radiative recombination at existing point defects in the device leads to formation of new point defects assisted by the process of recombination-enhanced defect reactions (REDR) [39, 40]. Over time, this feedback mechanism leads to migration and accumulation of defects which lower the quantum efficiency of the device. Typically, gradual degradation limits the lifetime of low-power diode lasers.

3. Catastrophic degradation occurs suddenly when a threshold condition is reached, and manifests as a substantial or total loss of output power, along with structural damage to the device. Generally, catastrophic degradation can occur within the device cavity or at the facets (mirrors). Catastrophic degradation that results from self-absorption of optical emission is referred to as catastrophic optical damage (COD) [41, 42] and is the most commonly observed type of catastrophic degradation. Most characteristic COD events in state-of-the-art devices occur at the outcoupling facet and are therefore called catastrophic optical mirror damage (COMD). The terms COD and COMD are often used interchangeably in the literature to refer to catastrophic degradation of mirror facets. However, COD has also been reported to occur within the inner cavity of high-power diode lasers [43], and is called bulk COD or COBD (catastrophic optical bulk damage) to distinguish it from COMD in such cases. In this work, we use the term COD to refer to the catastrophic degradation that occurs at the facet of high-power diode lasers.

Catastrophic optical damage is the result of a thermal runaway process which sets in when a critical local temperature is reached [44, 45]. This critical temperature can be achieved at the facets of high-power diode lasers through heating mechanisms such as surface recombination [46] and surface currents [47]. Facet mirrors typically exhibit larger defect concentrations compared to the bulk of the device due to the cleaving process and potential oxide growth [48, 49]. In addition,

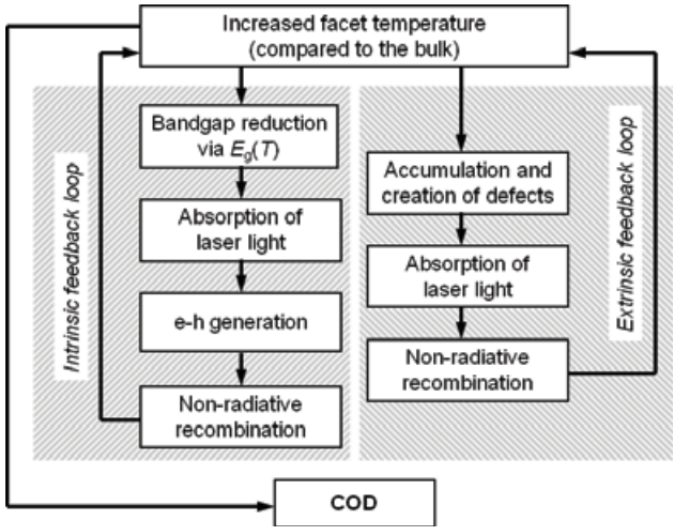

Figure 1.5: Schematic of the mechanisms leading to catastrophic optical damage in high-power diode lasers. Image courtesy of ref. [5].

diode lasers are often packaged with an overhang, where the facet is offset from the heat sink by a few microns. These factors can lead to elevated facet temperatures compared to the device bulk even at low injection currents [5]. At a high injection current above the lasing threshold, the temperatures are elevated further and may reach the critical temperature at some facet locations as a result of additional Joule heating and non-radiative recombination of charge carriers generated by absorption of laser emission at defect states.

Once the critical temperature is reached, two positive feedback loops are initiated which lead to further temperature increase. First, elevated temperatures lead to band gap shrinkage which increases the rate of optical absorption and leads to generation of more charge carriers which recombine non-radiatively and increase the temperature further [44]. Second, defect generation and accumulation, which is a thermally-activated process is enhanced and leads to even higher rates of non-radiative recombination and subsequent heating. Reports on the lowering of the threshold optical power output which can lead to COD in aged diode lasers are indicative of the existence of this feedback loop [50, 51]. These two loops occur together and can drive the temperature to the point where the device undergoes physical damage and power loss (Fig. 1.5).

It is clear that the degradation of high-power diode lasers are closely associated with the tem-

perature rise within the device cavity and at the facet. In order to study and analyze the degradation and failure modes in high-power diode lasers, it is essential to develop thermal metrologies that are capable of capturing their thermal behavior. In the next subsection, we describe the available measurement methods in detail.

1.2 Thermal Metrologies for Optoelectronic Devices

Since heating can significantly affect the performance, lifetime and reliability of optoelectronic devices, various microscale and nanoscale temperature measurement techniques have been developed. These methods can be broadly divided into two categories based on their operating mode: contact and non-contact.

1.2.1 Contact Mode-based Temperature Measurement

Contact mode-based temperature measurements are performed by placing a temperature sensor, such as a thermocouple, thermistor, resistance temperature detector (RTD) or scanning thermal microscope (SThM) [52], in contact with the measurement surface.

A thermocouple is composed of two dissimilar metal wires that are joined at one end (the tip) and connected to a voltmeter at the other end (Fig. 1.6 (a)). The voltage measured by the voltmeter is temperature-dependent, based on the thermoelectric effect, and can be calibrated to interpret and measure the temperature at the tip. Thermocouples are inexpensive, do not need costly equipment or external excitation to operate, and can measure a wide range of temperatures. Thermocouples can also operate at very high response frequencies ($>$10 MHz) and hence can be used to pick out weak thermal signals from noisy data using lock-in amplification techniques [53]. However, a few major drawbacks associated with temperature measurement using thermocouples involve low accuracy ($\sim$1 K) and poor spatial resolution. The smallest state-of-the-art thermocouple which can be constructed today has a tip size of 30 μm. Hence it cannot be used to characterize any thermal phenomena that occur at smaller length scales, which is often the case with modern optoelectronic

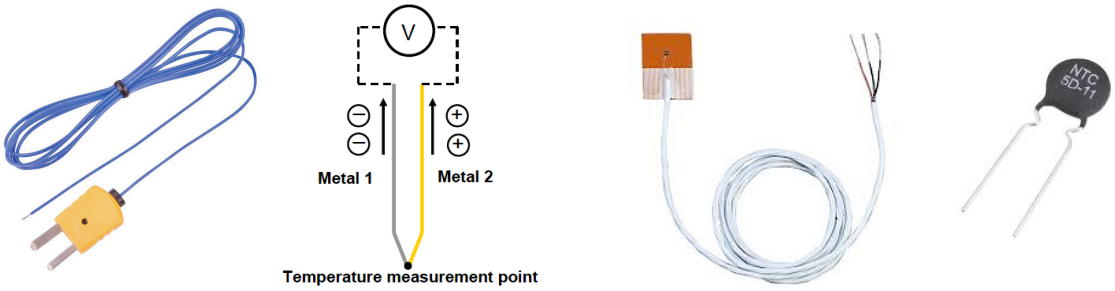

(a) (b) (c)

Figure 1.6: (a) A typical thermocouple and a schematic of the working principle. Metals 1 and 2 are n-type and p-type materials respectively. Charge carriers diffuse from the temperature measurement point to the reference point resulting in a measurable thermal voltage. A commercially available (b) resistance temperature detector and (c) thermistor, which measure temperature by sensing the thermally induced change in resistance.

devices. Moreover, placing a thermocouple in contact with the surface of an optoelectronic device can interfere with device operation. The emitted light can also be absorbed by the thermocouple which can cause it to heat up and provide inaccurate measurements.

A resistance temperature detector (Fig. 1.6 (b)) measures the change in resistance of a metal resistor induced by a change in temperature. RTDs are generally more accurate than thermocouples ($\sim$0.1 K) and also more linear in their temperature-voltage response. However, they have relatively slow response times, are costlier and require a current/voltage source for operation. Thermistors (Fig. 1.6 (c)) operate on the same basic principle as RTDs but are composed of ceramic or polymer resistors instead of metal. As such, thermistors are cheaper than RTDs but span a smaller temperature measurement range and have highly non-linear temperature-voltage response. RTDs and thermistors also suffer from the same drawback of poor spatial resolution as thermocouples. Typically, they have even larger footprints than thermocouples and cannot be used to measure thermal phenomena at finer than 1 mm resolution.

Scanning thermal microscopy (Fig. 1.7) is a scanning probe technique similar to Atomic Force Microscopy, wherein a probe, made out of thin dielectric films on a silicon substrate, is scanned over the sample. The change in the temperature of the probe (measured using an integrated ther-

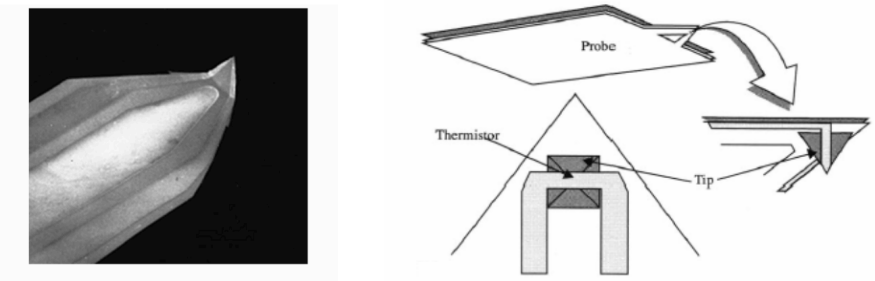

(a) (b)

Figure 1.7: (a) Au/Pd thermocouple probes for scanning thermal microscopy made by electron beam lithography and silicon micromachining. (b) Schematic of a thermistor-based scanning thermal probe. Image courtesy of ref. [6, 7]

mocouple [6]) or the thermally induced change in the resistance (measured using an integrated metal resistor [7]) is evaluated locally providing a spatial resolution of approximately 50 nm [52]. SThM has been used to study vertical cavity surface emitting lasers [54], carbon nanotube-based devices [55] and diode structures [56]. A major drawback of SThM is the absorption of optical emission, and subsequent heating, by the metal coating on the probe (used for resistance measurement) which renders the measurement inaccurate for most optoelectronic devices. In addition, SThM requires costly equipment which is difficult to operate and maintain.

In addition to the metrology-specific drawbacks detailed above, a major drawback of all contact-based methods stems from the size and thermal mass of the sensor itself. If the sensor footprint (typically $\sim$1 mm) is larger in size than the region of interest, the sensor acts as a heat sink and draws away heat from the sample leading to inaccurate measurements. Additional inaccuracies are induced in the measurement due to contact thermal resistance between the surface and the sensor resulting from imperfect contact. Contact-based methods are also unsuitable for measuring fragile surfaces/devices which can get damaged or are susceptible to modification of thermal properties upon contact. As a result, contact-based methods are largely not suitable for thermal characterization of optoelectronic devices for which the regions of interest are typically 1 - 100 μm in size and can get destroyed upon contact. A summary of the various contact mode-based temperature measurement techniques is provided in Fig. 1.8.

Metrology	Thermocouple	Thermistor	Resistance Temperature Detector	Scanning Thermal Microscopy
Operating principle	Seebeck effect	Thermally induced resistance change	Thermally induced resistance change	Nanoscale heat transfer variation
Pros	• Cost effective • Requires minimal equipment			• High spatial resolution (50 nm)
Cons	• Poor spatial resolution (30 µm) • Errors due to heat removal and thermal resistance • Non-fragile surfaces only			• Requires costly equipment • Errors due to heat removal, thermal resistance and optical absorption • Non-fragile surfaces only

Figure 1.8: A summary of the various contact mode-based temperature measurement techniques.

1.2.2 Non-contact Mode-based Temperature Measurement

Non-contact mode-based temperature sensing is usually accomplished through optical techniques such as infrared (IR) thermometry [57], Raman spectroscopy [58, 59, 60], or thermoreflectance [58, 61, 62, 63, 64, 65, 66].

1.2.2.1 Infrared Radiation Thermometry

IR thermometry estimates the temperature of a sample through measurement of its infrared radiation spectrum, given the spectral emissivity of the material is known through calibration experiments. The electromagnetic radiation intensity of a diffuse emitter ($E(\lambda, T)$), is given by the product of its spectral emissivity ($\pi(\lambda)$) and the radiation intensity of a blackbody (Planck's law):

$$E(\lambda, T) = \pi(\lambda) I(\lambda, T) = \frac{2\pi(\lambda) h c^2}{\lambda^5 (\exp \frac{hc}{\lambda k_B T} - 1)}, \tag{1.1}$$

where h is the Planck's constant, k_B is the Boltzmann constant, c is the speed of light in vacuum, λ is the electromagnetic radiation wavelength, and T is the blackbody temperature. By measuring the emissive power of an emitter at a certain wavelength and correlation with Eq. 1.1, the temperature of the body can be calculated.

Infrared thermometry provides a quick, non-contact method to create thermal maps. However,

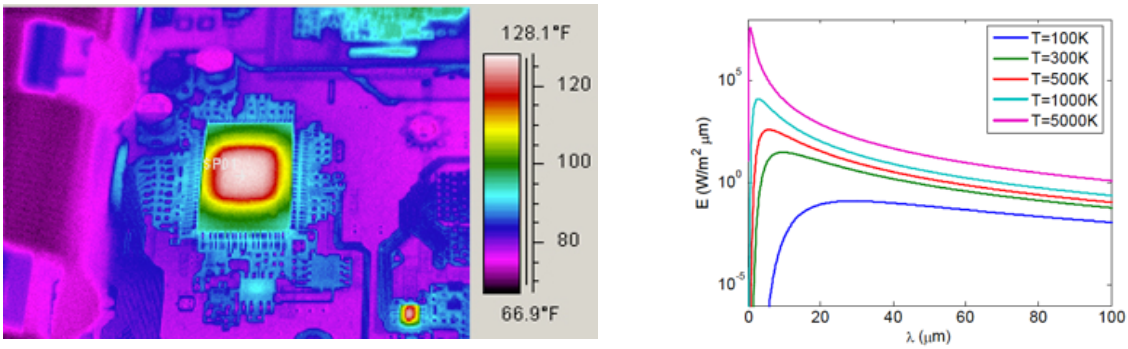

(a) (b)

Figure 1.9: (a) Infrared image of a printed circuit board (b) Spectral emissive powers of a blackbody at different temperatures. The wavelength corresponding to the peak emissive power shifts to lower wavelengths as the temperature of the blackbody increases. Image courtesy of ref. [8]

the knowledge of spectral emissivities of constituent materials of the samples is not easy to evaluate and requires separate calibration experiments.

The spectral emissive power of a blackbody at different temperatures is depicted in Fig. 1.9 (b). The wavelength at which the peak emission is achieved is a function of temperature and shifts to lower wavelengths as the body temperature increases. At room temperature, the peak emissive power of a blackbody occurs at a wavelength $\lambda \approx 10$ μm. As a result, the far field diffraction limit of $\lambda/2$ limits the spatial resolution of the IR thermometry technique to $\sim$5 μm for temperature measurements around 300 K. Since the characteristic length of typical optoelectronic devices are of the same order, IR thermometry is incapable of resolving thermal phenomena at this length scale.

1.2.2.2 Raman Spectroscopy

Raman spectroscopy is a well-known method used to determine the vibrational modes of molecules and identifying chemical components based on the detection of inelastically-scattered photons. However, Raman spectroscopy can also be used to determine the temperature of materials [58, 5]. In a typical Raman spectroscopy setup (Fig. 1.10 (a)), a laser beam is focused onto a spot on the sample and the resultant signal is passed through an optical filter to reject the purely reflected

and elastically-scattered photons before being collected by a spectrometer. The spectral peaks are plotted as a function of the Raman shift (the wavelength shift relative to the laser wavelength) as depicted in Fig. 1.10 (b) . The peaks at frequencies lower than the laser frequency correspond to the Stokes shift (phonon emission), while those at frequencies higher than the laser frequency correspond to the anti-Stokes shift (phonon absorption). The intensity of the Stokes and anti-Stokes peaks are a measure of the phonon populations at the corresponding frequencies. As such, the ratio of the Stokes and anti-Stokes peak intensity is only a function of the phonon frequency and the temperature,

$$\frac{I_{AS}}{I_S} = \left(\frac{\omega_L + \omega_V}{\omega_L - \omega_V}\right)^4 exp\left(\frac{-\hbar\omega_V}{k_B T}\right) \tag{1.2}$$

where ω_L is the excitation laser frequency, ω_V is the frequency of the phonon (vibrational mode), k_B is the Boltzmann constant and T is the temperature. Since the phonon frequencies can be determined from the Raman spectrum, the temperature can be extracted from Eq. 1.2.

An alternative method of calculation of temperature from the Raman spectrum involves tracking the shift in the peak position with sample temperature [5]. As the temperature changes, the energy of the vibrational mode will change, leading to a shift in the position of the peaks in the spectrum. The shift can be calibrated for a known temperature change and used for future temperature measurements.

The spatial resolution of Raman spectroscopy thermometry is limited by the size of the focused laser beam spot on the sample which is typically $\sim$1-2 μm [58]. However, the error in measurement is typically in the range of 5% - 15% which is relatively poor [59, 60]. In addition, the focused laser beam can heat up the sample and introduce errors in the measurement. Moreover, the method inherently lacks the ability of generating two-dimensional surface temperature maps and can only be used for point measurements.

Thermal characterization of optoelectronic devices ideally warrants a thermometry technique which is non-contact, offers diffraction-limited resolution, high accuracy and two-dimensional temperature mapping capabilities. The phenomenon of thermoreflectance, wherein a change in

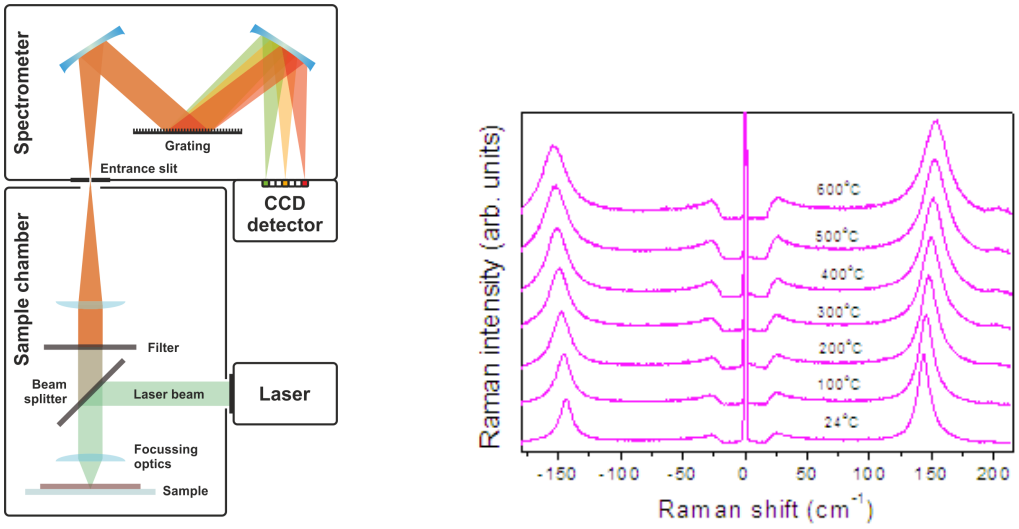

(a) (b)

Figure 1.10: (a) Schematic of a typical Raman spectroscopy measurement setup. An excitation laser beam is focused onto the sample and the spectrum of the inelastically scattered photons is recorded after interaction with the sample. (b) Raman spectra of a TiO_2 sample measured in the temperature range 24°C - 600°C. [] The peaks correspond to phonon absorption (anti-Stokes peak) and phonon emission (Stokes peak). Temperature of the sample can be ascertained from the ratio of the Stokes and anti-Stokes peak intensity and the vibrational mode frequency

Metrology	Infrared Thermometry	Raman Spectroscopy	Thermoreflectance-based Thermometry
Operating principle	Infrared radiation spectrum measurement	Inelastically-scattered photon spectrum measurement	Measurement of thermally induced change in surface reflectance

Pros	• Non-invasive
	• 0.1 K temperature resolution
		• Non-invasive
		• 1 μm spatial resolution
			• Non-invasive
			• spatial resolution
			  ○ 0.5 μm (broad area)
			  ○ 1 μm (point-based)
			• 0.1 K temperature resolution

Cons	• 5 μm spatial resolution • Emissivity calibration • IR camera	• 5 K temperature resolution • Raman setup • Parasitic probe beam heating	• Thermoreflectance coefficient calibration • Lock-in detection setup

Figure 1.11: A summary of the various contact mode-based temperature measurement techniques.

the temperature of a material induces a change in its reflectance, offers the possibility of such a measurement system. It is the primary temperature measurement approach applied in this work and is described in detail in the following section. A summary of the various non-contact mode-based temperature measurement methods is provided in Fig. 1.11.

CHAPTER 2

Thermoreflectance-based Thermometry

2.1 Physics of Thermoreflectance

Thermoreflectance is a non-contact, optical measurement technique that quantifies the temperature change of a material or device by correlating it with temperature-induced optical reflectivity variation. In semiconductors, this variation in reflectivity is primarily due to the shrinkage of the band gap E_g with increasing temperature T. The band gap shrinkage is caused by shifts in the conduction and valence band edges due to changes induced in the lattice constant and electron-lattice interactions with temperature. Dependence of E_g on temperature can be empirically modelled as,

$$E_g = E_0 - \frac{\alpha T^2}{T + \beta}, \tag{2.1}$$

where E_0 is the bandgap at 0 K, and α and β are constants [67]. The values of α and β for GaAs, a common semiconductor used in optoelectronic devices, are 5.58×10^{-4} eV/K and 220 K respectively. The small change in band gap caused by temperature changes, induces a change in the refractive index n of the material. The relationship between E_g and n can be semi-empirically expressed using the Moss relationship [68],

$$n^4 E_g = constant. \tag{2.2}$$

For light incident normally on the material from air, assuming no absorption, the reflectance (fraction of the incident light which gets reflected) of the material can be expressed as,

$$R = \left| \frac{n-1}{n+1} \right|^2 \tag{2.3}$$

Clearly, a change in the temperature ΔT of the material will lead to a change in its reflectance ΔR (equations 2.1, 2.2 and 2.3). A detailed analysis of the phenomenological basis of thermoreflectance involves studying the change in the complex dielectric function $\hat{\epsilon}(E) = \epsilon_1(E) + i\epsilon_2(E)$, where ϵ_1 and ϵ_2 are the real and imaginary parts of the dielectric function and E is energy [69, 70]. The normalized change in reflectance can be expressed as,

$$\frac{\Delta R}{R} = \alpha(\epsilon_1, \epsilon_2)\Delta\epsilon_1 + \beta(\epsilon_1, \epsilon_2)\Delta\epsilon_2 \tag{2.4}$$

The coefficients α and β are functions of the complex refractive index of the material, and thus the photon energy. The contributions $\Delta\epsilon_1$ and $\Delta\epsilon_2$ are the changes in the complex dielectric function induced due to temperature change ΔT, and can be expressed in terms of the band gap shift and broadening [71].

While such analysis of thermoreflectance is useful for studying the band structure and dielectric response function of semiconductors, in this work we focus on thermoreflectance-based thermal measurements, for which the effects of temperature on material's reflectance modulation can be simplified using a calibration coefficient. Hence, the relationship between ΔT and ΔR is usually approximated to be linear for small values of ΔT and expressed by the equation,

$$\Delta T = \kappa^{-1} \frac{\Delta R}{R}, \tag{2.5}$$

where $\frac{\Delta R}{R}$ is the normalized change in reflectance (thermoreflectance signal) caused by a temperature change ΔT and κ is a proportionality constant known as the thermoreflectance coefficient. The value of κ is dependent on the material properties, illumination wavelength and optical properties of the experimental setup. It effectively accounts for the complexities of the material band structure and the optical properties of the material and other optical components in the experimental setup with typical values ranging between 10^{-6} to 10^{-3} [61, 72]. Since κ is dependent on

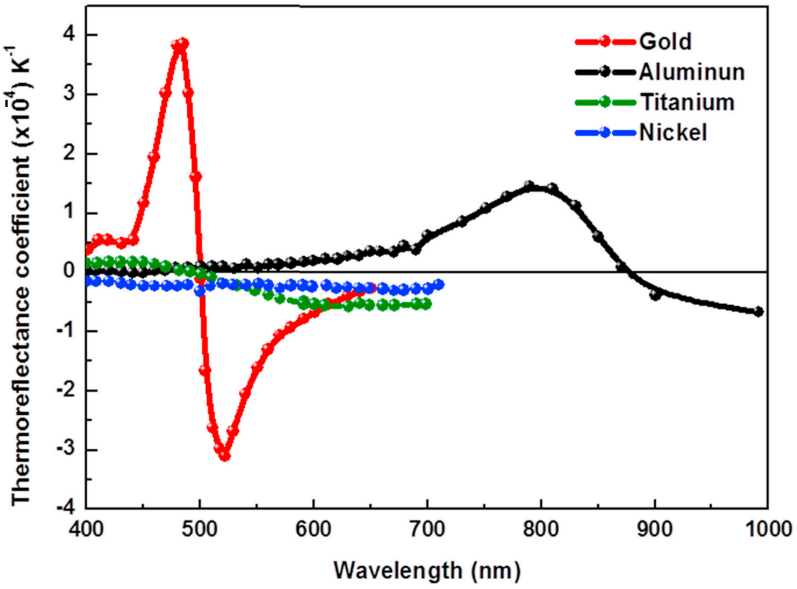

Figure 2.1: Thermoreflectance coefficient values of some metals for illumination wavelength range of 400 - 1000 nm. Most materials exhibit strong thermoreflectance response at certain wavelenghts. The thermoreflectance coefficient value of gold switches sign around 500 nm which is indicative of the complex interplay of temperature with the band structure and optical absorption properties of materials.

material properties as well as properties of the measurement setup, its value needs to be calculated separately for a particular set of experimental conditions and sample material. The choice of illumination wavelength is key to thermoreflectance measurements, since most materials exhibit a strong thermoreflectance response (large value of κ) at certain illumination wavelengths. A large value of κ translates into a stronger thermoreflectance signal which improves the signal-to-noise ratio of the measurements. Figure 2.1 depicts the spectrum of κ for a few metals.

2.2 Types and Application of Thermoreflectance-based Thermometry

Thermoreflectance has been successfully applied to study a variety of thermal phenomena in electronic devices and semiconductor materials [58, 61, 62, 63, 64, 65, 66]. Thermoreflectance techniques can be classified based on the mode of measurement: point-based or broad area imaging.

They can also be classified based on the nature of thermal process being analyzed: steady/quasi-steady or transient.

In point-based thermoreflectance, a low power laser beam is focused onto a spot on the material (typically 1-2 μm in size) using an objective lens, and the reflected light is captured by a photodiode which measures $\frac{\Delta R}{R}$. Since a photodiode is a low noise detector, it provides good signal-to-noise ratio (SNR). In addition, a photodiode offers very quick response times and can detect rapid changes in temperature. As such, it is suitable for characterizing both steady-state and transient thermal processes. However, it can only provide measurements for a single-point on the device at a time. Moreover, focusing a laser beam onto a point on the material can cause parasitic heating and limit the spatial resolution of the measurement to the size of the spot.

Using a Charge-coupled device (CCD) camera as the detector and an LED as the source for broad area illumination allows generation of two-dimensional temperature profiles of the region of interest since the CCD pixel array can image signals in parallel from a large field of view. Essentially, each pixel on the CCD sensor can measure $\frac{\Delta R}{R}$ for a unique point on the sample and thus generate a thermal image. The size of the field of view afforded by the CCD camera is dictated by the magnification of the objective lens. Additionally, it is possible to achieve diffraction limited spatial resolution of $\sim$0.5 μm (when using blue light illumination). However, there are few caveats associated with CCD-based measurements. CCDs are susceptible to readout and shot noise and the magnitude of this noise is typically $\sim$100 times higher than the thermoreflectance signal strength [73]. This shortcoming can be overcome by averaging signals over several measurements. However, the frame rate of CCD cameras is typically less than 100 frames per second (fps), which makes CCD-based measurements inherently much slower than photodiode-based methods. The extensive averaging needed for accurate measurements combined with the relatively low response time/frame rate of CCD cameras ($\leq$ 100 Hz) implies that using CCD cameras for thermal imaging of transient phenomena is not straightforward. However, such measurements have been performed with a CCD camera using a high frequency-modulated LED for illumination [74].

Transient thermoreflectance is often performed as a pump-probe technique with a femtosecond

pulsed source and a fast detector and is typically a single-point measurement. Transient thermoreflectance measurements are commonly used to characterize material thermophysical properties such as thermal conductivity [63], thermal diffusivity [64], electron-phonon coupling [65] and thermal boundary resistance [66]. In the pump-probe technique called time-domain thermoreflectance (TDTR) [75], a laser beam is divided into two beams - the pump and the probe. The pump beam is modulated at a high frequency (1-10 MHz) using an electro-optic modulator, and focused onto the sample where it induces a local temperature change on the sample at the point of incidence. The probe beam is low-intensity and is incident on the same spot on the sample but arrives after a controllable time delay, typically achieved by moving a mirror mounted on a linear motorized stage. The reflected probe beam intensity can be recorded and extracted by a photodiode combined with a lock-in amplifier. By analyzing the change in reflected probe beam intensity (representative of the sample local temperature) as a function of the time delay, it is possible to probe thermal phenomena at nanosecond resolution. TDTR, and its variation - frquency-domain thermoreflectance (FDTR) are powerful techniques that have been used extensively to study thermal properties of materials [75, 76, 77], but is limited to point-based measurements since it requires coherent illumination and a sensor with very fast response time.

The choice of the mode of measurement (point-based or broad area), type of detector (CCD camera or photodiode), the magnification of the objective lens and the wavelength of illumination are dictated by the characteristic length scale of device under test, the time scale of thermal phenomena being analyzed and the composition of the device. In this work, we have focused on generating two-dimensional maps of temperature rise near the active region of high-power diode lasers under steady-state operation. Hence, we have developed a microscope setup equipped with high magnification objectives lenses with a CCD camera as the detector.

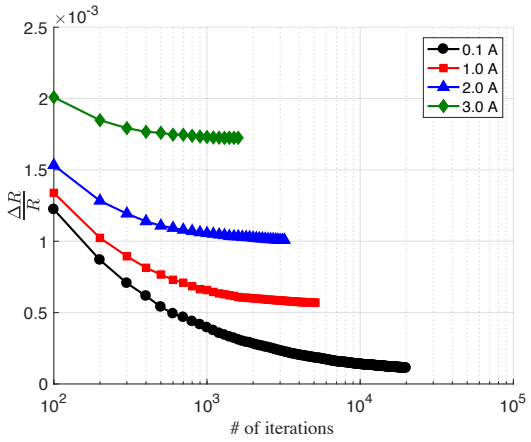

Figure 2.2: Convergence of thermoreflectance signals from the GaAs substrate material of a diode laser operating over a range of currents. The number of iterations (averaging) required for convergence is a function of the signal strength. As the signal becomes weaker (0.1 A), the number of iterations required to achieve convergence increases exponentially.

2.3 CCD Camera-based Thermoreflectance (CCD-TR)

The ability of a CCD camera to measure small changes in brightness is dependent on its bit depth. For example, a 12-bit camera can only detect $\frac{\Delta R}{R} \geq 2^{-12}$ in magnitude between two images (quantization limit). This value is relatively large compared to typical thermoreflectance signal strength and technically implies that a CCD camera is expected to be insensitive to small temperature changes. However, a phenomenon called stochastic resonance [19], caused by the inherent CCD readout noise, allows measurement of thermoreflectance signals well below the camera quantization limit by simply averaging over several measurements. The number of measurements needed for achieving a converged $\frac{\Delta R}{R}$ signal is a function of the camera bit depth and signal strength but is typically in the range of $10^3 - 10^5$ [73]. Figure 2.2 depicts the convergence of $\frac{\Delta R}{R}$ signal from the GaAs substrate material of a diode laser operating over a range of currents. As the injection current increases, the temperature signal grows stronger and the number of iterations needed for convergence reduces by an order of magnitude.

The CCD-TR setup can be used to determine the temperature rise of a device under steady-state operation as follows. First, the device is turned on at the given bias and an image I_1 of the device

is taken. Then, the device is turned off and a second image I_2 is captured. In this case, the change in reflectance ΔR induced by the temperature rise caused by operation of the device is given by $I_1 - I_2$. Hence the map of temperature rise is an image which can be calculated as,

$$\Delta T = \kappa^{-1} \frac{\Delta R}{R} = \kappa^{-1} \frac{I_1 - I_2}{\frac{I_1 + I_2}{2}}. \tag{2.6}$$

However, as described before, the image is noisy and needs to be averaged over several measurements in order to improve the signal-to-noise ratio (SNR). This can be done by taking several images when the device is ON and averaging them to calculate I_1 and repeating this after turning the device off to calculate I_2. Typically, the number of images required to improve the SNR by this method is very large and the convergence of the signal is extremely slow due to the large noise, spread over a wide frequency band, inherent in CCDs. However, the SNR can be quickly and greatly improved by turning the device ON and OFF cyclically at a frequency f and triggering the camera to capture images at a frequency $2f$ such that it is phase-locked with the device bias signal (Fig. 2.3). Hence, two images are acquired for every ON/OFF cycle of the device, one during the ON period and another during the OFF period. These two images are averaged over a large number of iterations to provide a converged thermal image. In this way, any fluctuations in pixel intensity of images which are oscillating away from the frequency of interest f are quickly averaged out, greatly improving the signal to noise ratio. This technique is akin to a software-analogue of hardware lock-in based signal acquisition techniques.

It is important to remember that the device will require some time to reach steady state, hence the temperature waveform of the device will lag behind the bias signal with a phase difference ϕ. In order for Eq. 5 to be valid, the camera should start integrating the images only after steady state has been achieved. This is typically not an issue if the device bias frequency is low and thermal time constant of the package is small which is the case with diode lasers. For diode lasers, the thermal time constant of the device is $\sim$100 μs and the device ON/OFF time can be set to $\sim$ 250 ms (f = 4 Hz) such that $\phi \approx 0$ and the temperature waveform can be approximated as a square wave. However, in case the phase difference ϕ between the bias signal and thermal waveform is

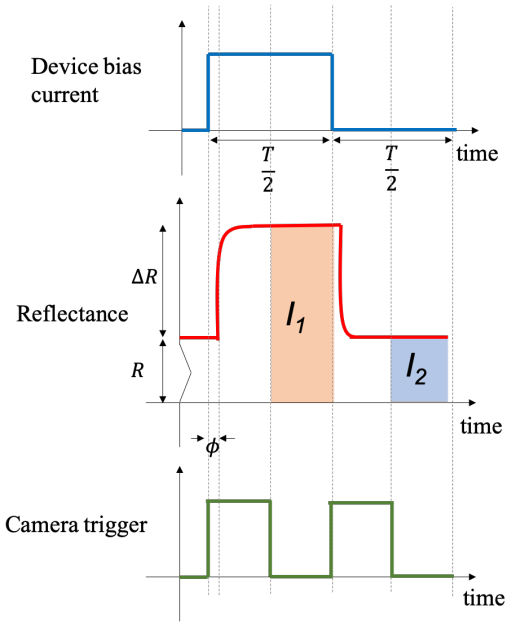

Figure 2.3: A schematic of the 2-bucket thermoreflectance imaging technique. The device is operated at a frequency f while the camera is triggered by a square waveform of frequency $2f$ such that two images (I_1 (I_2) for ON (OFF)) are captured per device cycle. The map of device temperature rise can be obtained from these images.

expected to be large, it is useful to implement a 4-bucket lock-in scheme instead of the 2-bucket scheme described above. In the 4-bucket scheme, four images are acquired for every ON/OFF cycle of the device, two during the ON period (I_1 and I_2) and two during the OFF period (I_3 and I_4). In this case, the temperature rise map and the phase difference ϕ map is given by,

$$\Delta T = \kappa^{-1}\frac{\Delta R}{R} = \kappa^{-1}\frac{1}{\sqrt{2}}\frac{\sqrt{(I_1 - I_3)^2 + (I_2 - I_4)^2}}{\frac{(I_1+I_2+I_3+I_4)}{4}}. \tag{2.7}$$

$$\tan\phi = \frac{I_1 - I_2 - I_3 + I_4}{I_1 + I_2 - I_3 - I_4} \tag{2.8}$$

In this work, we have used the 4-bucket scheme to generate thermal images of diode lasers. Figure 2.4 illustrates the waveforms involved in the 4-bucket scheme of thermoreflectance imaging.

Several groups have used the phase-locked version of CCD-TR to measure thermal response of electronic and optoelectronic devices under operation including organic LEDs [9], quantum

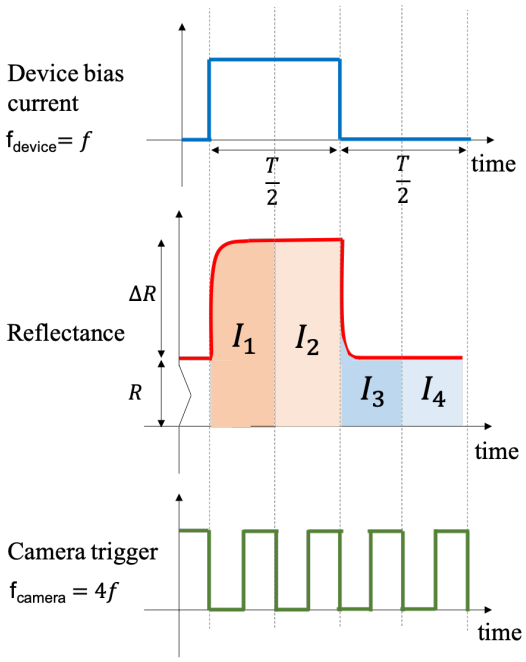

Figure 2.4: A schematic of the 4-bucket thermoreflectance imaging technique. The device is operated at a frequency f while the camera is triggered by a square waveform of frequency $4f$ such that four images (I_1 and I_2 (I_3 and I_4) for ON (OFF)) are captured per device cycle. The map of device temperature rise and the phase lag (between the bias signal and thermal signal) can be obtained from these images.

cascade lasers [10], and high electron mobility transistors [11] (Fig. 2.5).

Figure 2.6 depicts the CCD-TR system used in this work. The custom microscope system includes a 100X or 50X objective (Mitutoyo Plan Apo NIR HR infinity corrected) and a 14-bit CCD camera (Allied Vision Prosilica GT 1920) which provide a 91.1 μm × 67.7 μm field of view (at 100X magnification). The laser facet is illuminated by a blue LED (Luxeon StarLEDs) with λ = 470 nm and $\Delta\lambda$ = 20 nm full width at half maximum (FWHM). The reasoning behind this choice of illumination wavelength is two-fold. Firstly, the constituent materials of HPDLs are GaAs-based which have a strong thermoreflectance response at 470 nm. Secondly, using the shortest possible wavelength allows for the best resolution since the resolving power of a microscope system is inversely proportional to the illumination wavelength. Koehler illumination [78] is implemented to achieve uniform illumination over the entire facet using a set of two f = 20.1 mm condenser lenses with a diffuser (Thorlabs). The LED light reflected by the facet is focused onto the CCD camera by an f = 200 mm tube lens. A dichroic mirror (Semrock edge-pass λ = 680 nm) and an OD 6 band-pass filter centered around the LED wavelength are used to prevent laser emission from reaching the sensor since even a small leakage of laser emission onto the CCD sensor can saturate the pixels and mask the thermal signal. Using this system, we have been able to achieve a spatial resolution of $\sim$0.5 μm and temperature resolution of $\sim$0.2 K. Figure 2.7 depicts a photograph of the experimental setup. It is worth noting that the spatial resolution of $\sim$0.5 μm corresponds to resolution of the microscope imaging system. The spatial resolution afforded in the thermal images generated using this method is expected to be the same ($\sim$0.5 μm) if the temperature rise of the device is small. For large temperature changes, the motion induced due to cyclical thermal expansion and contraction of the device degrades the resolution by the same magnitude as the range of motion.

During a typical thermoreflectance experiment, the diode laser is mounted on a temperature and position-controlled stage. It is driven by a square wave current with 50% duty cycle at a frequency of 4 Hz. The camera is triggered to acquire four images for every ON/OFF cycle with an integration time of 62 ms per image. The $\frac{\Delta R}{R}$ signal at every pixel is calculated from these four images, as they

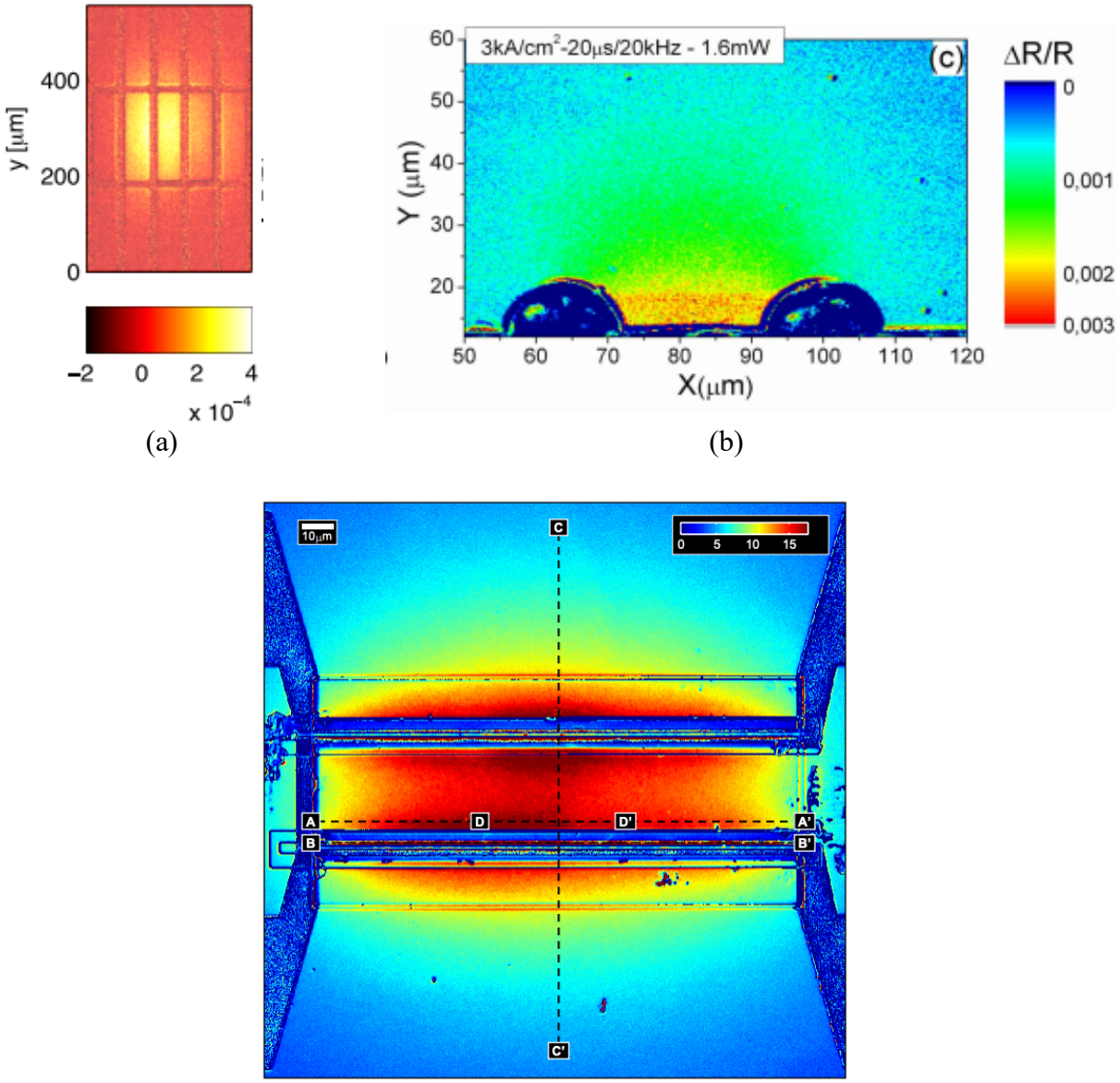

Figure 2.5: CCD-based thermoreflectance imaging has been used to study thermal response of electronic and optoelectronic devices at micron scales including (a) organic light emitting diode pixels [9] (b) quantum cascade lasers [10] and (c) high-electron mobility transistors [11]. The resolution and field-of-view size of the imaging system depends on the magnification of the microscope and the choice of illumination wavelength.

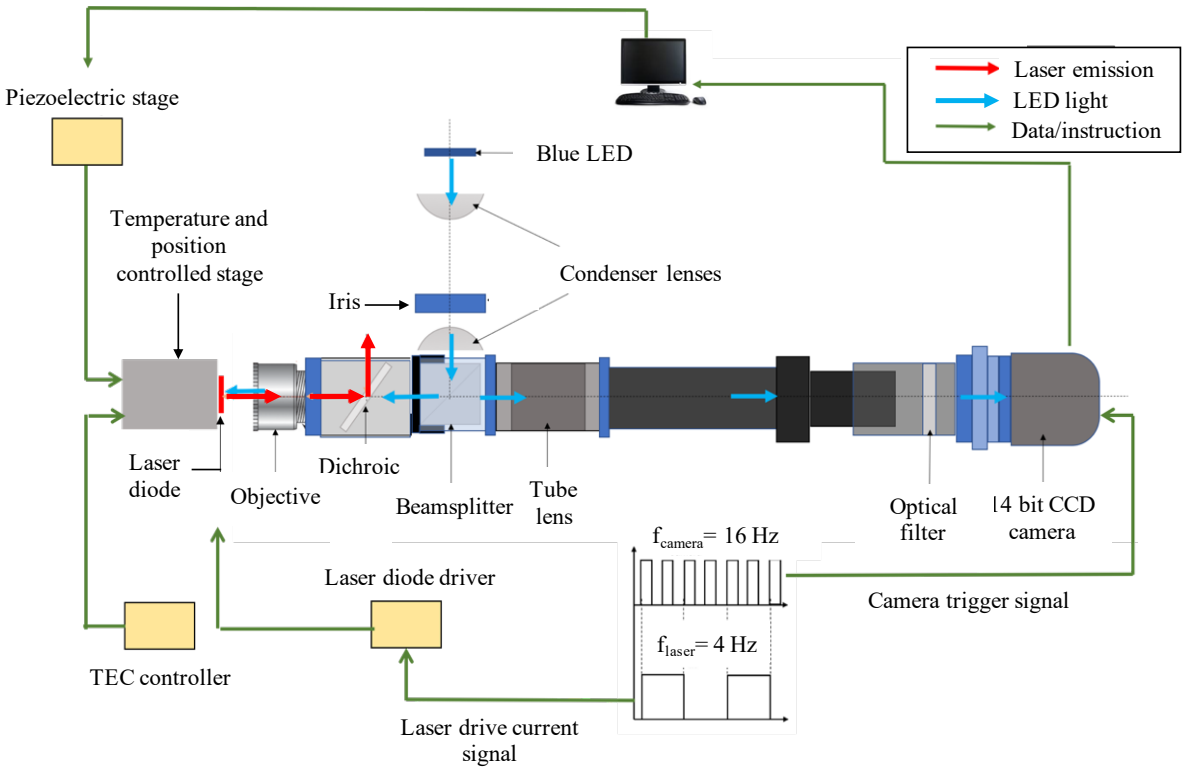

Figure 2.6: A schematic of the experimental setup used for CCD-based thermoreflectance imaging.

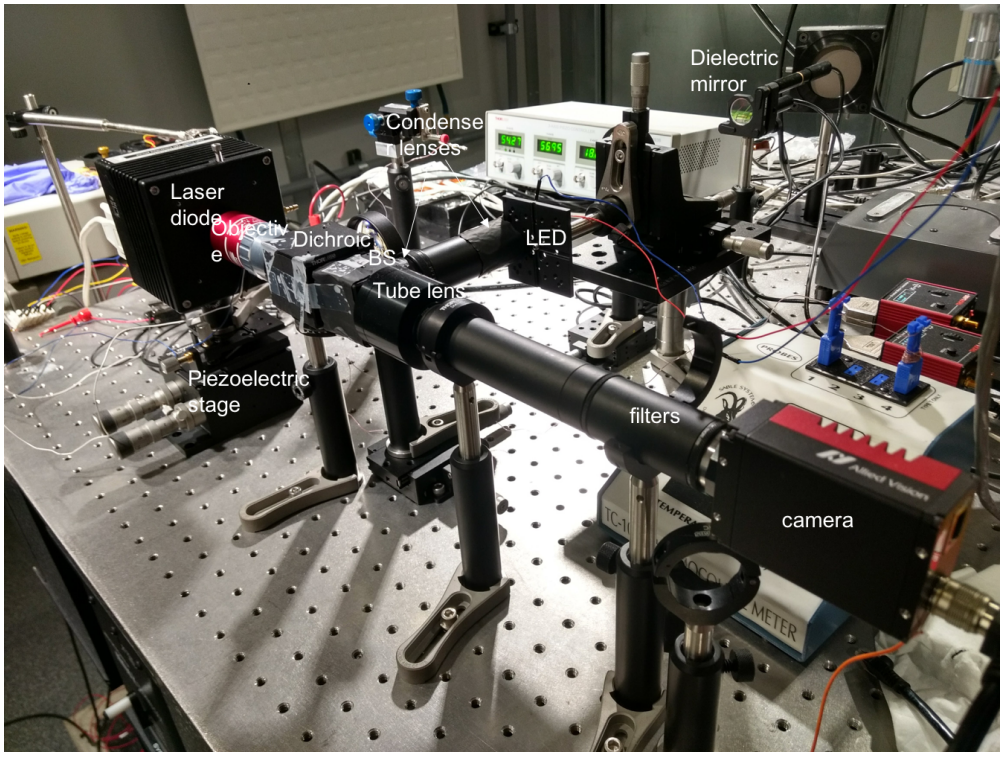

Figure 2.7: An image of the experimental setup.

provide a measure of reflectivity variation between the ON and OFF states of the diode laser. The four images are denoised by averaging over a large number of iterations to arrive at a converged $\frac{\Delta R}{R}$ image. A temperature map is then obtained from the $\frac{\Delta R}{R}$ image using Eq. 2.5. However, we need to know the values of the thermoreflectance coefficient κ for all constituent materials of the diode laser before Eq. 2.5 can be used. Since κ is not merely a material property but also depends on the optical properties of the microscope system, it has to be calculated separately through calibration experiments. These experiments are detailed in the next section.

2.4 Thermoreflectance Coefficient Calibration

In a typical thermoreflectance calibration experiment, a known temperature change is induced in a material and the thermoreflectance signal is measured. Equation 2.5 then allows the calculation of κ. The high-power diode lasers used in this work emit near 800 nm, 900 nm and 1000 nm

wavelengths and are composed of three main constituents (detailed in Section 3.3): GaAs substrate (upon which the epitaxial layers are grown), the waveguide and the cladding. The waveguide and cladding make up the active region of the diode laser. In order to calculate κ for each of these materials, witness samples of the substrate, waveguide and cladding were mounted on a thermoelectric cooler (TEC) (Fig. 2.8). The TEC was driven by a square wave of current and the sample temperature was measured using a microthermocouple. By modulating the mean and amplitude of the current signal, a range of operating temperatures were achieved (20 °C - 65 °C). For a known ΔT ($\sim$5 K), the $\frac{\Delta R}{R}$ image of the sample was recorded and κ was calculated using Eq. 2.5.

The results of calibration experiments with diode laser witness samples is plotted in Fig. 2.9. The mean values of κ for substrate, cladding and waveguide of the $\sim$800 nm diode laser at room temperature (with $\pm\sigma$ uncertainty) were measured to be $2.19 \times 10^{-4} \pm 5.5\%$, $1.28 \times 10^{-4} \pm 7.2\%$ and $1.16 \times 10^{-4} \pm 3.2\%$ respectively. We also noticed that there was no significant change in the thermoreflectance coefficient value for any material as the mean sample temperature varies. This trend is not expected for all materials since the thermoreflectance coefficient is expected to be constant only for a small temperature change. In fact, this constant value can be different for different values of T, and needs to be accounted for if the sample temperature rise is too large.

Material witness samples for the cladding and waveguide materials were unavailable for the $\sim$900 nm and $\sim$1000 nm diode lasers. As a result, a separate approach was employed to determine κ for these materials. First the average junction temperature rise was measured for the devices operating at all three wavelengths by directly measuring the red shift in emission spectrum with increasing drive current. Because the diodes are identical in geometry and package type, the offset between the average junction temperature rise and that observed at the facet are similar at sub-threshold currents where optical absorption at the facet is effectively zero. This fact was verified by simulating heat transport across the device using a two-dimensional finite element model which showed the average junction temperature rise and facet temperature at the position of the quantum well differ by less than 5% for sub-threshold currents. The $\frac{\Delta R}{R}$ images were obtained as usual for

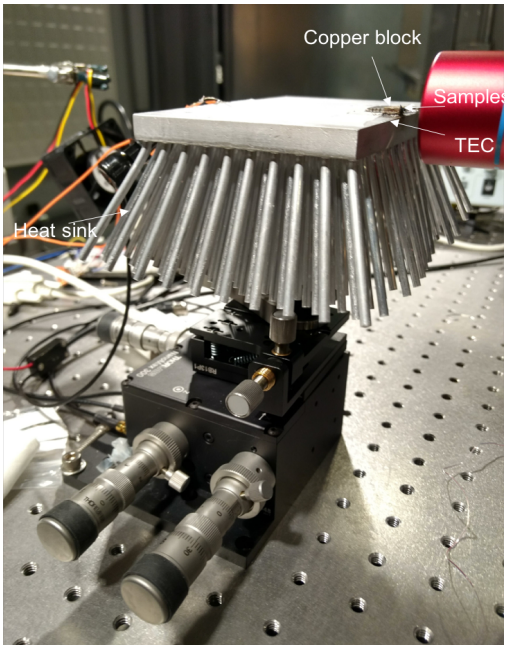

Figure 2.8: An image of the experimental setup for thermoreflectance coefficient calibration. Witness samples of laser constituent materials were mounted onto a copper block which was in turn mounted on a heat-sinked thermoelectric cooler. Thermoreflectance signal was measured for a known temperature rise over mean temperatures in the range of 20 °C - 65 °C

the ∼900 nm and ∼1000 nm devices. The appropriate values of κ were then obtained within the epitaxial layers by calibrating the sub-threshold experimental $\frac{\Delta R}{R}$ images with the previously measured active region facet temperatures. This approach, taken over multiple sub-threshold current setpoints, yielded an average κ value within the epitaxial layers of $(1.8 \pm 0.07) \times 10^{-4} K^{-1}$ (∼900 nm device) and $(9.9 \pm 0.5) \times 10^{-5} K^{-1}$ (∼ 1000 nm device).

In this section, the CCD-based thermoreflectance microscopy technique was described in detail. In the following sections, the structure of the devices under test will be described, followed by the experimental results for thermal characterization of these devices.

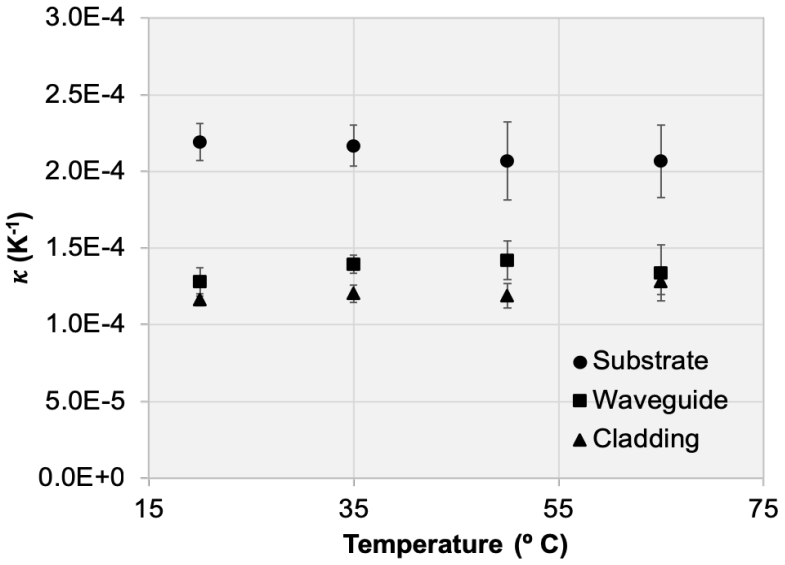

Figure 2.9: Values of κ for witness samples of $\sim$800 nm laser diode plotted as a function of temperature exhibiting a nearly constant trend. The room temperature values agree well with literature values.

CHAPTER 3

Thermal Characterization of High-Power Diode Lasers under Back-irradiance

3.1 Back-irradiance Induced Degradation of High-Power Diode Lasers

As mentioned in Chapter 1, degradation and damage in diode lasers has been a topic of active research and study over the last few decades. However, most of these studies are performed through isolated testing of diode lasers under controlled conditions. High power semiconductor lasers deployed in real laser systems are subject to different conditions than those present during isolated testing [79]. One such difference is the presence of back-irradiance (BI) of optical emission. There are numerous sources of back-irradiance in diode pumped laser systems [80], including: 1) back-scatter and reflection from micro-optics, 2) residual specular reflection from antireflection-coated optical flats, 3) amplified spontaneous emission from the laser gain medium, 4) imperfect optical isolation leading to pulsed or continuous wave laser emission leak-through, and 5) unabsorbed pump light in double-pass and double side- or end-pumped laser systems. Back-irradiance is known to alter diode behavior in several ways including a broadening of the spectral linewidth, greater fluctuations in the outcoupled optical power, a reduction in the threshold current, and a shift in the emission wavelength [80, 81, 82, 83].

An important consequence of optical feedback is accelerated device degradation leading to premature failure of high-power diode lasers [83, 12, 84, 85]. In a study conducted by DILAS

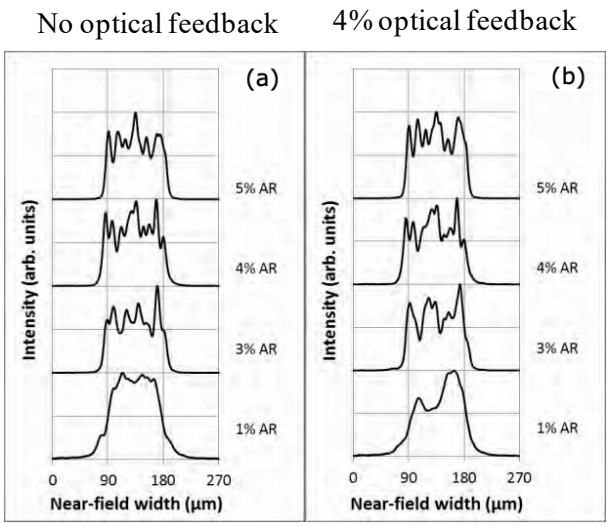

Figure 3.1: For a ∼1000 nm diode laser, 4% optical feedback leads to local intensity spikes in the near field profile. The location of the spike is found to correlate with the location of the eventual damage on the diode laser facet, at high injection currents. Image courtesy of ref. [12].

[12], it was found that feeding only 4% of the optical power back into a ∼900 nm diode laser leads to local intensity spikes in the near field profile (Fig. 3.1). Moreover, the location of the spike correlates well with the location at which eventual laser damage occurs at high injection currents. Figure 3.2 illustrates this effect, where 10 out of 24 emitters in a diode laser array failed when 24% of the outgoing laser emission was reflected back onto the facets and swept along the fast axis. This reliability hazard is of great concern in the design of virtually all diode-pumped laser systems. In this section, we use the thermoreflectance imaging system described in Section 2.3 and add the capability of generating nearly diffraction-limited back-irradiance intensity distributions. This setup is used to examine the dependence of temperature rise in the active region of diode lasers on the position of the back-irradiance, for lasers emitting at wavelengths near 800 nm, 900 nm, and 1000 nm. Through this analysis, we are able to develop an understanding of the effects of back-irradiance position, power, wavelength and polarization on its thermal contributions to diode laser failure.

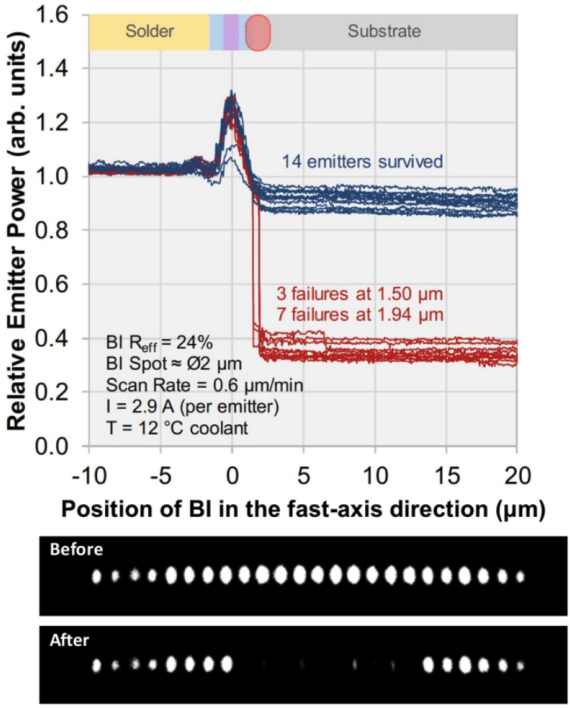

Figure 3.2: Results for destructive testing of a high-power diode laser array containing 24 emitters. 24% of the laser optical power was reflected back onto the facet and positioned at a range of locations. 10 out of 24 emitters fail when the back-irradiance is positioned close to the active region. The bottom panel shows the before and after near field intensity photographs of the 24 emitter array. Image courtesy of ref. [13].

3.2 Back-irradiance Spot Generation and Characterization

In order to generate a sharp, uniform back-irradiance spot with controllable power and position, the following modifications were made to the thermoreflectance setup described in section 2.3 (Fig. 3.3). The dichroic mirror present before the beam-splitter cube reflects $>$ 99% of the laser emission along a pathway that is perpendicular to the microscope optical axis. The laser light reflected by the dichroic passes through a 2.67X magnification 4F relay (f = 75 mm and f = 200 mm plano-convex lenses) and is incident upon a dielectric mirror of chosen reflectivity which controls the amount of optical feedback. The reflected laser emission is focused back onto the facet by the objective, forming a sharp BI spot. The position of the BI spot on the facet is controlled by a motorized kinematic mount for the mirror which offers a positional resolution of $>$ 0.1 μm on the facet.

Figure 3.4 (a) shows the size of the BI spot compared to the field-of-view (after background

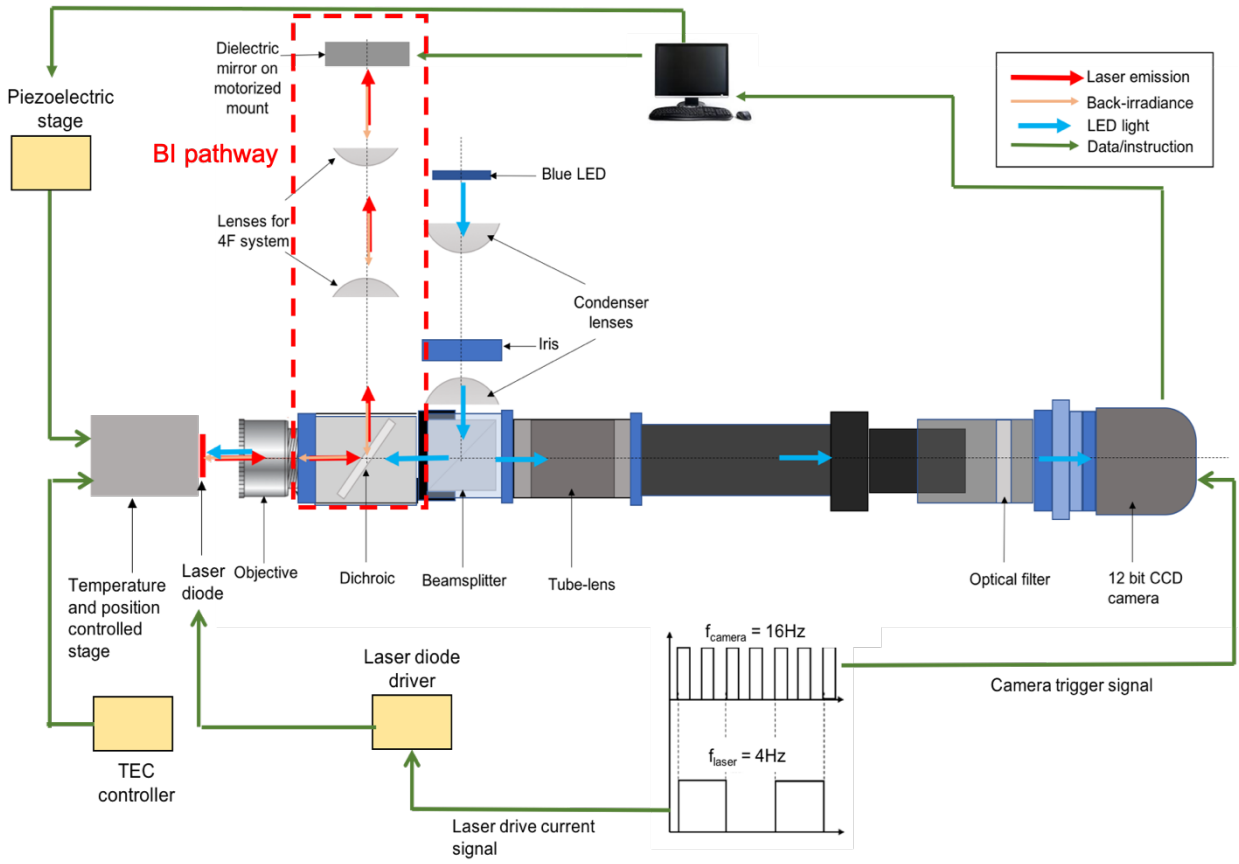

Figure 3.3: A schematic of the CCD-based thermoreflectance imaging system with added components to create a controllabel back-irradiance spot on the device. The laser emission is reflected along the back-irradiance pathway by an edgepass dichroic mirror. The emission passes through a 4F relay system, is reflected by a dielectric mirror of controllable reflectance and position and is focused onto the diode laser facet by the objective.

subtraction to remove laser emission and noise). A consistent irradiance distribution is retained as the BI is scanned along the diode facet in the fast axis direction. Figure 3.4 (b) depicts the measured beam width of the BI distribution as a function of the location of the BI spot along the fast axis of the device. The width of the BI distribution is $1.29 \pm 0.1\ \mu m$. Figure 3.4 (c) depicts the irradiance distribution of the BI spot along the fast axis direction (integrated along the slow axis direction of the diode); the peak irradiance remains nearly constant with position due to low vignetting afforded by the 4F imaging system along the feedback path of the microscope. The 2.67X magnification of the 4F relay along the feedback path allows very fine and repeatable positioning of the BI spot center.

A set of five dielectric mirrors having nominal reflectance values of 10%, 30%, 50%, 70%, and 90% were used to vary the feedback level to the diode facet. However, the wavelength-dependent reflection/transmission coefficients of the chosen feedback mirror and other optics along the feedback branch (and in particular, the objective lens) play a significant role in determining the effective reflectance (R_{eff}) and hence total optical power of the BI spot. The total power contained in the BI spot for a given combination of mirror and operating wavelength can be expressed as,

$$P_{BI} = R_{eff} P_{op}, \tag{3.1}$$

where P_{op} is the optical power produced by the laser diode at a given current. The values of R_{eff} for all mirrors at three operating wavelengths ($\sim$800 nm, $\sim$900 nm, and $\sim$1000 nm) were calculated as follows. First, the optical power was measured at three locations along the beam path – immediately after the laser (P_{op}), before the mirror P_2, and after the mirror P_3 (Fig. 3.5). With the assumption that the objective lens offers equal transmissivity in both incident beam directions, R_{eff} is estimated as,

$$R_{eff} \approx \left(\frac{P_2}{P_{op}}\right)^2 \left(1 - \frac{P_3}{P_2}\right). \tag{3.2}$$

However, aberrations along the 4F feedback branch arising from the shape of the lenses and

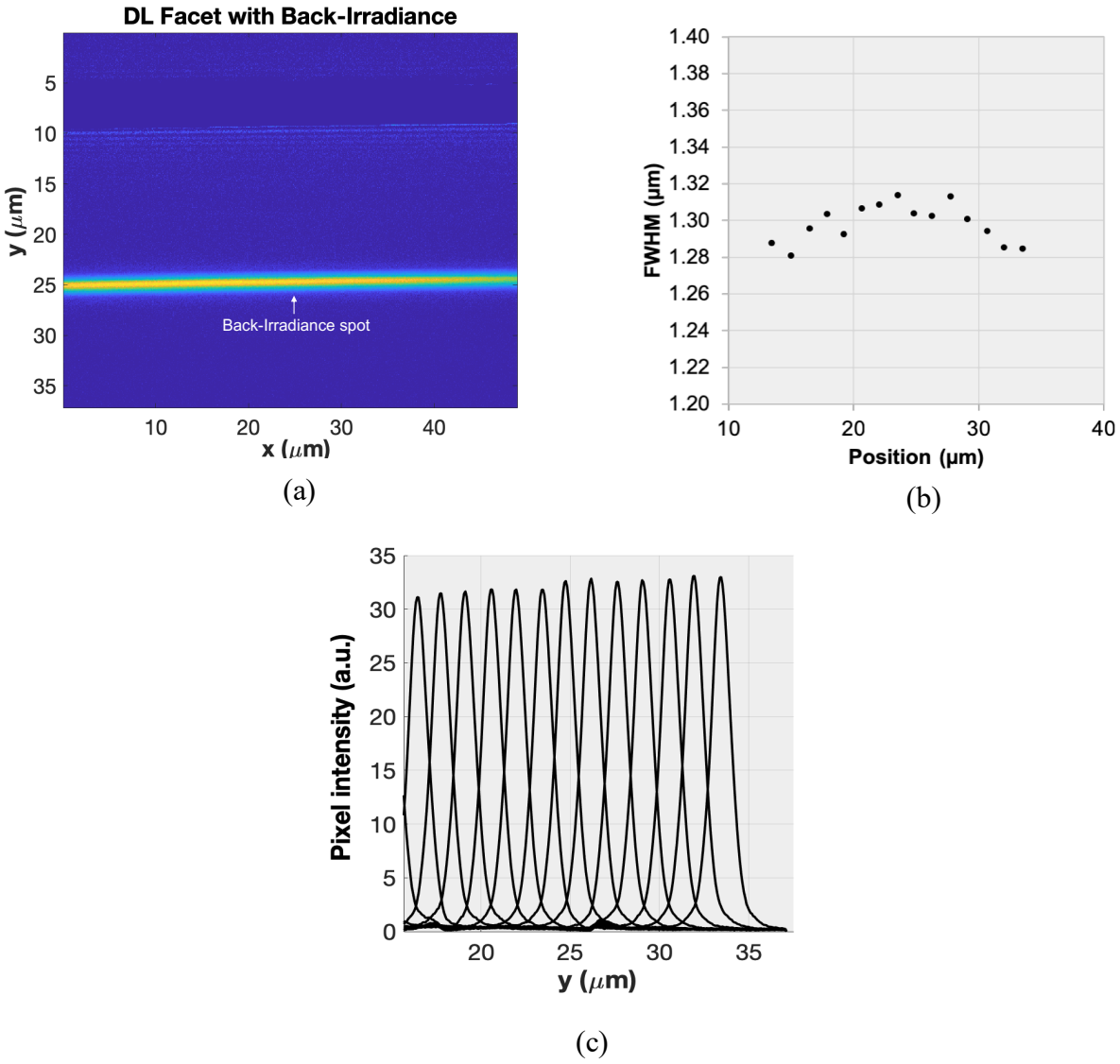

Figure 3.4: (a) BI spot positioned deep in the GaAs substrate. Outgoing laser emission has been subtracted from the image to remove noise. (b) Width of BI spot (FWHM) is consistent for a range of BI spot positions along the fast axis of the diode laser. (c) BI spot intensity profiles for a range of BI positions along the fast axis direction (integrated in the slow axis direction). The peak beam intensity remains mostly constant with position.

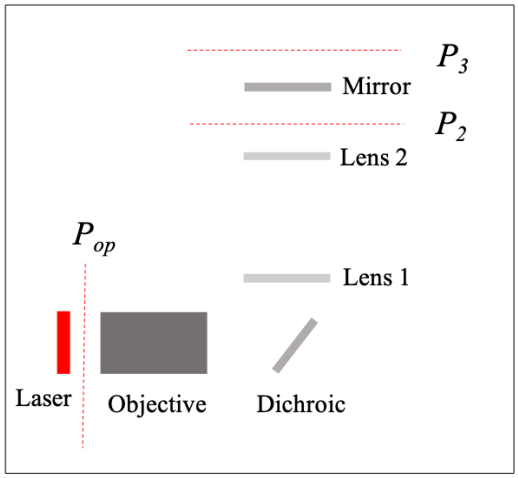

Figure 3.5: Schematic for estimating R_{eff} values of feedback mirrors. Measurement of optical powers at three distinct locations along the beam path can be used to estimate the power of the back-irradiance spot.

flatness of the mirrors result in some degree of vignetting in the beam as it passes through the objective lens the second time. This results in slightly higher transmission loss through the objective on the return leg, causing the actual value of R_{eff} to differ slightly from the value calculated using Eq. 3.2. To correct for this effect, an additional experiment is performed by using the measured intensity of the BI spot in the images captured by the CCD camera; this experiment is performed as follows.

First, an image of the outgoing laser beam was taken at an integration time T_1 such that the pixels at the laser beam location are just below saturation. The output laser beam power P_{laser} is proportional to the integral of the recorded intensity profile. The integration time was then increased to T_2 which causes the pixels at the BI spot location (visible in the substrate) to just barely approach the saturation limit. The BI beam power P_{BI} is proportional to the integral of the recorded intensity profile. This measurement is corrected for the reflectivity of the GaAs substrate (R_{GaAs}) at the laser emission wavelength to represent the true back-irradiance beam power. From this, R_{eff} is calculated as follows,

Nominal mirror reflectance	∼800 nm	∼900 nm	∼1000 nm
10%	1.40%	2.39%	1.45%
30%	7.50%	6.46%	4.12%
50%	15.50%	10.98%	6.73%
70%	21.76%	14.94%	10.31%
90%	25.30%	18.19%	14.43%

Table 3.1: Effective Mirror Reflectances : Measured R_{eff} values of feedback mirrors at ∼800 nm, ∼900 nm and ∼1000 nm operating wavelengths. R_{eff} value provides a direct ratio of feedback to outgoing optical power, taking all system losses into account.

$$R_{eff} = \frac{P_{BI}}{P_{laser}} \frac{T_1}{T_2} \frac{1}{R_{GaAs}}. \tag{3.3}$$

R_{eff} was measured for all mirrors using Eq. 3.3 and its value found to differ from the estimate calculated using Eq. 3.2 by an average of 6%. Table 3.1 details the R_{eff} value measured for all dielectric mirrors at all operating wavelengths. Each entry is the reported average as measured at varying diode operating current levels ranging from 1 A to 4 A.

3.3 Devices Under Test

The diode lasers under test are 3.5 W rated, broad-area single emitters with a 180 μm stripe width and 1500 μm cavity length. The devices exhibit a threshold current of $I_{th} \approx 0.65$ A, below which they produce negligible optical power. The diode structures are epitaxially-grown on GaAs substrates, and the wafers are fabricated following standard processes. The device emitting near 800 nm is transverse magnetic (TM)-polarized and is based on the InGaAsP material system with tensile-strained quantum wells, while those emitting near 900 nm and 1000 nm are transverse electric (TE)-polarized and are based on the InAlGaAs material system with compressively strained quantum wells. In all three designs, the quantum well active region is surrounded by an optical waveguide approximately 1 μm thick which itself is surrounded by doped cladding layers of appropriate thickness. The chips are soldered junction-down to industry standard CuW C-mount heat sinks using AuSn solder. Images of the device at three different length scales are shown in Fig.

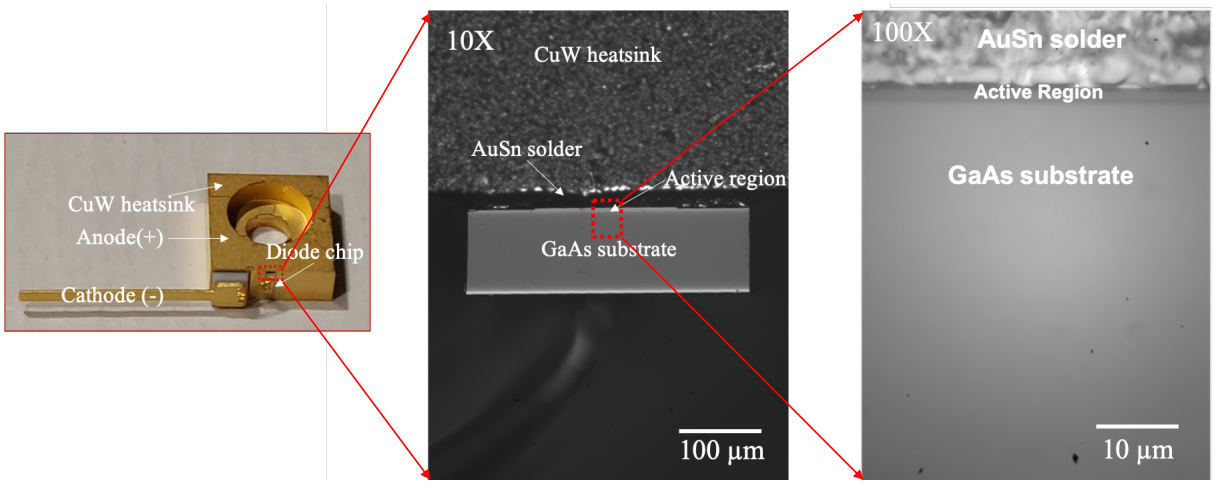

Figure 3.6: (a) C-mount diode laser (b) Image of the diode laser at 10X magnification. The epitaxial layers are grown on GaAs substrate and soldered to a CuW heat sink. (c) The image of the diode laser at 100X magnification. The thin ($\sim$2 μm) active region strip can be seen between the solder and the substrate.

3.6.

It is worth noting that the magnitude and configuration of strain in the quantum well region plays a significant role in determining the operating characteristics of the diode laser device. Strain-induced changes in band structure affect the emission wavelength, polarization and threshold current of the device. In diode lasers based on unstrained InGaAsP and InAlGaAs material systems, the band structure is characterized by a conduction band with low effective mass, a degenerate valence band at the zone center (heavy hole and light hole bands) and a spin split-off band. The introduction of strain breaks the degeneracy at the zone center and splits apart the heavy hole and light hole bands. In the case of compressive strain, the heavy hole levels are brought up into the gap and the polarization is TE due to electron-heavy hole recombination. Conversely, tensile strain leads to the light hole levels being brought up into the gap and the emission is TM-polarized due to electron-light hole recombination.

The devices described above are tested one emitter at a time. The emitter is mounted on a laser mount (Arroyo Instruments 242) that has an integrated feedback-controlled thermoelectric cooler (TEC). The device is bolted down onto the TEC and the TEC temperature is set at 25°C

for all tests. No thermal interface material is used between the TEC and the device. Basic device characterization is performed to measure the diode output optical power P_{op} and voltage V as a function of bias current I. The optical power is measured using a thermopile-based power meter (Gentec-EO) and the voltage was measured using an Agilent multimeter across the diode laser terminals. We also measure the junction temperature rise ($\Delta T_{junction}$) for the device by tracking the emission spectrum as a function of operating current. $\Delta T_{junction}$ is an estimate of the overall temperature increase of the device as opposed to the temperature increase at particular locations within the device. As the current increases and the device heats up, the thermally-induced band gap shrinkage leads to an increase in the wavelength of the emission. The degree of red-shift is approximately linear with the change in temperature and has been estimated at 0.26 nm/°C for the $\sim$ 800 nm device. Hence, by measuring the red-shift in the emission spectrum, $\Delta T_{junction}$ can be ascertained. The slope of the variation of $\Delta T_{junction}$ with waste heat is the thermal resistance of the system (right panel of Fig. 3.7) which is also indicative of the effectiveness of the heat sink. The device characteristics, both before and after thermoreflectance experiments with back-irradiance (detailed in section 3.4) are shown in Fig. 3.7.

3.4 Thermoreflectance with Back-Irradiance Experiments

3.4.1 Experimental Plan

In this section, we describe the experimental plan to understand the effect of back-irradiance on the behavior of high power diode lasers (device design described in section 3.3). The approach described here can be applied to study diode lasers of any design. Our general approach is to carry out non-destructive testing of diode lasers and investigate the thermal response at the facet. We use the CCD-thermoreflectance setup described in section 2.3 to capture thermal maps of the diode laser facet for various back-irradiance power levels and positions on the facet.

As mentioned before, the position of the BI spot is controlled by mounting the dielectric mirror on a motorized kinematic mount. In order to make inferences regarding the effect of BI spot

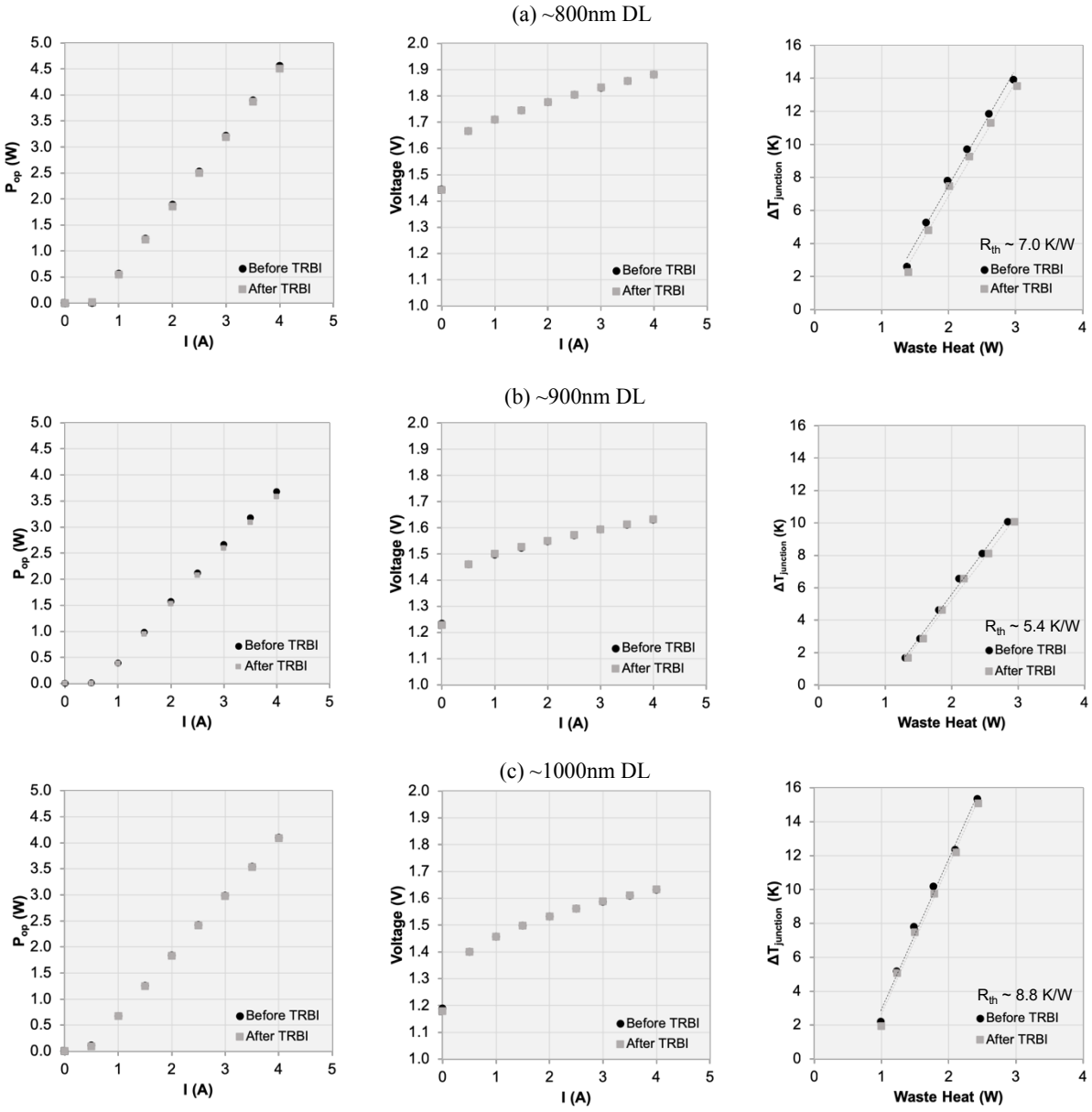

Figure 3.7: Out-coupling optical power versus bias current (left panel), voltage versus bias current (middle panel), and junction temperature rise versus waste heat (right panel) for the (a) ∼800 nm device, (b) ∼900 nm device, and (c) ∼1000 nm device. The PIV characteristics are measured before and after thermoreflectance with back-irradiance (TRBI) experiments to ensure that the device integrity is not compromised during the experiment. Also, a linear fit of the junction temperature versus waste heat generation is used to determine the thermal resistance of the laser mount.

position on the thermal response, the BI position needs to be calibrated with respect to the quantum well (QW) location. This calibration is performed by sweeping the BI spot in the vicinity of the active region in small steps while monitoring the emission spectrum. When the BI spot is perfectly aligned with the quantum well, the coupling of back-irradiance into the waveguide layers leads to a reduction in the threshold current. The reduction in the threshold current causes the peak of the carrier distribution to occur at a lower energy level, resulting in laser emission at a longer wavelength (red-shift). Hence, the mirror position which leads to the maximum red-shift in the emission spectrum, corresponds to the location of the QW and is assigned $x = x_0 = 0$ μm (x_0 is the QW location and x is the BI spot position relative to the QW location). In order to vary the BI power, appropriate dielectric mirror of desired R_{eff} value at a particular wavelength is chosen (detailed in section 3.2).

The thermal response of the diode laser is recorded by capturing the thermoreflectance maps of the facet. Since the area of the facet near the quantum well (where the photon flux is highest) is the most vulnerable part of the device, the temperature of this region is key to understanding BI-induced degradation. Hence for all experiments, a temperature profile of the active region is calculated along the slow axis direction, using the peak temperature values at every fast axis location along the emission strip. The temperature rise near the quantum well at the facet (ΔT_{QW}) is calculated by averaging this temperature profile.

A single thermoreflectance with back-irradiance (TRBI) experiment involves operating the diode laser at injection currents in the range of 1 A - 4 A and 1 A - 2 A, for two respective BI power levels - $R_{eff} \approx 9\%$ and 17%. Currents greater than 2 A led to immediate COD in $\sim$800 nm emitters at $R_{eff} \approx 17\%$. For each combination of experimental conditions (i.e. current and R_{eff} value), the BI spot is placed at 27 locations between x = –10 μm (deep in the solder) to x = +40 μm (deep in the substrate). ΔT_{QW} value associated with each BI location is calculated using the method described above. A schematic of the diode laser facet under back-irradiance is depicted in Fig. 3.8. In order to make meaningful comparisons of ΔT_{QW} across diode lasers with different emission wavelengths, feedback mirrors were chosen such that the BI power reach-

ing the facet is comparable within ∼15% across all wavelengths. The subsequent sections detail the results of these measurements for diode lasers emitting near 800 nm, 900 nm and 1000 nm, fo which the GaAs substrate (band gap ≈ 870 nm) is strongly absorbing, weakly absorbing, and nearly non-absorbing, respectively. (Fig. 3.9).

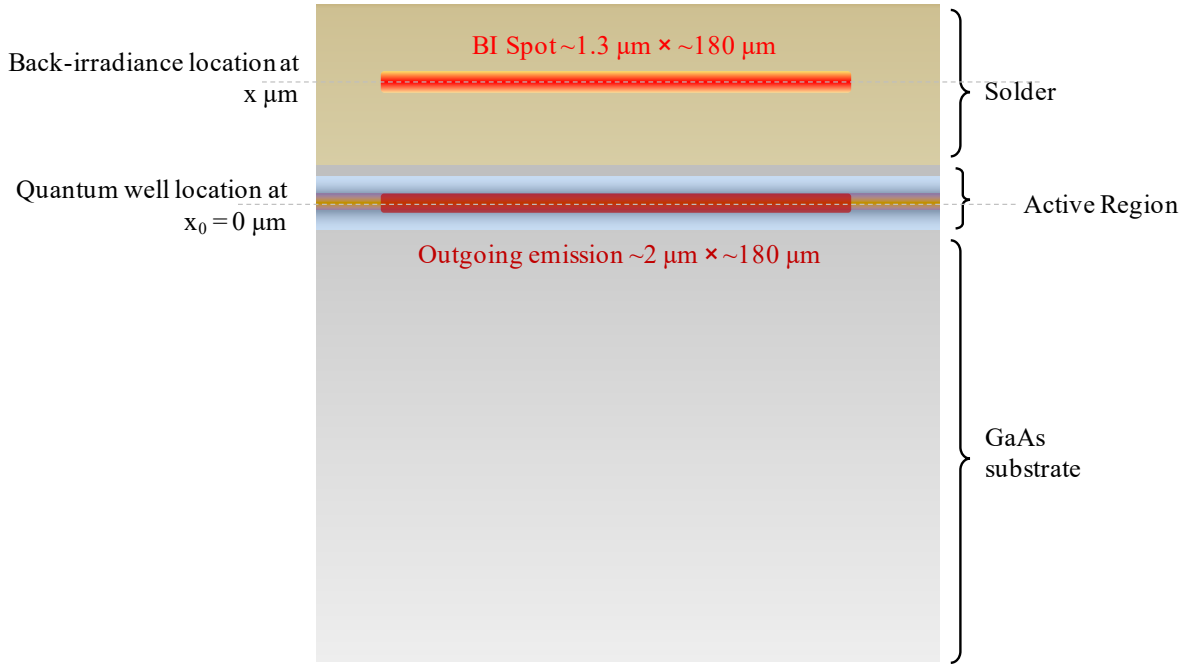

Figure 3.8: A schematic of the front view of the diode laser facet under back-irradiance. The position of the BI spot is controlled by a motorized kinematic mount which holds a mirror of variable reflectance to control the back-irradiance power. x represents the position of the BI spot and is negative when the BI is positioned in the solder, positive when it is positioned in the subsrate and zero when it is perfectly aligned with the quantum well.

3.4.2 800 nm Diode Lasers

Figure 3.10 shows the two-dimensional (2D) temperature rise maps of the facet for a diode laser emitting near 800 nm as the BI spot is located in the solder (x = –10 μm), close to the QW in the substrate (x = +2 μm), and deep into the substrate (x = +20 μm). Residual thermal expansion in the fast axis causes measurement artifacts in $\frac{\Delta R}{R}$ signal due to the rough surface of the solder. Consequently, the solder region has been set to zero in the temperature map. A bright hotspot can be observed centered at the BI location indicative of the fact that GaAs is strongly absorbing at this

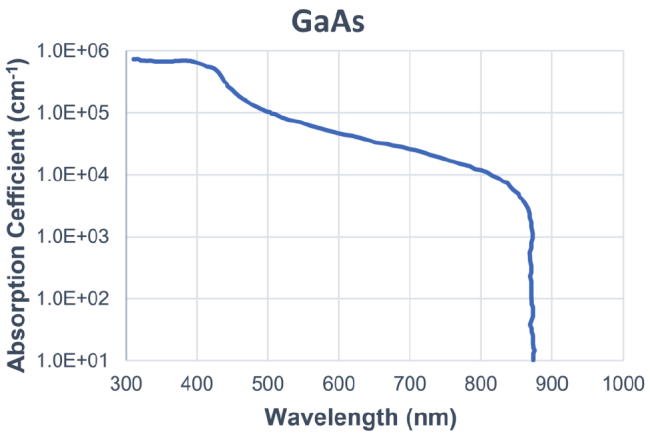

Figure 3.9: Room temperature absorption coefficient values for undoped GaAs as a function of incident emission wavelength. Image courtesy of ref. [14].

wavelength. The peak hotspot temperature is higher for x = +2 μm compared with x = +20 μm, possibly because the diffusion of heat close to the epi-layers is hindered by thermal resistance at the substrate/epi interface and/or low thermal conductivities within the epi layers.

Figure 3.11 depicts how ΔT_{QW} evolves as the BI spot is swept in the direction perpendicular to the epi-layer stacking direction. For this emitter, a sharp temperature rise is observed when the BI is centered $\sim$2 - 2.5 μm from the QW into the absorbing substrate. This critical location maximizes ΔT_{QW} since at this location a large fraction of the spot is within the substrate and the heat generated is quite close to the QW. Moving the BI spot closer to QW reduces ΔT_{QW} due to reduced absorption, while moving the BI spot further into the substrate also leads to a drop in ΔT_{QW} due to the absorption hotspot being located further from the QW. Remarkably, when the laser is run at 3 A with 7.5% effective back-reflectance level, ΔT_{QW} with BI (29.3 K) nearly triples that of the free-running (i.e. without back-irradiance) case (11.4 K). It is also worth noting that a secondary peak in ΔT_{QW} appears when the BI spot is $\sim$3 μm above the QW in the metallic solder.

3.4.3 900 nm Diode Laser

Figure 3.12 shows the 2D temperature rise map of the facet for three distinct BI spot locations at x = –3 μm, +2 μm and +20 μm. The substrate heating is minimal due to low absorptivity of GaAs

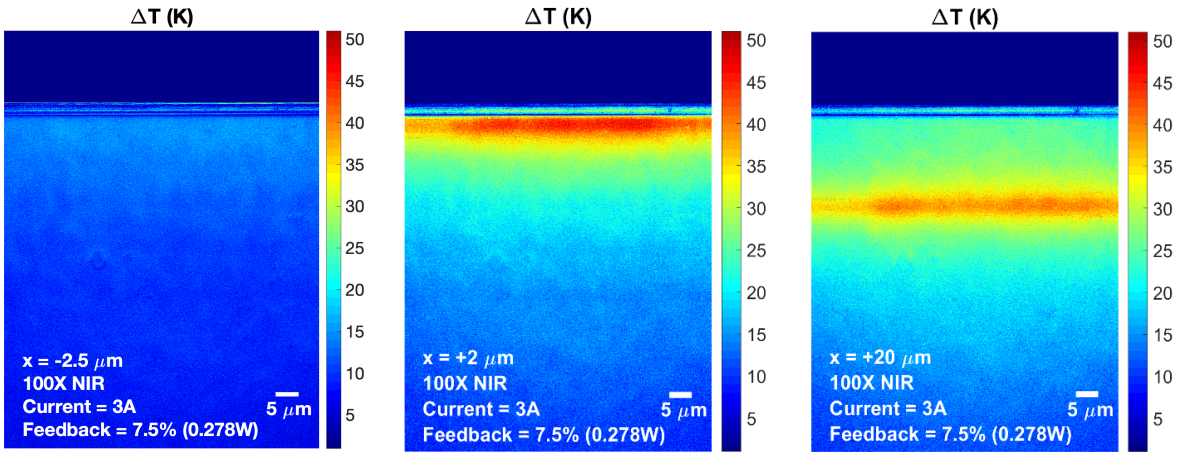

Figure 3.10: 2D temperature maps of the facet when the BI spot is located 2.5 μm above the QW in the solder (left), 2 μm below the QW in the substrate (middle), and deep into the substrate (right). The text at the bottom-left corner corresponds to the position of the BI spot, the magnification of the objective, the drive current, BI feedback level, and BI power reaching the facet (shown in brackets)

around 900 nm. Figure 3.13 depicts how ΔT_{QW} varies as the BI spot is swept in the direction perpendicular to the epi-layer stacking direction. A 50% nominal reflectance mirror is used to yield R_{eff} = 10.98%, which compensates for the lower P_{op} of the diode laser emitting around 900 nm at 3 A compared to that emitting around 800 nm at 3 A, resulting in a P_{BI} of 0.29 W which is close to the 0.28 W BI power for the previous case. For this device, the ΔT_{QW} corresponding to BI positioned near substrate/epi-layer interface becomes much less pronounced. This can be seen by its comparable magnitude with the secondary peak close to the solder/epi-layer interface; which can be attributed to the much smaller absorption coefficient of GaAs around 900 nm. It is also worth noting that for the solder critical location, the difference between ΔT_{QW} with BI and without BI, is higher around 900 nm compared to 800 nm diode laser.

3.4.4 1000 nm Diode Laser

Around 1000 nm, GaAs has an extremely small absorption coefficient, so we anticipate the additional temperature rise in the active region due to substrate absorption to be negligible. It can be seen from Fig. 3.14 that the active region is hotter when BI is located at the solder/epi-layer

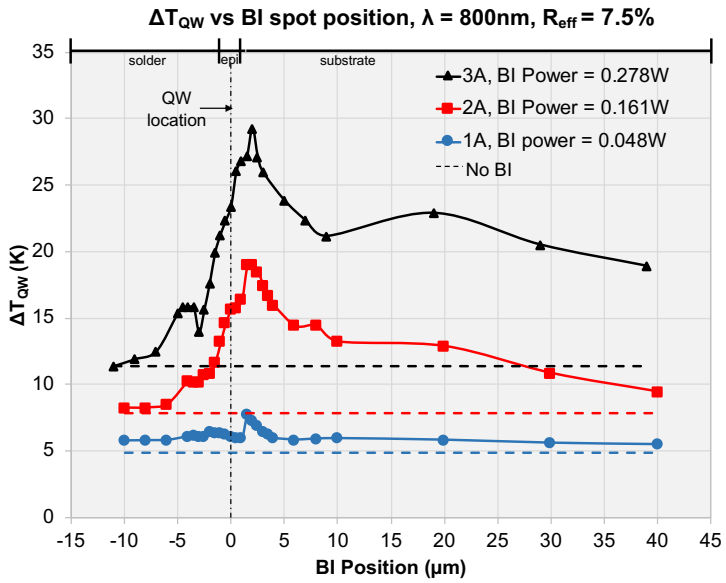

(a)

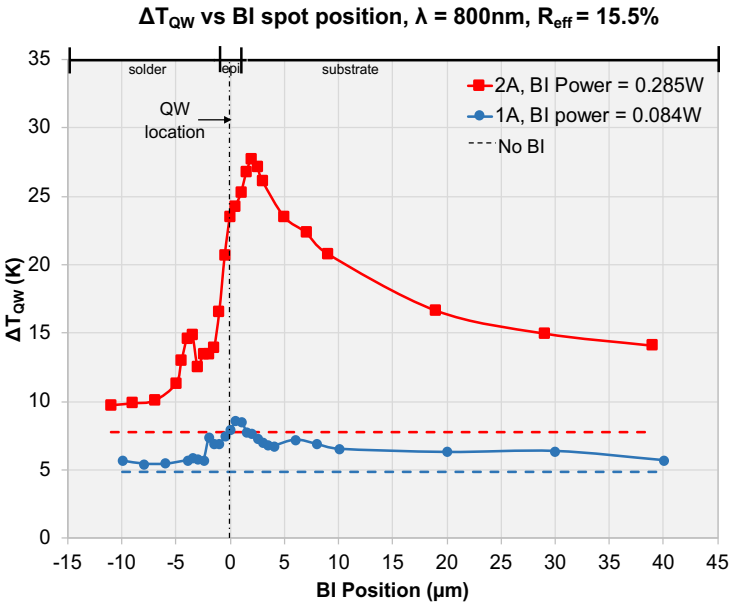

(b)

Figure 3.11: ΔT_{QW} versus the BI spot position with respect to the quantum well location for the ~800 nm device with the direction going towards the substrate being positive, at feedback levels of (a) R_{eff} = 7.5% and (b) R_{eff} = 15.5%. For all currents and feedback levels tested, a peak in ΔT_{QW} can be observed at $x \approx +2.5$ μm, corresponding to a critical location in the substrate close to the epi-layer/substrate interface at which the device is potentially most susceptible to COD. A small peak is also observed at $x \approx -3\mu$m. The dotted lines correspond to the ΔT_{QW} for the case without back-irradiance.

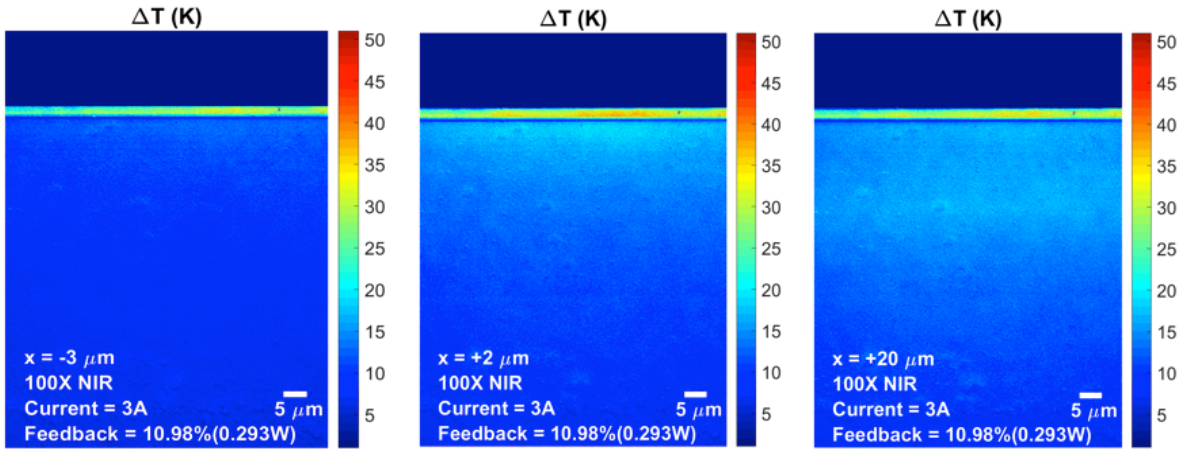

Figure 3.12: 2D temperature maps of the facet for the ∼900 nm diode laser when the return spot is 3 μm above the QW into the solder (left), 2 μm below the QW into the substrate (middle), and 20 μm into the substrate (right).

interface (left panel) rather than at the epi-layer/substrate interface (middle panel). In Fig. 3.15 we can clearly see that the peak due to substrate absorption becomes extremely weak and much less pronounced than the secondary peak of the metallic solder. In addition, the difference between ΔT_{QW} with BI and without BI for the solder critical location intensifies further and is nearly three-fold compared to the case of ∼800 nm emitter. This result is consistent with the observations by Rauch et al. in their single-point thermoreflectance study of 950 nm TE-polarized high-power diode lasers [86].

In summary, we observe that ΔT_{QW} for the n-side substrate critical location diminishes as emission wavelength increases while it simultaneously intensifies for the critical location on the p-side metallic solder. Although the existence and wavelength dependence of substrate critical location is well understood, the origin and behavior of the p-side solder critical location is not entirely clear. As previously noted, the presence of BI at the solder appears to impact the facet temperature by a greater amount in the TE-polarized ∼900 nm and ∼1000 nm devices as compared to the ∼800 nm device (TM-polarized). The analysis for exploring the cause of this phenomenon is presented in detail in the next section.

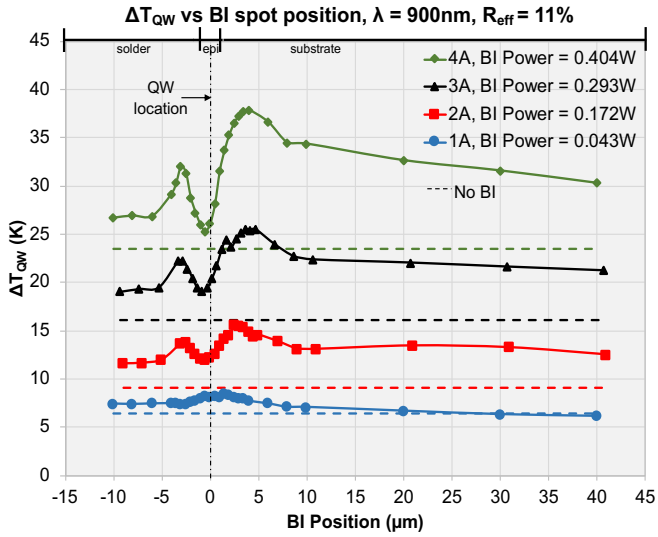

(a)

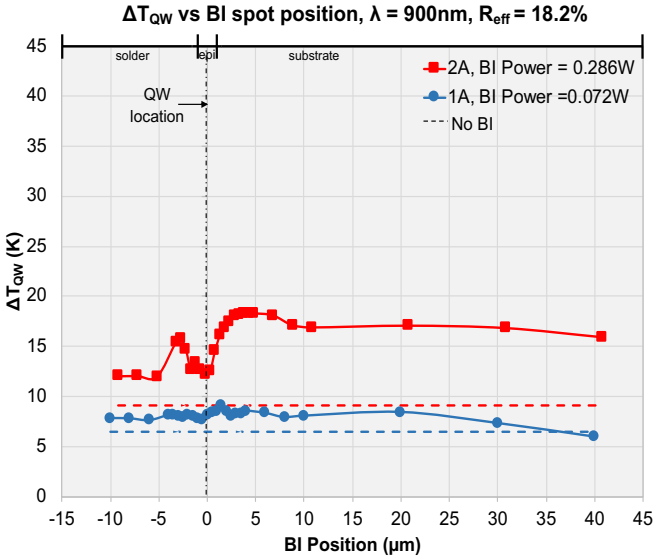

(b)

Figure 3.13: ΔT_{QW} versus the BI spot position with respect to the quantum well location, for the $\sim$ 900 nm device with the direction going towards the substrate being positive, for TRBI experiment with (a) R_{eff} = 11% and (b) R_{eff} = 18.19%. The peak in ΔT_{QW} observed at $x \approx$ +2.5 μm becomes much less pronounced due to weak absorption of $\sim$900 nm light by the GaAs substrate. The secondary peak in the solder, near the solder/epi-layer interface ($x \approx$ –3 μm) becomes almost comparable (although still lower) to the primary peak caused by substrate absorption.

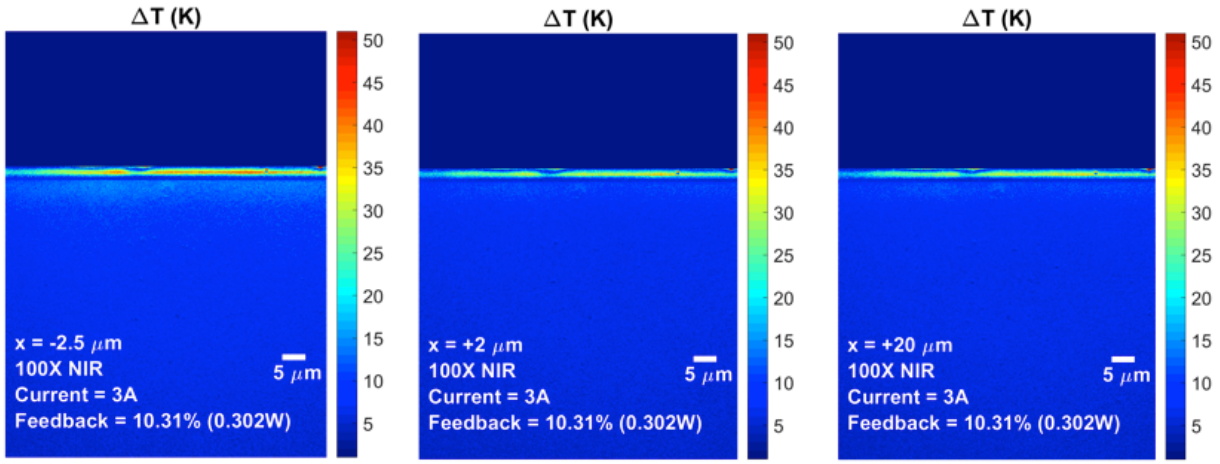

Figure 3.14: 2D temperature maps of the facet for the ∼1000 nm diode laser when the BI spot is positioned 3 μm above the QW into the solder (left), 2 μm below the QW into the substrate (middle), and 20 μm into the substrate (right).

3.4.5 Effect of Polarization on Back-Irradiance Induced Heating

To analyze the effect of polarization on BI-induced heating, the contribution of back-irradiance to ΔT_{QW} was calculated as the difference of the measured ΔT_{QW} with BI and ΔT_{QW} without BI (Fig. 3.11, 3.13, 3.15) at 3 A operating current, with the BI positioned at the solder critical location. The values are listed in Table 3.2 for all three wavelengths alongside other relevant parameters. We note that for nearly the same incident BI power, the values of ΔT_{QW} are ∼40% higher for 900 nm and ∼200% higher for 1000 nm emitters compared to 800 nm emitters. Incidentally, 900 nm and 1000 nm diode lasers are TE-polarized while 800 nm is TM polarized. These observations suggest that light absorption and subsequent heat dissipation processes within the metallic solder might be a function of the polarization of incident emission (in addition to emission wavelength).

Emission wavelength (nm)	BI power at 3 A (W)	BI contribution to ΔT_{QW}	Polarization
∼800	0.28	4.48	TM
∼900	0.29	6.11	TE
∼1000	0.30	13.51	TE

Table 3.2: Back-irradiance contribution to ΔT_{QW} for solder critical location

To further investigate this hypothesis, finite-difference time-domain simulations of Maxwell's equations and extraction of light absorption was carried out for a two-dimensional model of the

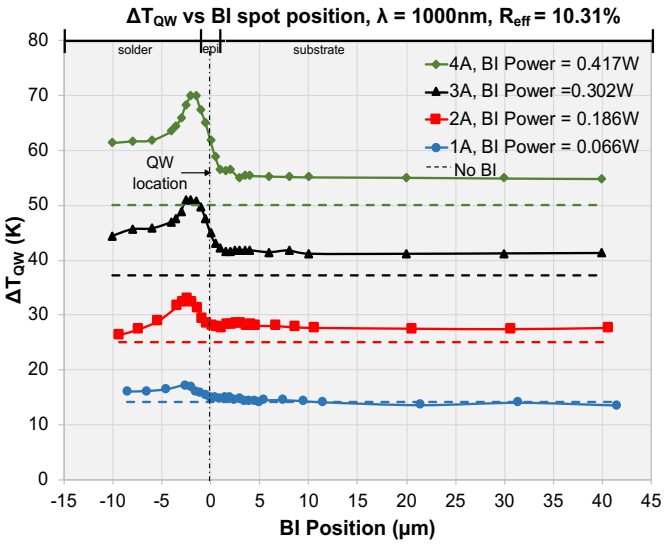

(a)

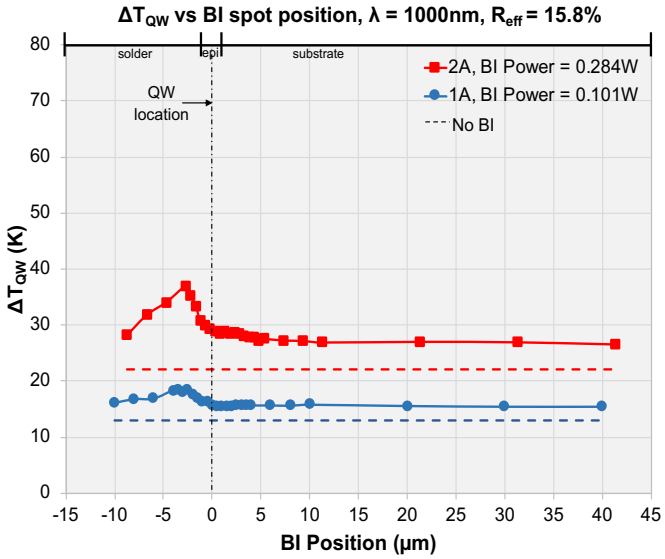

(b)

Figure 3.15: ΔT_{QW} versus the position of the BI spot with respect to the quantum well location for the ∼1000 nm diode laser, with (a) R_{eff} = 10.31% and (b) R_{eff} = 15.80% . The peak in ΔT_{QW} due to BI absorption in the substrate (at $x \approx$ +2.5 μm) becomes very weak due to negligible absorption of ∼1000 nm light by the substrate. The secondary peak in the solder, near the solder/epi-layer interface ($x \approx$ –3 μm) becomes significantly more pronounced in comparison.

device (in collaboration with the Lawrence Livermore National Lab). The local device structure within the area of interest is shown in Fig. 3.16 (a), although the complete simulation domain spans 7 μm in the fast-axis direction and 70 μm along the longitudinal (emission) direction of the diode. The complex refractive indices of the various metallic, dielectric, and semiconductor layers are appropriately modelled for the 800 nm diode laser design. A Gaussian beam with waist ω_0 = 2 μm located in air 0.15 μm away from the facet is incident on the structure and centered 1 μm above the quantum well in the p-metal. The calculation is performed and normalized to 1 W incident BI power. While the actual 800 nm laser device is TM-polarized, the calculation is performed for both TM- and TE-polarized incident light. Here, TM-polarization corresponds to the polarization state where the magnetic field is pointing in the plane of the quantum well and the electric field is pointing in the fast axis direction. Figure 3.16 (b) and (c) show the locally absorbed power density on the device surface for TE- and TM-polarized light under the back-irradiance conditions described above. It is evident that for TE-polarized light, intense light absorption occurs at the corner of the p-metal due to the localization of optical intensity caused by high electric field at the sharp corner. In contrast, the TM-polarized light appears to distribute along the edges of the metal (in both x and y) and results in delocalization of the absorption.

The strong localization of absorption in the TE case near the corner of the p-metal layers is attributed to the high electric field intensity which naturally arises at sharp corners (charge repulsion and Gauss's Law). The origin of the delocalization of this effect is not yet well understood, however it is clear that some effect is causing the high electric field to be spread out along the metallic edges. One effect that may explain this observation is the excitation of surface plasmons. The surface plasmon effect would permit incident TM-polarized light (but not TE-polarized light) to couple to a guided wave which propagates along the metal-insulator edges. Figure 3.17 plots the fraction of overall absorption occurring at the metal corner (area within yellow box of Fig. 3.16 (b)) for several BI positions. It can be seen that a maximum in absorption is achieved when the BI spot is located $\sim$1.5 μm from the QW in the p-metal which is consistent with our experimental results for the longer wavelength TE-polarized devices. In addition, the local absorption is $\sim$7-

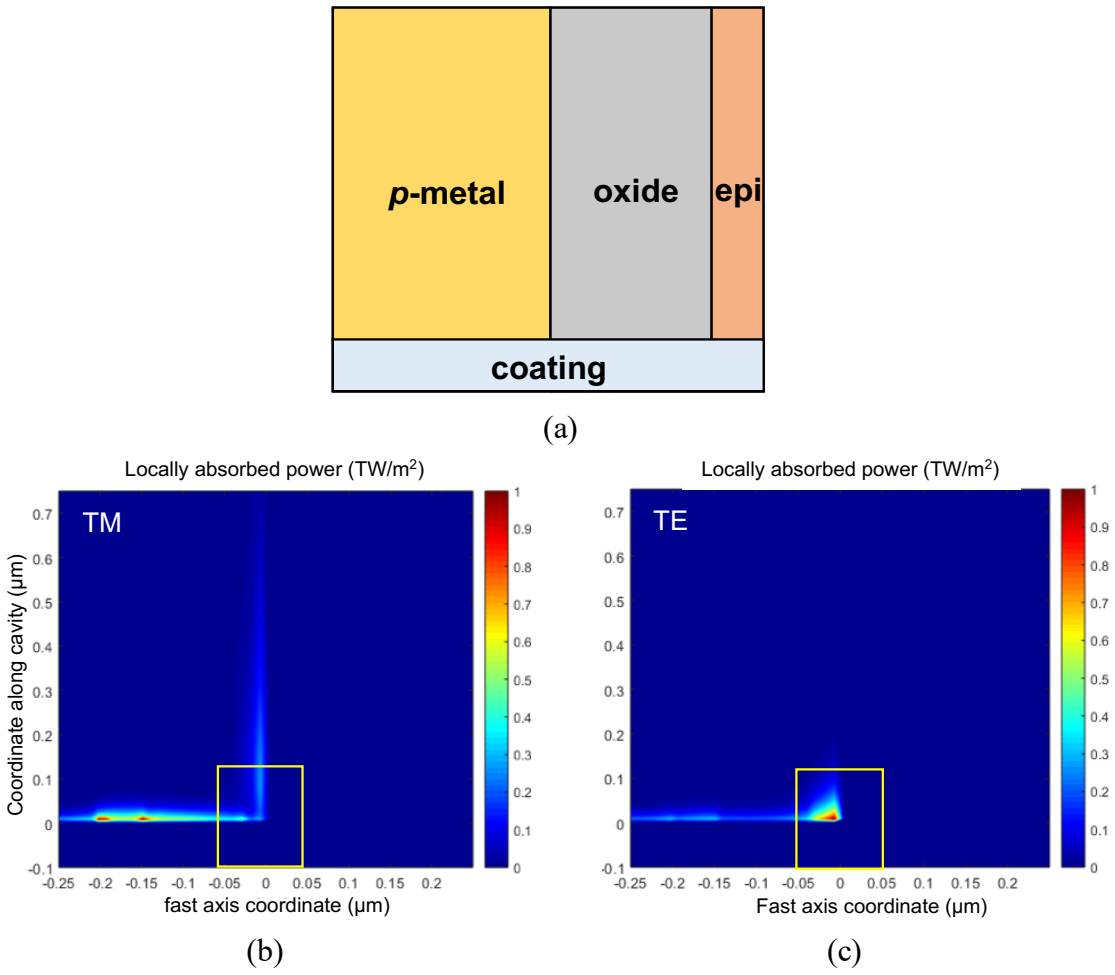

Figure 3.16: Schematic of the materials comprising the diode laser near the metal/epi interface. Locally absorbed power on device surface with the BI positioned 1 μm away from the quantum well in the p-metal for (b) TE and (c) TM-polarized incident light. Light absorption is highly localized for TE-polarized light while distributed absorption is facilitated for TM-polarized light, possibly by a surface plasmon.

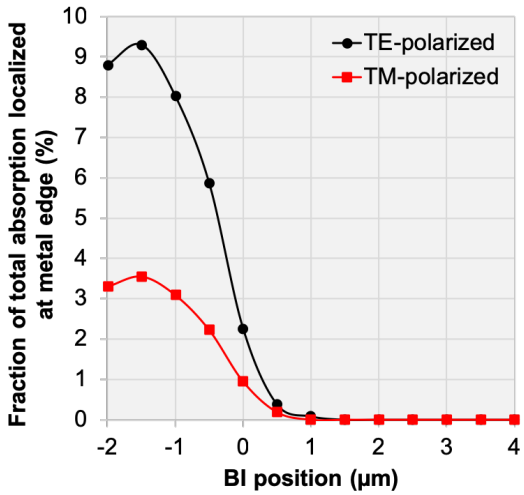

Figure 3.17: Fraction of overall absorption occurring at the metal corner, represented by the area within the yellow box on Fig. 15 (b) and (c), as a function of BI position. The absorption is maximized for a BI position 2 μm away from the QW which is consistent with experimental observations.

fold stronger for TE-polarized light compared to TM-polarized light. This phenomenon becomes clearer when we look at the electric field distribution in the materials near the metal/oxide interface (Fig. 3.18). In case of TE-polarized back-irradiance, a strong electric field arises in the dielectric at the corner of the p-metal. On the contrary, for TM-polarized light, propagation of the electric field along the metal-oxide interface (into the cavity direction) is observed.

This analysis suggests that TE-polarized back-irradiance directed into the p-metal and solder of the emitter will result in higher ΔT_{QW} compared to TM-polarized back-irradiance. As a result, TE-polarized diode lasers emitting around 800 nm are predicted to be doubly susceptible to back-irradiance induced COD as both the substrate and p-metal critical locations can absorb significantly. On the other hand, TM-polarized lasers operating at wavelengths longer than the GaAs band edge are predicted to be much more robust to back-irradiance induced failure.

Through this work, we have investigated the conditions under which high-power diode lasers emitting in the wavelength range of 800 – 1000 nm are most susceptible to fail due to back-irradiance of emitted light. Critical locations were identified on the diode laser facets $\sim$ 2 μm

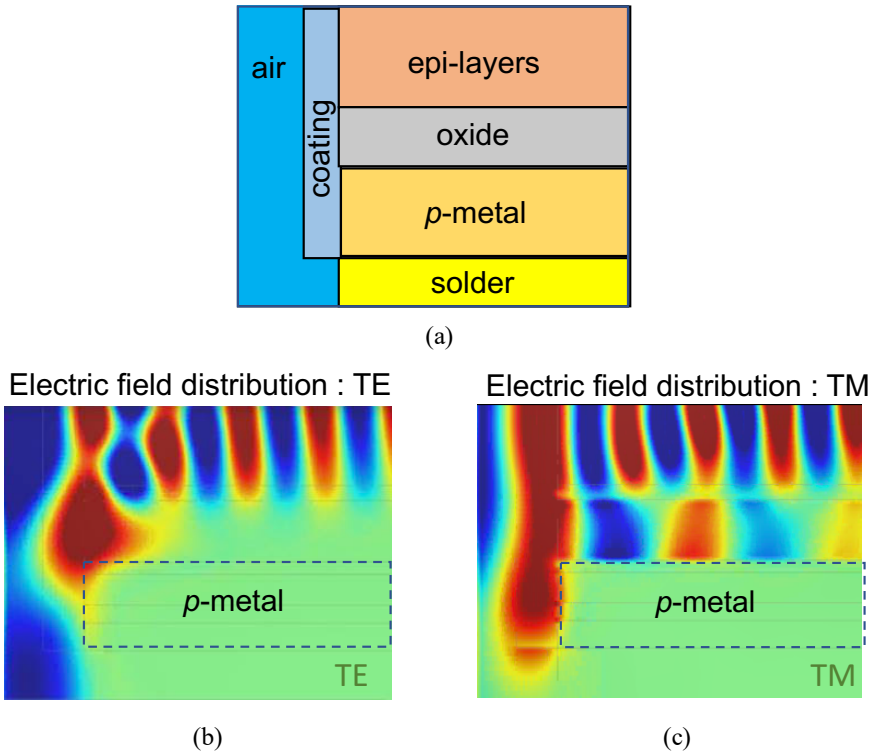

Figure 3.18: (a) Schematic of the materials comprising the diode laser near the metal/epi interface. (b) Electric field distribution for TE-polarized incident light shows the presence of a strong electric field at the metal edge (c) Electric field distribution for TM-polarized incident light shows the electric field being distributed away from the metal edge.

($\sim$ 1.5$\times$ the FWHM of the BI spot) away from the quantum well in the solder and the substrate, such that when the back-irradiance is positioned in these locations, the temperature rise near the quantum well at the facet increases significantly. It was found that with only $\sim$7.5% of optical feedback, the facet temperature rise experiences a nearly three-fold increase at the rated current, and with $\sim$ 15% optical feedback, the devices undergo catastrophic optical damage at nearly half the rated current. Moreover, we found that the contribution of BI to facet temperature rise when it is positioned in the solder/p-metal is significantly mitigated if the emission is TM-polarized as opposed to TE-polarized.

CHAPTER 4

Facet Optical Absorption in Diode Lasers

4.1 Optical Absorption Induced Facet Heating

As described in chapter 1, one of the primary factors triggering COD in modern high-power diode laser devices is the non-radiative recombination of carriers at defects present on or near the outcoupling facet. These carriers are in-part produced by partial absorption of the laser emission incident at the facet (Fig. 4.1). The heat produced by non-radiative recombination leads to band gap shrinkage which in turn increases the degree of optical absorption and leads to generation of more free carriers which recombine non-radiatively, further increasing the facet temperature. Although it is generally known that elevated facet temperature, caused by absorption of emission at the facet, is a pre-condition for COD, it is difficult to ascertain the threshold value of optical absorption that triggers it. This is because the incident photon flux on the outcoupling facet is unknown and difficult to measure.

To investigate the effect of optical absorption on the thermal characteristics of high power diode laser facets, thermoreflectance imaging of the facet of a $\sim$800 nm diode laser is performed for injection currents ranging from 0.1 to 4 A. The diode laser device is of the same design as described in section 3.3, and the facet does not have any passivation layers. Figure 4.2 depicts the thermal images obtained at 0.5 A, 2 A and 4 A injection current for this device. The temperature rise near the quantum well ΔT_{QW} is calculated as described in section 3.4 for all current set points.

The waste heat produced within the device can be calculated as the difference of the input power (IV) and the optical power output of the device (P_{op}). Figure 4.3 plots the ΔT_{QW} as a function of

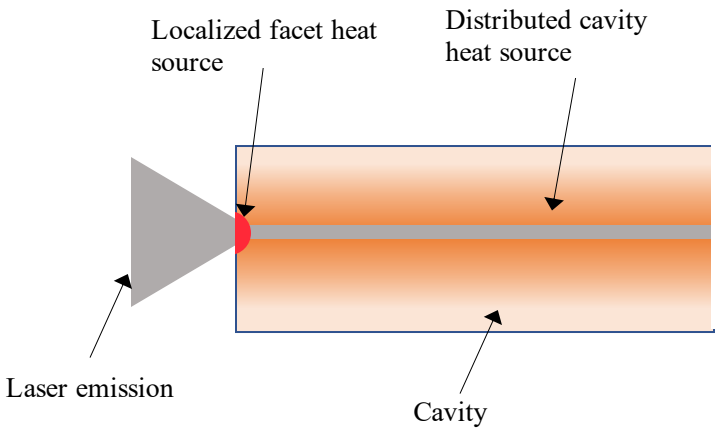

Figure 4.1: A schematic of the localized heat source created at the facets of high power diode lasers due to self-absorption of emission which is the primary driver of most facet degradation mechanisms.

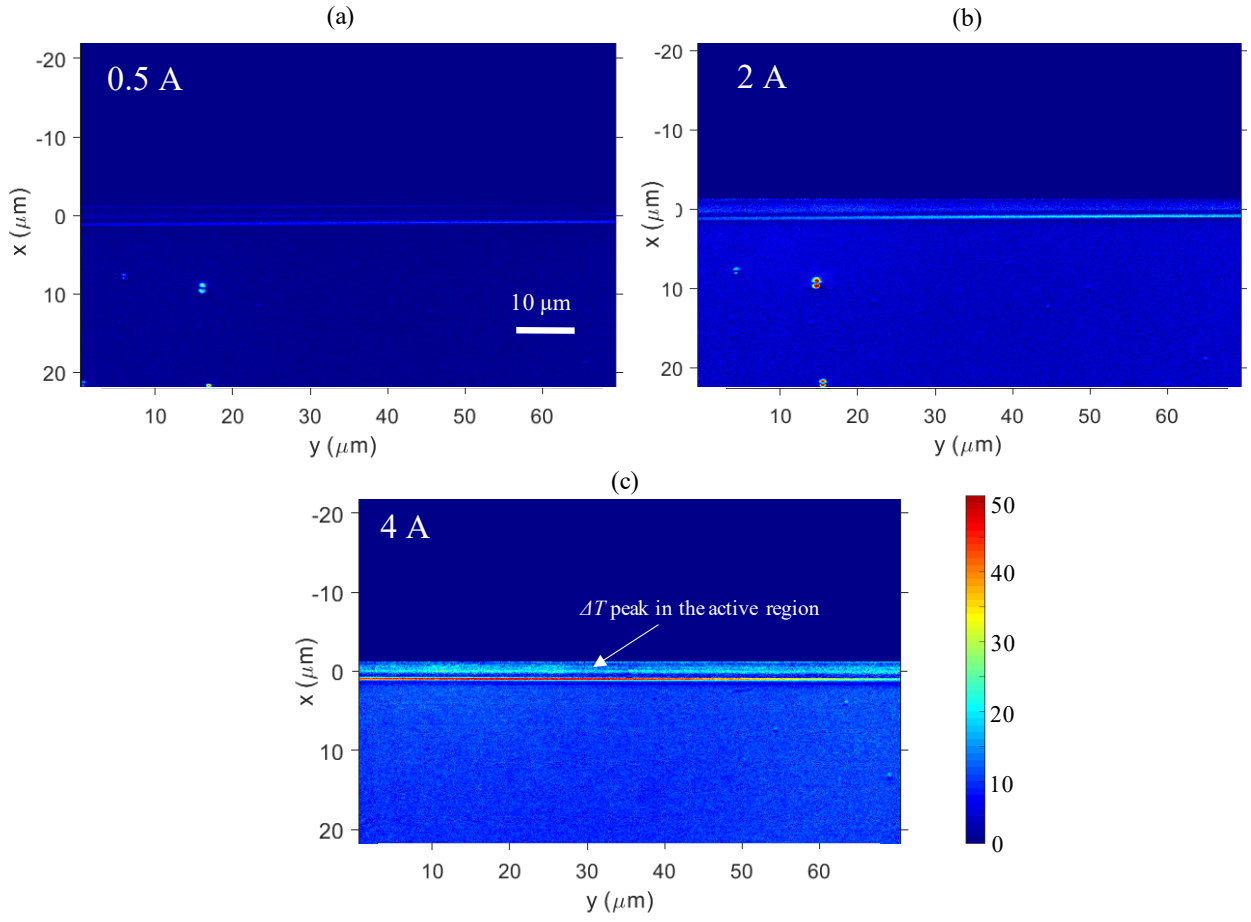

Figure 4.2: Thermal images of a ∼800 nm, non-passivated device operating at (a) 0.5 A, (b) 2 A and (c) 4 A injection currents.

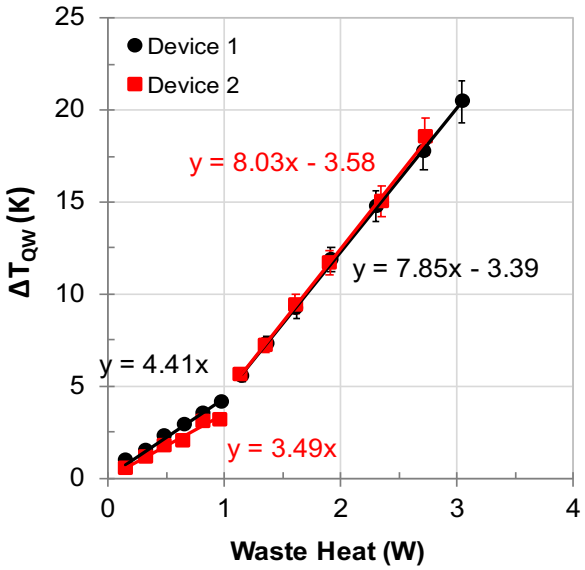

Figure 4.3: ΔT_{QW} as a function of waste heat for two different devices of the same design emitting near 800 nm wavelength.

the device waste heat for two devices of the same design. An abrupt change in slope is observed in the plot of ΔT_{QW} vs waste heat around 1 W. The devices exhibit a threshold current of ≈ 0.65 A which corresponds to ≈ 1 W of waste heat. Clearly, there is a contribution to the facet temperatures from a heat source that appears as the laser transitions from below-threshold to above-threshold operation. These observations can be explained by a small fraction of photons generated in the laser cavity that are re-absorbed at the outcoupling facet, leading to localized surface heating. A similar conclusion was made by Schaub [62] where point thermoreflectance measurements made along the top ridge of a diode laser emitting at 980 nm suggested the existence of a surface heat source at the outcoupling facet that led to high $\frac{\Delta R}{R}$ values close to the facet.

The presence of a surface heat source at the facet due to partial optical absorption raises some important questions such as how does the degree of optical absorption evolve as the diode laser ages, and if there exists a threshold value of optical absorption that serves as the necessary condition for COD. The ability to quantify optical absorption at the facet would enable tracking of device degradation over time and potentially help in understanding the conditions prior to COD. It would also enable rapid development of alternative passivation technologies and ultimately lead to

improved output power and reliability. In the next section, we describe some prior efforts and our approach to quantify the degree of optical absorption at the facets of high-power diode lasers.

4.2 Calculation of Facet Optical Absorption

Previous efforts to quantify facet absorption have been limited to point-based thermoreflectance measurements using a probe laser [58, 61, 62, 87, 88]. These point-based measurements have typically been performed by focusing a $\sim$1 mW probe beam focused onto a $\sim$1 μm-sized spot on the device that lies a few microns away from the quantum well [62]. In addition to probing a region that does not include the active region, this approach may generate a surface heat source at the probed location which has an intensity comparable to that created by the facet absorption of the diode laser's internal photon flux, introducing a constant offset in measured temperatures [61]. Moreover, point-based thermoreflectance measurements have typically used relatively long wavelength probe beams, yielding a spot size that is relatively large (compared to the thickness of the epitaxial layers and the significant temperature gradients near the active region) and thereby limiting the resolution and accuracy of the technique [61, 87]. The effectiveness of prior efforts has also been limited by parasitic effects observed in the reflectance signal, likely caused by photoelasticity, which can modify the reflection conditions at the facets of coated diode lasers due to mechanical stresses caused by thermal expansion coefficient mismatch [62]. As a result, measurement of facet absorption has been limited to situations where this absorption was impractically high and the reflectance signal was free from distortions, for example in the case of uncoated facets [62].

In this work, we use CCD camera-based thermoreflectance imaging (described in section 2.3) to generate thermal images of the diode laser facet. This approach uses broad LED illumination with an incident radiation flux $\sim$100 times smaller than that previously used in point-based measurements of laser diode facets. Also, a two-dimensional thermal image of the facet allows for spatial averaging of temperature values, providing a more accurate representation of facet temper-

ature compared to point-based methods. Calibration experiments that are performed to measure the thermoreflectance coefficient of coated epitaxial layer samples, account for photoelasticity effects and allow accurate conversion of normalized reflectance changes into temperature rise values. The experimental measurements of temperature rise in the active region are coupled with the predictions of a two-dimensional finite element-based model of heat transport within the diode laser package to derive the degree of optical absorption at the diode laser facet.

The absorption fraction A is defined as,

$$A = 1 - \frac{P_{op}}{P_{op} + P_{surf}}, \tag{4.1}$$

where P_{op} is the measured outcoupled power and P_{surf} is the power of the surface heat source at the facet resulting from optical absorption. Hence P_{surf} can be expressed as,

$$P_{surf} = \frac{A}{1 - A} P_{op}. \tag{4.2}$$

In order to evaluate A, a two-dimensional (2D) finite element-based thermal model of the diode laser was developed. Figure 4.4 shows a schematic of the heat transfer model geometry with marked domains. The model simulates core heat generation, surface re-absorption, and heat transfer through the epitaxial layers and heat sink. In this model, A is used as a fitting parameter to achieve agreement between the experimentally measured facet temperatures and those predicted by the model.

The total waste heat generated in the device (measured experimentally as $(IV - P_{op})$) is divided among three sources of heat in the model: junction heating within the core region, surface heating at the facet, and ohmic heating in the epi layers. Resistive heating in the wire bonds and optical power emitted from the back facet are assumed to be negligible. The ohmic heating component is distributed across the device layers based on their electrical resistivities, while the surface heat source is calculated in terms of A as defined in Eq. 4.2 (P_{op} is known through experimental measurement). The surface heat source intensity distribution is assumed to be a Gaussian with

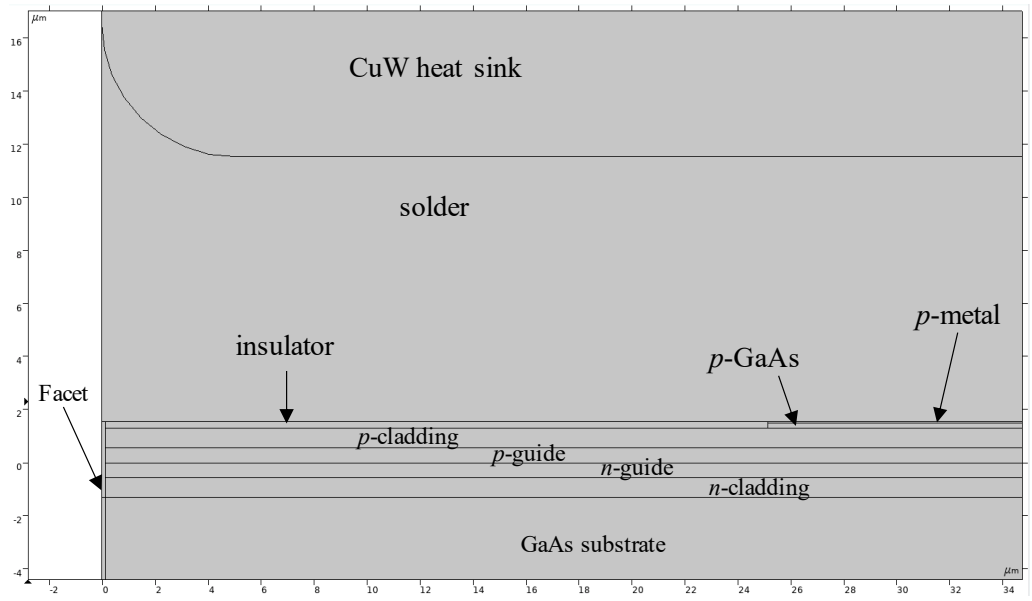

Figure 4.4: A schematic of the heat transport model geometry with marked domains (zoomed in to show the details of the epitaxial layers). The degree of optical absorption is extracted by using it as a fitting parameter to achieve agreement between the experimentally measured facet temperatures and those predicted by the model.

FWHM equal to the optical mode size ($\sim$0.9 μm) that is centered around the quantum well location at the facet. The remaining heat is distributed uniformly in the volume comprising the n and p waveguide layers. In accordance with experimental conditions and the C-mount geometry, the back plane of the heat sink is set to a constant temperature boundary condition (T = 25 °C). Other chip surfaces are given natural convection boundary conditions with typical heat transfer coefficient values. The temperature rise map generated by this model for the $\sim$800 nm diode laser operating at 4 A current is shown in Fig. 4.5.

The model is run for various values of A and the model-predicted above-threshold temperature rise at the facet is calculated for each run. The agreement between experimentally measured facet temperature rise and model-predicted values is shown in Fig. 4.6 for a few values of A. As is evident from Fig. 4.6, $A = 0.0028 \pm 0.0002$ provides the best agreement between the model results and experimental values. The uncertainty bounds for A are calculated as the range of values which provide the best linear fits for the measured ΔT_{QW} values with $\pm\sigma$ uncertainty. At a drive current of 4 A (4.5 W output power), this corresponds to $\sim$12.6 mW of optical power re-absorbed

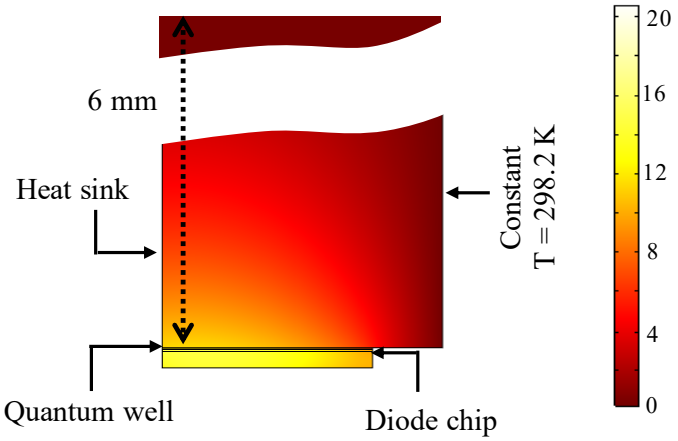

Figure 4.5: Model generated thermal map for the ∼800 nm C-mount device operating at 4 A current.

at the facet. Even though the magnitude of absorbed power is small, the localized nature of surface heating leads to high facet temperatures which can potentially be very damaging to the device. In particular, facets in Al-based devices are more susceptible to defects formed by oxidation which can lead to stronger absorption.

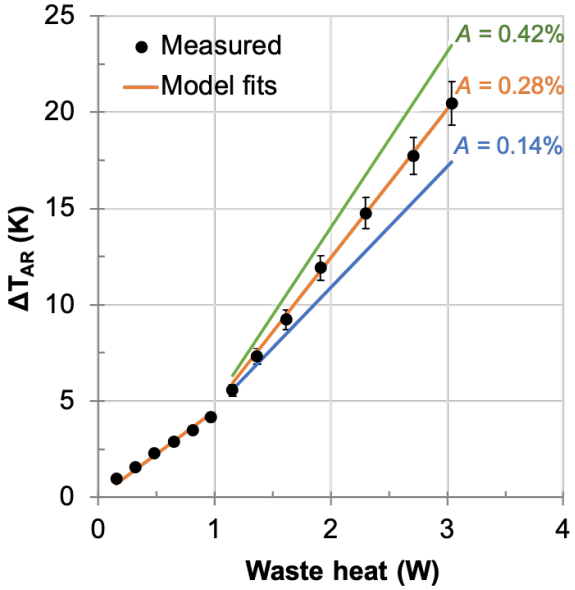

Figure 4.6: Model fits to measured facet temperature data. 0.28% absorption at the facet provides the best agreement between model results and experimental data for the non-passivated diode laser emitting near 800 nm. Inset shows a model-generated map of ΔT in and around the diode chip.

The combination of high-resolution thermal measurement using thermoreflectance microscopy and a detailed thermal model of diode lasers provides a powerful method to estimate the degree of optical absorption at the facet. Notably, the technique described in this work can be implemented for a wide range of diode lasers, irrespective of the presence of facet coatings and passivation layers. The technique can also be used to track device degradation as a function of time, and to quantify and compare the effectiveness of coatings and passivation layers in improving device lifetime. Since high facet temperature is a known precursor to catastrophic optical damage, estimating the degree of facet absorption provides a useful metric to quantify the long-term thermal stability of diode lasers.

4.3 Variation of Facet Optical Absorption with Aging

As mentioned before, the ability to quantify the degree of optical absorption at the facets of diode lasers can be used to track device degradation with aging. In this section we explore the evolution of facet optical absorption over time for two types of diode lasers emitting near 800 nm - with and without passivation layers at the facet, in aging steps of 200 hours.

Facet passivation is the treatment of laser facets to reduce the rate of degradation through one or more of the following methods [89] - removal of surface states caused by dangling bonds and imperfections, removal of existing oxides and filling up states susceptible to oxidation, and creating a diffusion barrier between the facet and the atmosphere. Facet passivation helps reduce the temperature at the facet and improve device lifetime and reliability.

Figure 4.7 depicts the optical power and voltage characterisitics, and thermal resistance values (measured using spectral red-shift approach described in section 3.3) of the passivated and non-passivated device under test. Both devices exhibit similar optical power outputs and thermal resistances. The design of both devices is the same as described in section 3.3

In order to investigate the change in degree of optical absorption at the facet with device age, the following step-wise experimental plan was adopted.

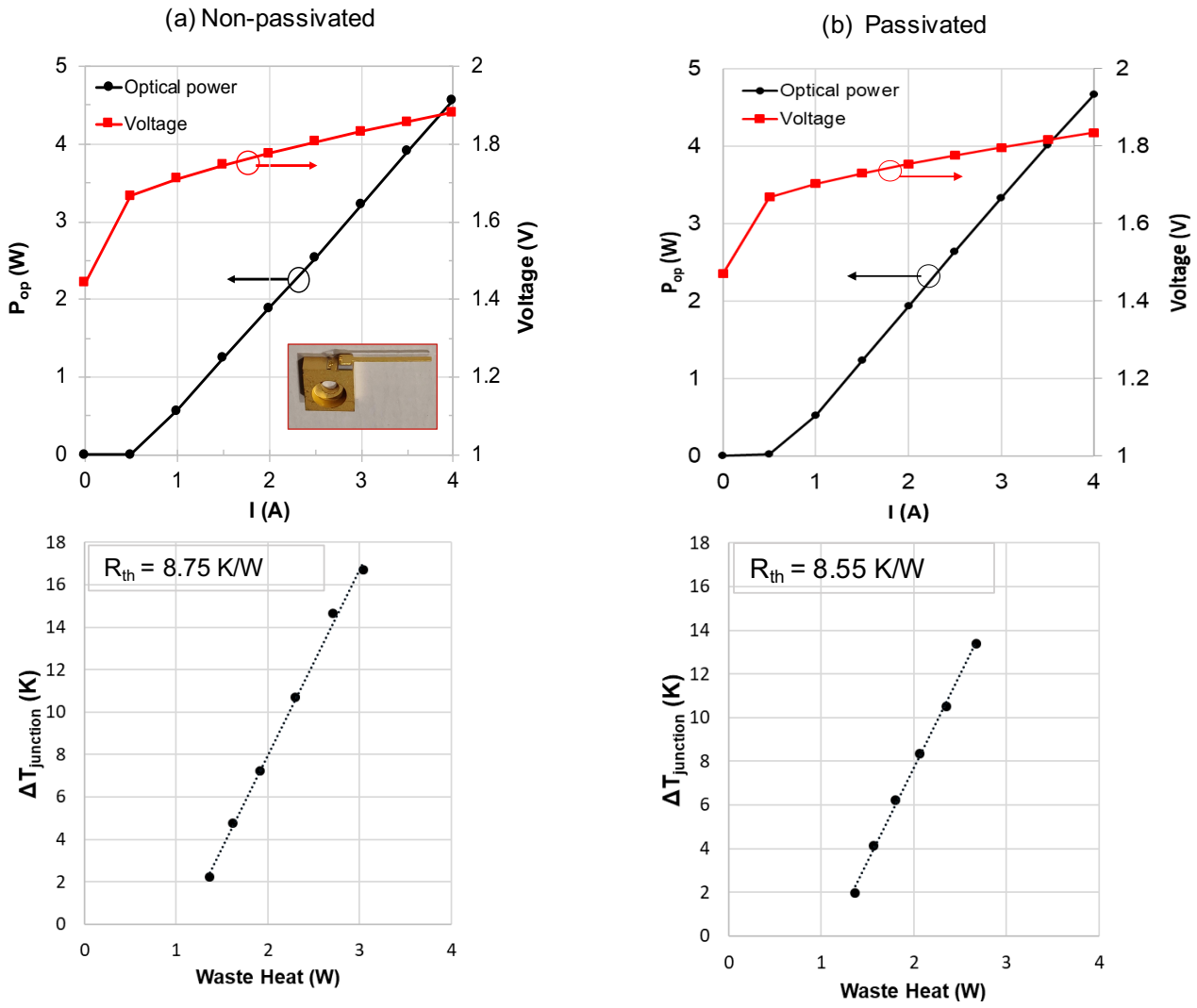

Figure 4.7: Optical power, voltage and thermal resistance measurements for the (a) non-passivated and (b) passivated device emitting around 800 nm. Both devices exhibit similar performance at the rated currents. Inset in (a) shows the C-mount diode laser.

1. Measure the optical power and voltage characteristics, and thermal resistance for the fresh device. Here, fresh device implies the condition in which the device was received from the manufacturer (after the initial burn-in period). We designate this condition as 0 hours of aging.

2. Measure temperature maps of the fresh device using the CCD-thermoreflectance method for operating currents ranging from 0.1 A - 4 A.

3. Calculate the temperature rise near the quantum well (ΔT_{QW}) using the approach mentioned in section 3.4 for all current setpoints, and plot them as a function of waste heat ($IV - P_{op}$).

4. Fit the predictions of the 2D finite element-based heat transport model (described in section 4.2) to the plot from step 2 using facet absorption A as a fitting parameter.

5. Age the diode lasers by operating it in continuous wave mode at the rated current (3.75 A) and a heat sink temperature of 20 °C for 200 hours.

6. Repeat from Step 1.

This experimental plan was followed for two devices of each type (non-passivated and passivated). The non-passivated device was aged up to 400 hours and the passivated device up to 200 hours. The choice of aging step size of 200 hours was based on the prior work on diode laser aging and its effect on device performance. The ΔT_{QW} vs waste heat plot for the non-passivated and passivated devices are depicted in Fig. 4.8 and Fig. 4.9 respectively.

Figures 4.8 and 4.9 bring forth some expected and some interesting trends. The facet temperature values for the two non-passivated devices are similar when both devices are fresh (Fig. 4.8 (a)). This is expected since barring any large irregularities associated with the manufacturing process, the two devices should exhibit similar thermal response. The evolution of facet temperatures with aging for the first non-passivated device (Fig. 4.8 (b)) shows a large increase in above-threshold slope after the first 200 hours of aging. Upon further 200 hours of aging, the above-threshold slope is lowered by a small amount. These results indicate that the facet degradation rate is rapid in

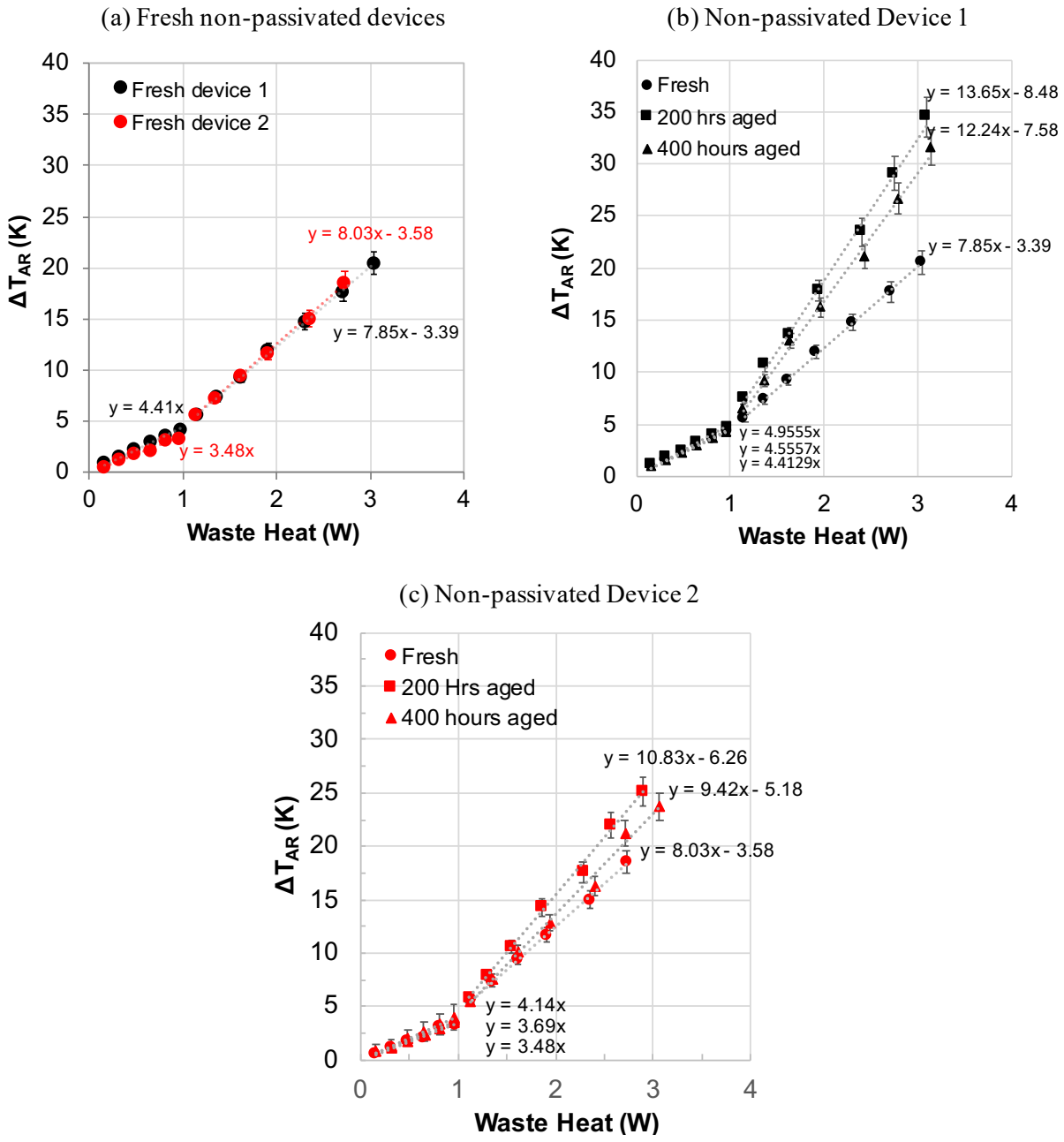

Figure 4.8: Plots of ΔT_{QW} as a function of waste heat for two non-passivated ~800 nm devices (a) at 0 hours for both devices, (b) at 0, 200 and 400 hours of age for the first device, and (c) at 0, 200 and 400 hours of age for the second device.

the first 200 hours of aging, but saturates between 200 and 400 hours of device age. The second non-passivated device (Fig. 4.8 (c)) exhibits similar trends in terms of large increase and small drop in the above threshold slope after 200 and 400 hours of aging, but the increase in slope is not as significant as the first non-passivated device. This indicates that the point defect formation and migration processes in two different devices of the same design may evolve differently.

The facet temperatures of the two passivated devices are also very similar when both devices are fresh, as shown in Fig. 4.9 (a). However, the difference between the below-threshold and above-threshold slopes is much more subtle. This is a consequence of the passivation layers which lower the facet temperatures and mitigate the effects of optical absorption. For both non-passivated devices, the above-threshold slope increases by nearly the same amount after 200 hours of aging. The increase in slope is also less dramatic compared to the non-passivated devices.

Using these plots, and the heat transport model described in section 4.2, the value of facet optical absorption A was derived for all four devices as a function of device age (Fig. 4.10). From Fig. 4.10, we can see that the facet absorption rate more than doubles after 200 hours of aging for all devices under test. After 200 hours of further aging, the non-passivated devices exhibit a $\sim$10% decrease in facet absorption. It is to be noted that the optical power and voltage characteristics of the devices were consistent (within 1%) across the entire aging process for all devices. Additionally, the thermal resistance of each device was also similar across all experiments indicating that there were no overall device-level changes that occurred within these devices. The rise in facet temperatures was a purely a local phenomena up to 400 hours of aging without any significant effect on the laser performance. We also note that the facet absorption rate is ≈ 4 times lower for passivated devices as compared to the non-passivated devices. This provides a direct quantification of the effectiveness of the passivation layers in improving the reliability of these lasers.

Similar measurements and analyses were performed for fresh (0 hours aged) diode lasers emitting near 900 nm (non-passivated and passivated variants) and 1000 nm (non-passivated only) as well. The ΔT_{QW} vs waste heat plots for these devices are depicted in Fig. 4.11. The facet optical

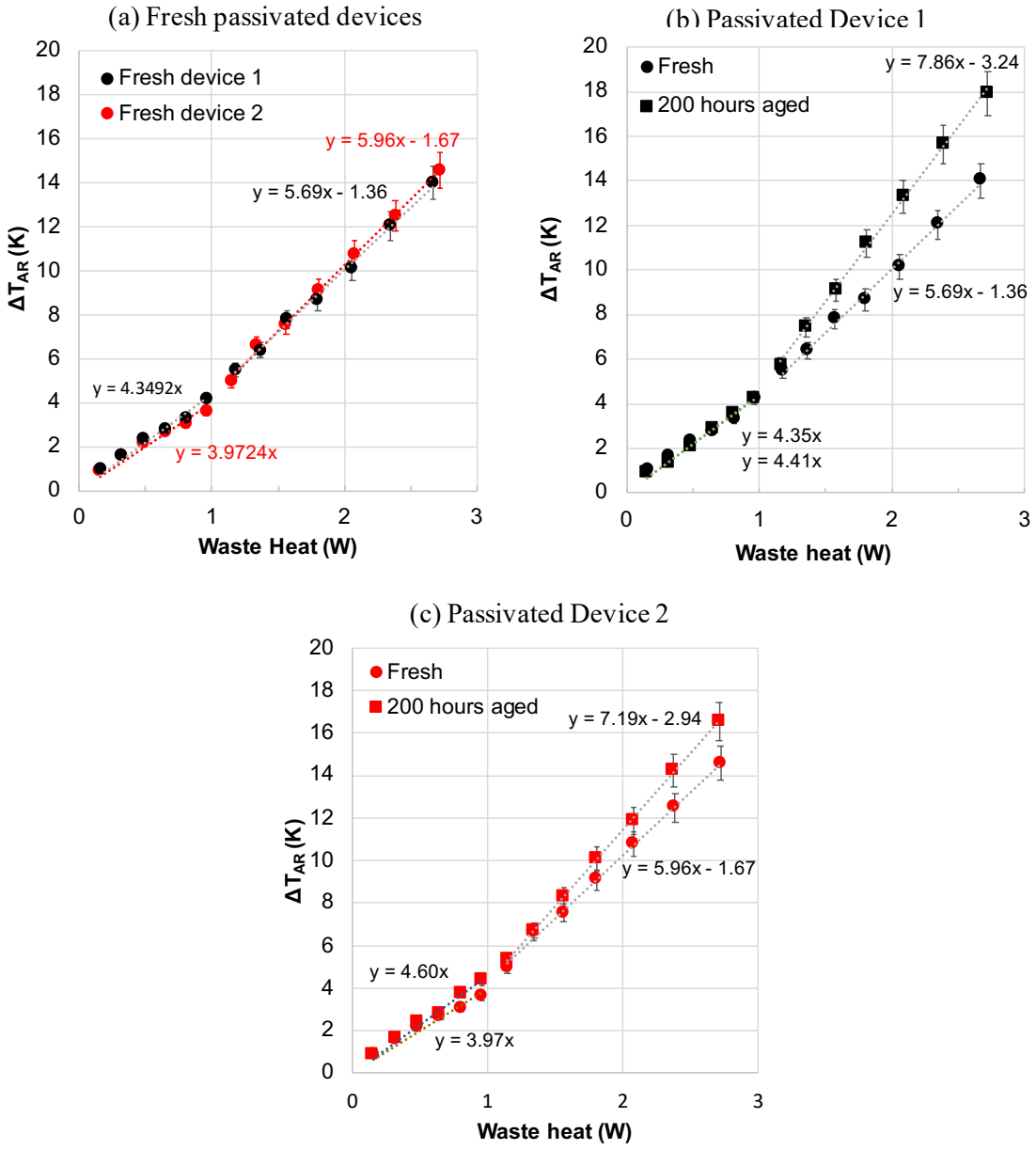

Figure 4.9: Plots of ΔT_{QW} as a function of waste heat for two passivated ~800 nm devices (a) at 0 hours for both devices, (b) at 0 and 200 hours of age for the first device, and (c) at 0 and 200 hours of age for the second device.

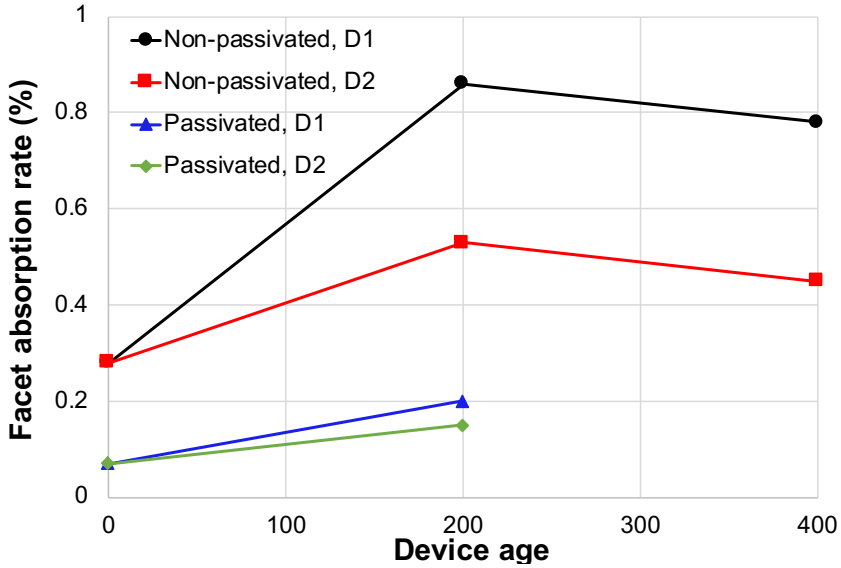

Figure 4.10: Variation of the degree of facet absorption A as a function of device age for two non-passivated and two passivated devices emitting near 800 nm.

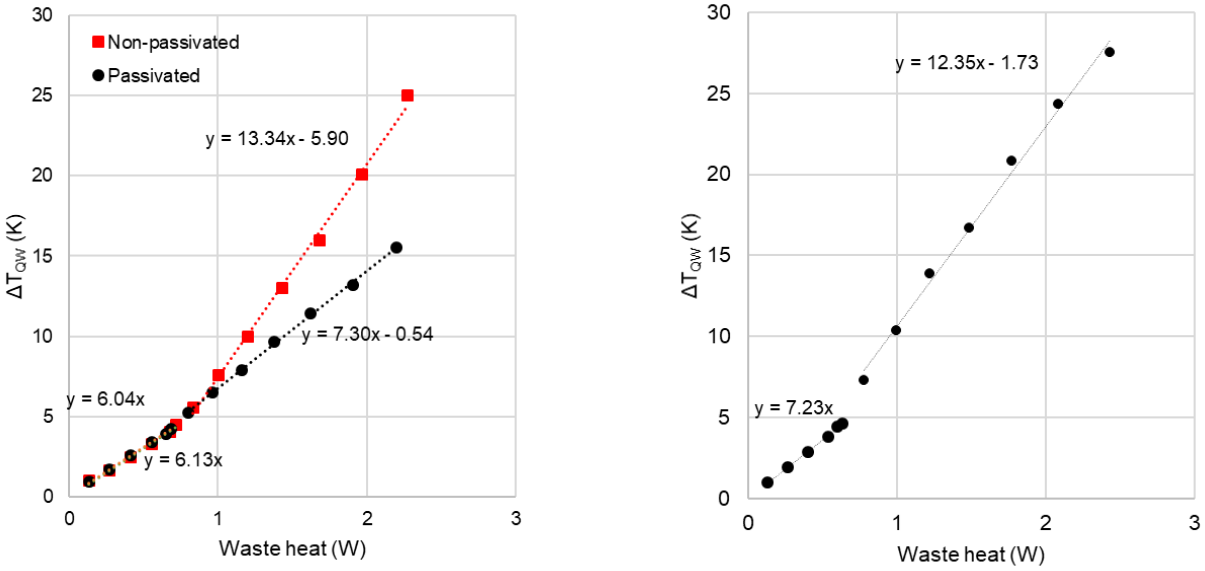

(a) (b)

Figure 4.11: Plots of ΔT_{QW} as a function of waste heat for (a) ∼900 nm fresh non-passivated and passivated devices (b) a ∼1000 nm fresh non-passivated device.

absorption for the non-passivated devices emitting near 900 nm and 1000 nm were determined to be 0.68% and 0.81% respectively, whereas the passivated variant of the 900 nm emitter exhibited a facet absorption of 0.23%. Clearly, the absorption rate is $\sim$2.5-3 times higher for longer wavelength devices, compared to 800 nm emitters. This could be a consequence of the wavelength-dependent absorption characteristics of the constituent materials, in addition to a difference in the defect density at the facet due to different strain and growth conditions.

Overall, these results indicate that facet degradation is rapid in the first 200 hours of aging and saturates thereafter. In order to explore this implication in more detail, it is necessary to carry out thermal characterization experiments during the first few hundred hours of device operation at a smaller aging step. Such analysis will help in understanding the dynamics of facet degradation and the associated time scales. The details of this study are provided in the next section.

CHAPTER 5

High Resolution Thermal Profiling of Diode Laser Active Regions

In the previous section, the results from aging studies of diode lasers were presented. Based on these results, we conclude that the initial 200 hours of operation are crucial from the perspective of diode laser degradation. The small decrease in the degree of optical absorption with further aging of 200 hours was surprising and indicated a saturation behavior.

So far, we have quantified the average temperature rise near the quantum well at the facets of high power diode lasers by averaging peak temperature values within the active region. However, this metric does not capture details of thermal response such as the spatial variation of temperature profile, temperature gradient variations and local hot spots within the active region. In most cases of diode laser failure at the facet, damage occurs over a small area of the emission region as opposed to the entire emission strip. Hence, it is important to capture these local effects which become more important than an average overall increase of facet temperatures as the diode laser ages. Moreover, based on the conclusions from the previous study that significant temperature rise occurs over the first few hundred hours of laser operation, it becomes imperative to probe this timescale at a higher temporal resolution to capture the evolution of degradation in greater detail. Using these ideas, an aging study was designed to capture fine details of thermal response during the initial period of device operation.

The device under test for this study is a $\sim$800 nm, non-passivated emitter of the same design as described in section 3.3. The optical power and voltage as a function of injection current, and the junction temperature rise of the device as a function of waste heat are depicted in Fig. 5.1.

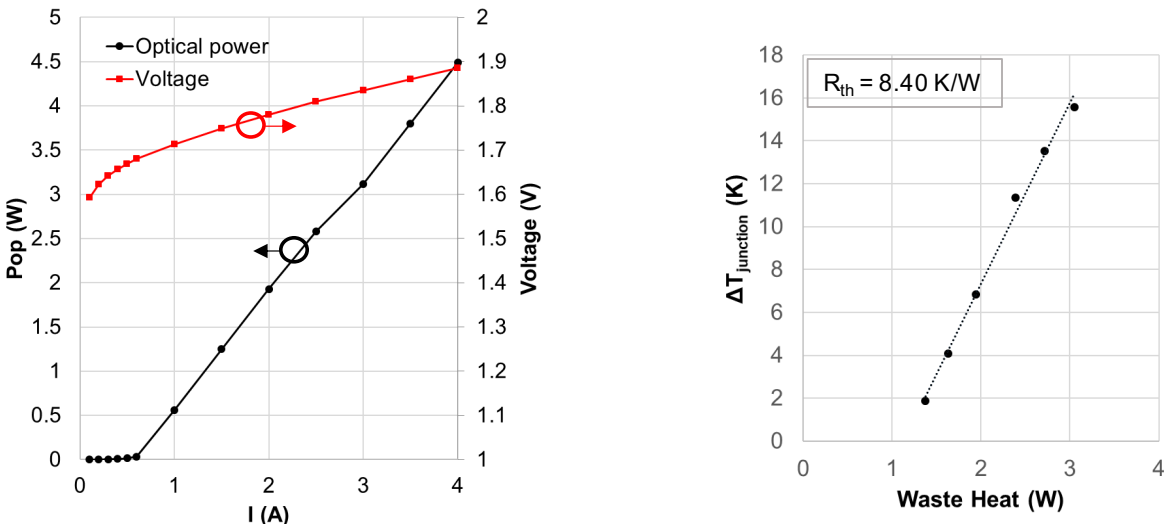

Figure 5.1: Optical power and voltage as a function of operating current, and thermal resistance for the device under test.

This device was aged up to 198 hours in aging steps of 12 hours (there was one aging step which was 18 hours long. This results in the total device age to be 198 hours instead of 192 hours after 16 steps.). The device was tested after each aging step using the same experimental protocol as described in section 4.3. As described before, the region over which the device emits is $\sim$ 180 μm $\times$ 2 μm in size. In order to capture the entire emission region in one image, the experiments were conducted at a magnification of 50X which provides a $\sim$ 182.2 μm $\times$ 135.4 μm -sized field of view.

The thermal maps of the active region at the facet at a drive current of 4 A measured after each aging step are depicted in Fig. 5.2. The fresh device (0 hours) exhibits a maximum temperature rise of only about 20 K at 4 A drive current. Regions with a characteristic size of $\sim$ 5-10 μm can be observed which are hotter than neighboring regions. As the device ages, there is a general increase in the temperatures across the entire emission region, while the hot areas maintain their positions. After 60 hours of aging, two small hot regions are identified (Fig 5.3 (a)) in the right half of the map at the substrate/epi-layer interface. Another similar hot spot arises after 114 hours of aging. These hot spots are consistently observed in all subsequent maps and their surroundings are not

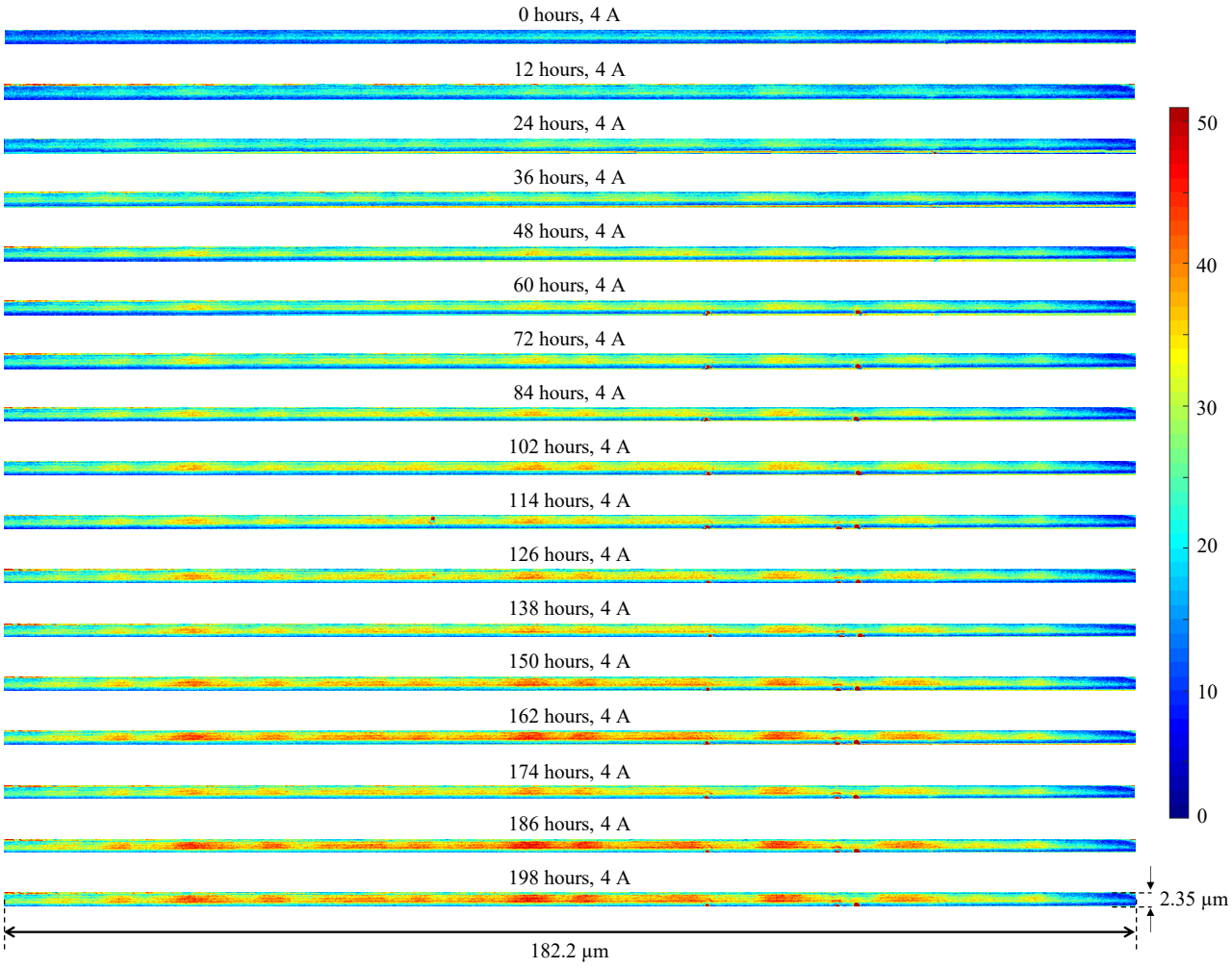

Figure 5.2: Thermal maps of the active region at the facet of a ∼800 nm diode laser operating at 4 A current, at various steps of aging.

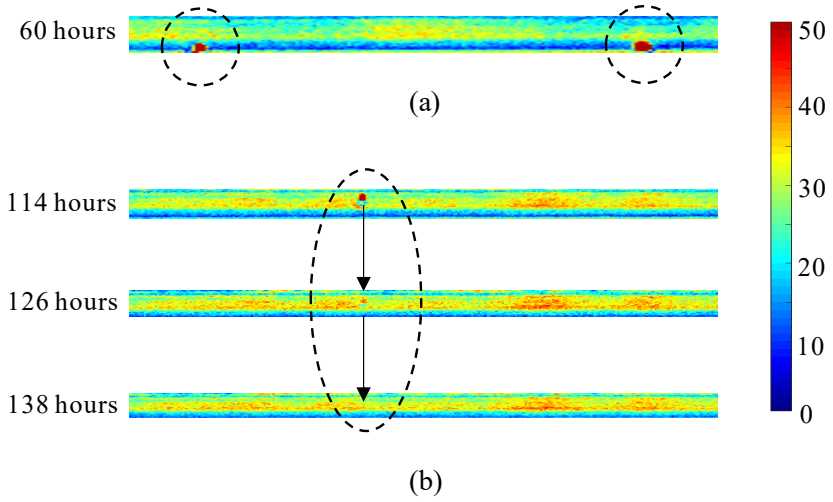

Figure 5.3: (a) Hot spots appear at the substrate/epi-layer interface after 60 hours of aging. The regions around these hot spots are not thermally perturbed which leads to the conclusion that these are debris on the diode laser facet. (b) A hot spot appears in the middle of the epi-layers which grows fainter and eventually disappears with aging. This could be a case of point defect generation and migration away from the facet.

nearly as hot. Hence these spots were concluded to be debris on the facet and the associated hot spot in the thermal map is merely an artifact.

Another localized hot spot is observed after 114 hours of aging in the left half of the active region (Fig. 5.3 (b)). This hot spot is not located at the interfaces, but is closer to the center of the epi-layers. After the next aging step, a hot spot can still be observed at the same location, but is much fainter. The hot spot disappears completely after 138 hours of aging. This could be a point defect which was created close to the facet and migrated inwards into the cavity as the device aged, although further investigation is necessary to confirm this hypothesis.

The device optical power output over the entire aging process was largely unchanged. Figure 5.4 depicts the optical power output of the device at 4 A current as a function of device age. A small downward trend can be observed with a total power drop of 1.4% (0.063 W) over 198 hours alongside an increase in waste heat of similar magnitude.

In order to make quantitative comparisons between the thermal maps across different aging steps, temperature profiles along the slow axis were calculated for each thermal map through the

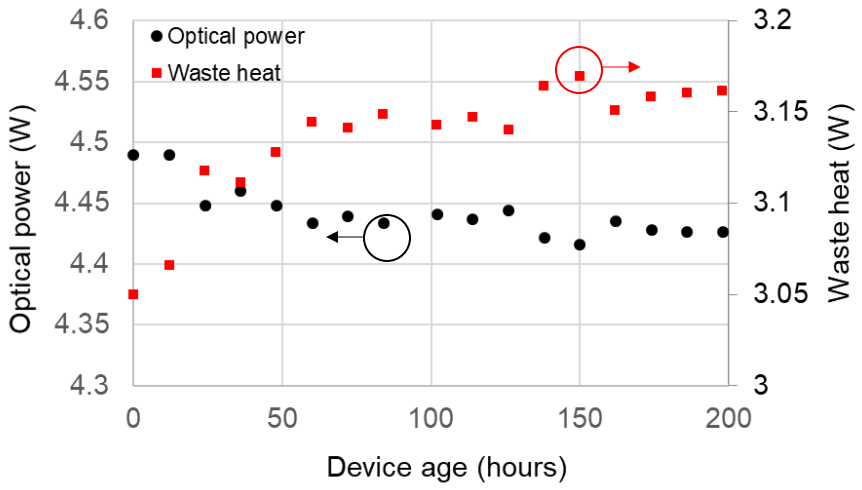

Figure 5.4: Optical power output (P_{op}) and waste heat ($IV - P_{op}$) as a function of device age for 4 A drive current. We can see that there is a gradual decrease in the power output and a simultaneous increase in the waste heat as the device ages.

following process. First, a peak temperature is identified along every vertical slice of the thermal map. An average temperature value corresponding to each vertical slice is calculated by averaging temperatures within 0.85 μm (FWHM of the optical mode) around the location of the peak temperature. Each vertical slice corresponds to a slow axis location in the range 0 - 182.2 μm, hence the temperature profile along the slow axis direction can plotted from this information. The averaging process in the fast axis direction accounts for heat spreading and is a better representation of the average facet temperature at a given location compared to only the peak temperature. The temperature profiles at 4 A current for all aging steps is depicted in Fig. 5.5. These profiles have been denoised through low-pass filtering which gets rid of high frequency variations in the profile that are not physical.

From Fig. 5.5 we can clearly see the development of local temperature spikes at particular locations along the slow axis with aging, in particular around 30 μm, 45 μm, 85 μm and 125 μm (The sharp spike at nearly 140 μm corresponds to the debris artifact). There is an overall parabolic curve to the temperature profiles, which is expected due to thermal diffusion in the slow axis. However, the fine structure observed in the temperature profiles spatially is unprecedented. Some large peaks, such as the one around 85 μm corresponds to a temperature gradient of $\sim$1.3 K/μm.

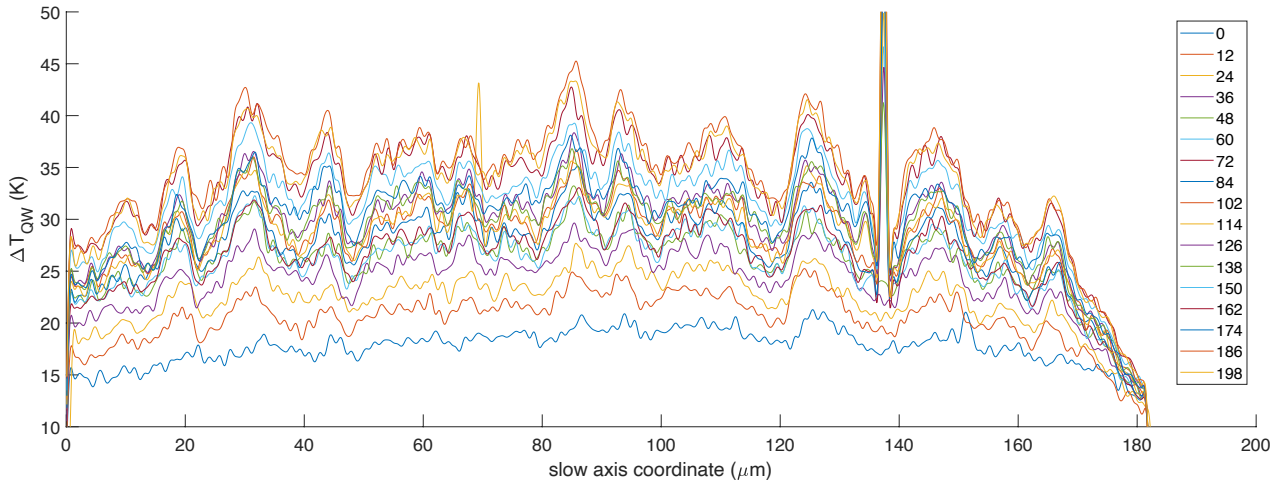

Figure 5.5: Temperature profiles within the epitaxial layers at the facet along the slow axis direction as a function of device age at 4 A current. The value at each slow axis location corresponds to an average over ∼0.8 μm in the fast axis. The mean and standard deviation (non-uniformity) of facet temperature shows a general increasing trend with age. The local spikes in the temperature profile have a characteristic width of a few microns and are consistent in their positions as the device ages.

Such steep thermal gradients can result in large thermally-induced strains at the facet which has significant implications for defect formation rate and the lifetime and reliability of these devices. Moreover, such temperature mapping allows identification of the parts of the device that are most susceptible to undergo catastrophic damage. The location of the peaks are very consistent across the various thermoreflectance experiments that were conducted over the duration of a few months, which indicates that these are not random fluctuations in the temperature profiles.

Figure 5.6 depicts the variation in temperature profile along the slow axis for operating currents ranging from 0.1 A - 4 A after 198 hours of aging (The sharp spike at nearly 140 μm corresponds to the debris artifact). Some local temperature spikes, such as the ones at around 125 μm and 115 μm, show a consistent increase in their values as current increases while also maintaining their positions. However, several other peaks such as the one at around 85 μm show a more complicated trend. We can see that a prominent temperature spike appears around this location at 2 A drive current, which becomes much less pronounced for 2.5, 3 and 3.5 A, only to strengthen again at 4 A. Similarly the peak at around 170 μm for 4 A current is nearly non-existent at all lower currents

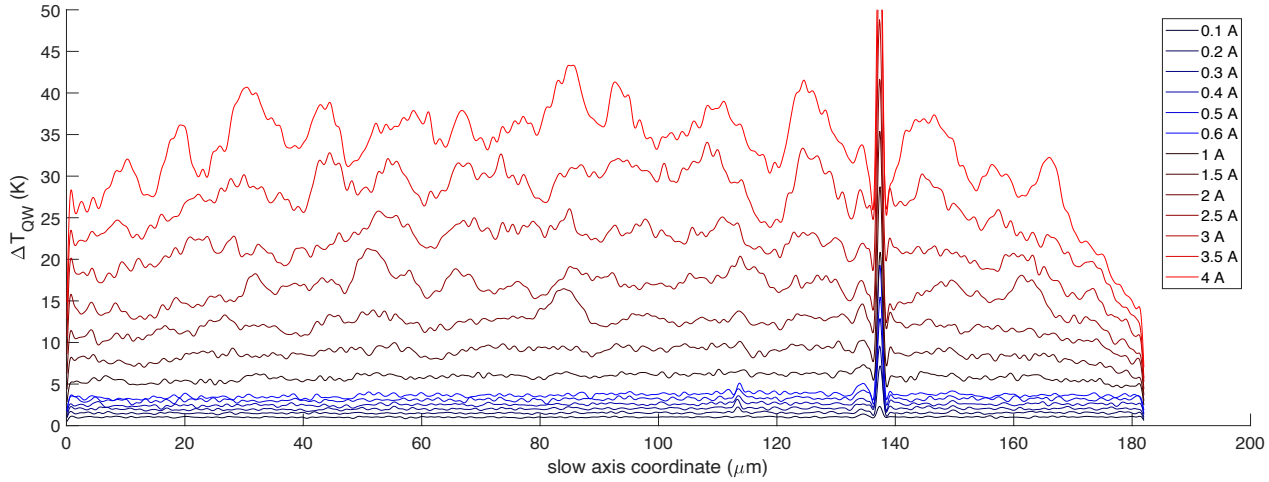

Figure 5.6: Temperature profiles within the epitaxial layers at the facet along the slow axis direction as a function of the operating current after 198 hours of aging. Some distinctive peaks can be observed which get consistently bigger with increasing current. However, there are also local spikes in temperature which appear at certain currents and disappear upon increasing it.

(other than a slightly shifted temperature peak at 2.5 A). Such trends can be explained by a closer examination of the interplay between temperature, optical intensity and defect density distribution along the facet.

As discussed in chapter 1, temperature rise at the facet for large injection currents is primarily caused by non-radiative recombination of carriers generated by optical absorption. Defects near the facet serve as non-radiative recombination centers. Hence, the two factors which affect facet temperatures are the concentration of carriers available for recombination and the density of defect states at the facet that can aid in this process. Diode lasers do not produce uniform intensity emission across the entire active region. This is due to non-linear effects in the laser medium such as non-linear heating and carrier distribution which can lead to inhomogenous refractive index profiles, thus resulting in a non-uniform optical intensity distribution (also called filamentation). The defect density distribution is also non-uniform across the facet and depends on several factors such as threading dislocations, stacking faults and crystal inhomogeneties introduced during epitaxial growth. Hence, the temperature profile at the facet is expected to be a convolution of the optical intensity and defect density distributions along the facet. In turn, temperature affects the local

optical intensity (by modifying the refractive index) and also affects the rate at which defects are created and accumulated.

It is possible that a varying optical intensity profile at the facet as a function of operating current modifies the degree of optical absorption that occurs at a particular location on the facet. If so, a direct correlation can be expected to exist between the the optical intensity profile and the temperature profile at a given current. To investigate this further, the thermoreflectance measurement setup was modified to measure optical intensity profiles. This was achieved by removing the OD 6 band-pass filter in front of the CCD camera and taking images of the operating diode laser at very low exposures such that the sensor is below saturation. Only $\sim$1% of the emission reaches the CCD sensor due to rejection by the dichroic mirror to prevent damage to the sensor. The captured image is averaged in the fast axis direction and the resultant profile is normalized. The normalized optical profiles calculated in this manner for above-threshold currents (1 A - 4 A) are plotted alongside the temperature profiles for the same set of currents, after 36 hours and 48 hours of aging in Fig. 5.7. It is noted that the all optical intensity profiles are normalized to lie between 0 and 1 and have been artificially shifted in the vertical direction for plotting purposes (top-most curve for 4 A and bottom-most for 1 A).

From Fig. 5.7 we can see that the optical intensity profiles are almost identical between 36 hours and 48 hours of aging. There are clear direct correlations between spikes in the optical intensity and temperature at the most prominent temperature peaks such as around 30 μm, 85 μm, 130 μm and 150 μm. However, there are also several locations where we see spikes in the temperature profiles but no corresponding local spike in the optical profile such as around 110 μm. These observations indicate that the local photon flux is an important factor in determining the temperature, but large defect densities in some regions may cause elevated temperatures in a location even with a moderate degree of optical output.

In order to confirm the reproducibility of experimental results, the above-threshold temperature measurements were repeated twice after 36 hours of aging. The agreement of the results is depicted in Fig. 5.8. Based on these results, it can be safely concluded that these temperature spikes are not

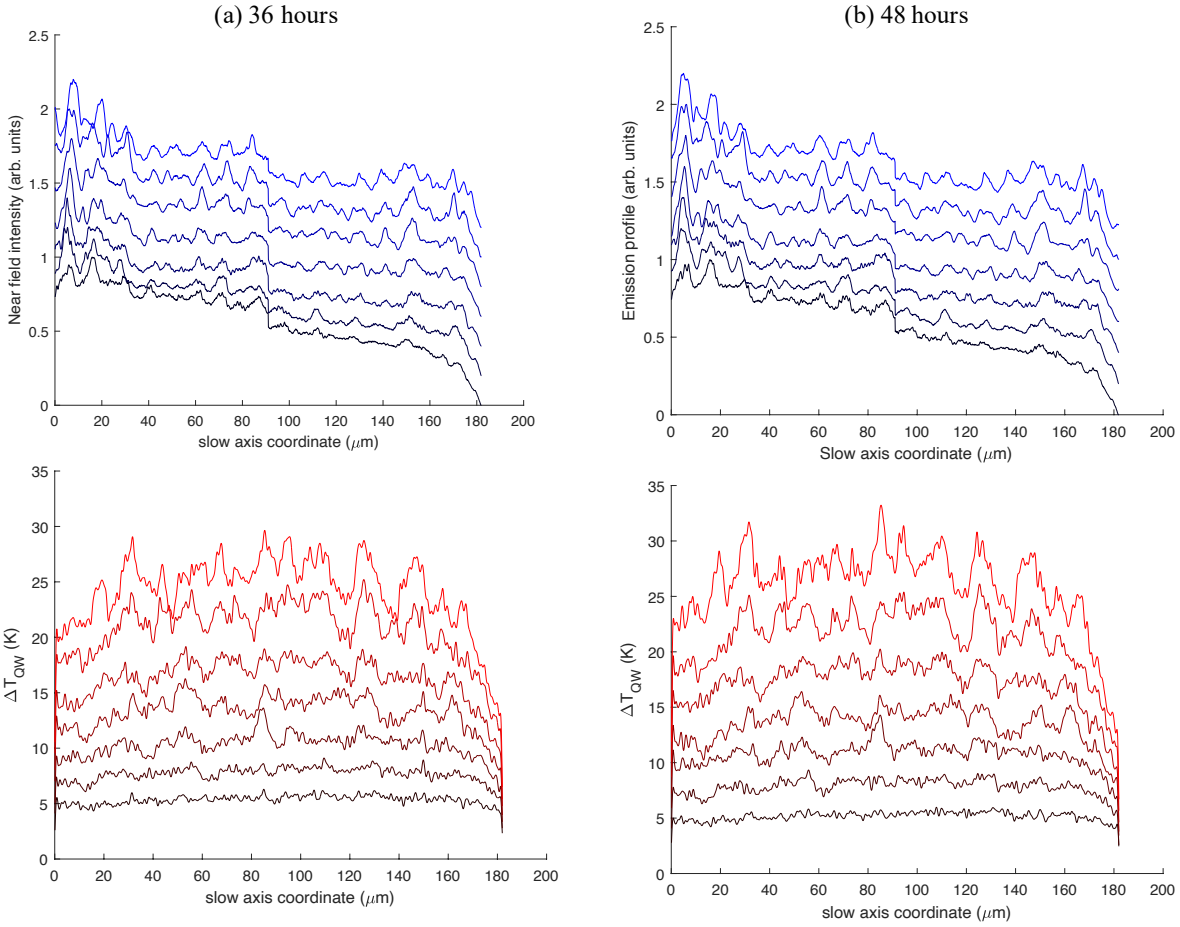

Figure 5.7: Optical intensity profiles and temperature profiles along the slow axis after (a) 36 hours and (b) 48 hours of aging. The largest temperature peaks correlate well with local spikes in the optical intensity profiles. However, there are peaks in the temperature profile not associated with any optical peaks as well.

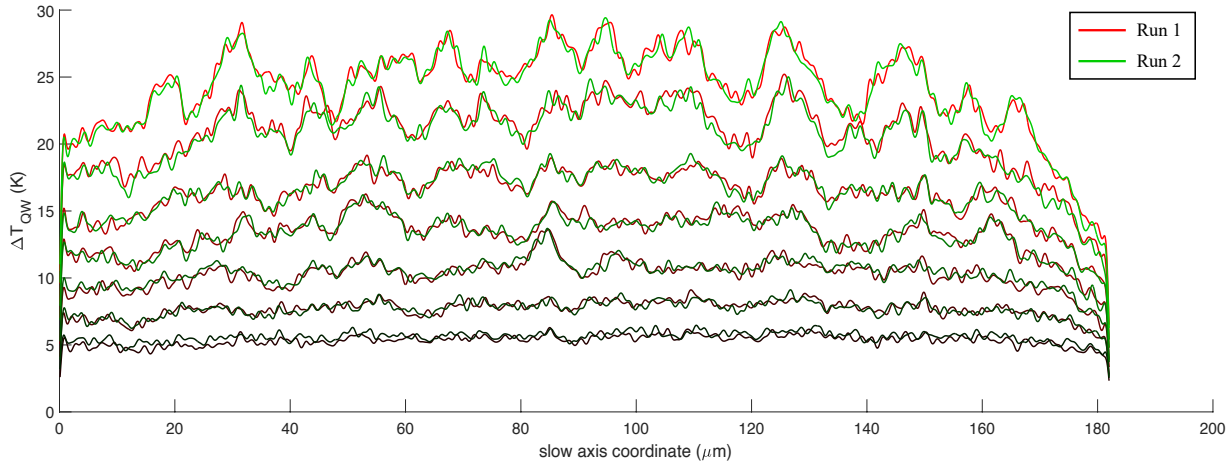

Figure 5.8: Temperature profiles along the slow axis within the epitaxial layers for above-threshold currents for two separate runs at the same aging step (36 hours). The good agreement between results from two separate runs indicates that the non-uniformities in the temperature profiles are not random measurement artifacts, but a result of physical processes.

random artifacts.

In order to investigate the evolution of laser degradation with aging, we utilize the approach outlined in section 4.3. We begin by plotting ΔT_{QW} as a function of the device waste heat for all aging steps (Figure 5.9 (a)). The ΔT_{QW} is calculated by averaging the active region temperature profiles over the center half ($\sim$ 90 μm) of the emission region. This is the most representative temperature rise metric since it takes into account the temperatures of the most vulnerable regions of the diode laser and the heat spreading in the fast axis. As before, a change in slope is observed when the laser transitions from below-threshold to above-threshold operation. More importantly, we note that the above-threshold slopes do not increase monotonically with device age. This trend becomes clearer in Fig. 5.9 (b) where we see an overall saturation behavior in the values of above-threshold slope as a function of device age, albeit with some local fluctuations. These fluctuations appear as a negligible change or a drop in the above-threshold slope at some consecutive aging steps. It is not clear what causes these irregularities compared to the general increasing trend. It is worth noting that this behavior was also observed in the results described in section 4.3 where a drop was observed in the above-threshold slope after the device was aged from 200 to 400 hours.

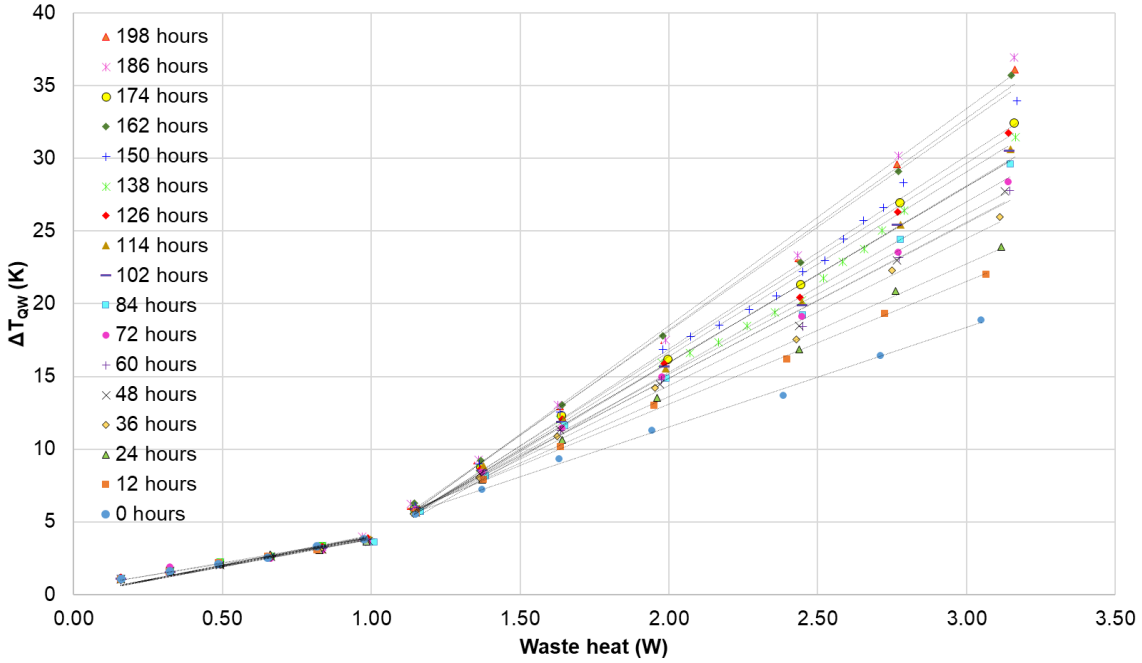

(a)

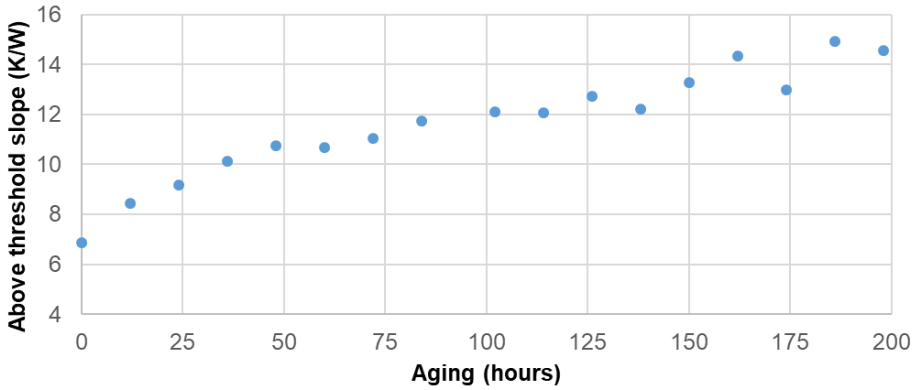

(b)

Figure 5.9: (a) Temperature rise near the quantum well at the facet plotted against waste heat for all operating currents and all aging steps. (b) Above-threshold slopes as a function of device age. The above-threshold slopes show a general increasing trend with age, but there exist consecutive aging steps where the slope decreases.

Another important metric that could be closely related with diode laser degradation is the standard deviation of ΔT_{QW} within the active region at the facet ($\sigma_{\Delta T_{QW}}$). An increase in $\sigma_{\Delta T_{QW}}$ implies growing temperature gradients at the facet which can affect laser reliability even as the mean facet temperatures does not rise appreciably. Figure 5.10 (a) and (b) plot the variation of $\sigma_{\Delta T_{QW}}$ and $\frac{\sigma_{\Delta T_{QW}}}{\Delta T_{QW}}$ (coefficient of variation) as a function of above-threshold operating currents and device age.

From Fig. 5.10 (a), we can see that at any given aging step, the standard deviation of temperature values increases from 1 A - 4 A. However, a kink is observed at 3 A for all aging steps. The standard deviation values exhibit a saturation behavior up until 3 A, however, increasing the current beyond 3 A leads to a rapid increase in the temperature gradients within the active region. Fig. 5.10 (b) depicts a similar trend, wherein the standard deviation relative to the mean facet temperature rise exhibits a local minimum (global minimum for some aging steps) at 3 A. In other words, the facet temperatures are most homogeneous at 3 A. In order to investigate the device behavior around 3 A, the thermoreflectance experiments were conducted in smaller steps of 0.1 A between 2.5 A and 3.5 A after 138 and 150 hours of aging. We found that the trends in standard deviation and coefficient of variation of temperature with increasing current are not monotonic. However, the fluctuations are repeatable and not random artifacts. These results indicate that the thermal behavior of the facet is very responsive to changes in the operating current, probably due to the changing local current distributions and optical intensities. We also note that the ΔT_{QW} values also exhibit a significant kink at around 3 A ($\sim$ 2.4 W waste heat) where the behavior deviates from a linear increase in facet temperature with waste heat for all aging steps (Fig. 5.9). Moreover, the optical power output vs current plot for the device (Fig. 5.1 (a)) also exhibits a small kink at 3 A current. Such behavior is likely the result of filamentation which is caused by changes to the refractive index profile within the laser medium due to non-linear effects and is dependent on the injection current distribution, as described earlier. The kink in the optical power output is minimal, nonetheless it significantly affects the temperatures at the facet. The relationship behind a small kink in optical power and the homogeneity of the facet temperature profile is not clear.

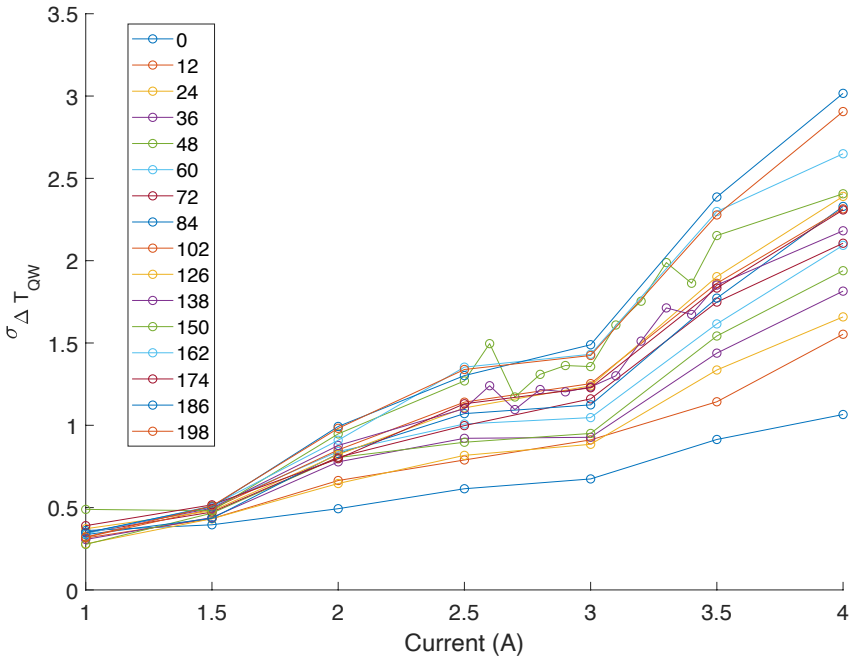

(a)

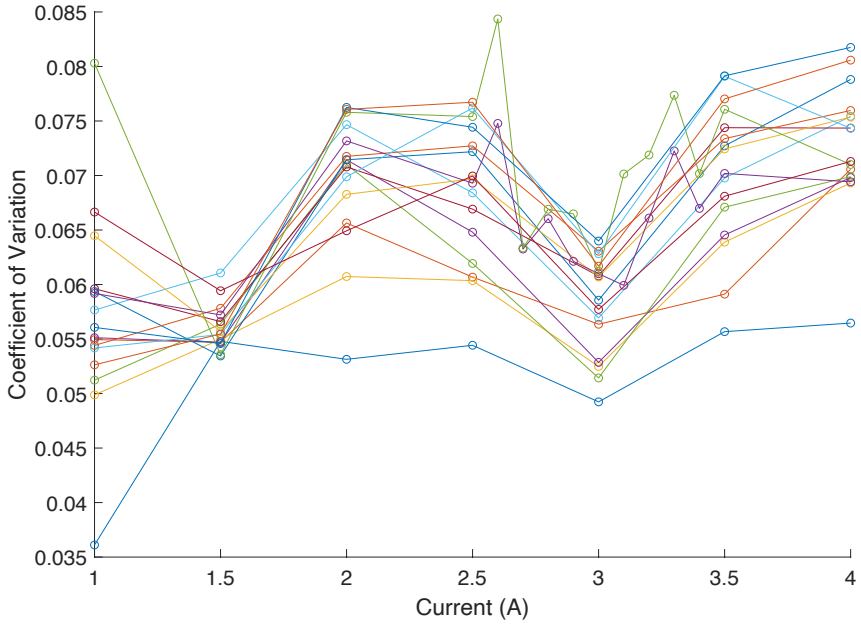

(b)

Figure 5.10: (a) Standard deviation and (b) coefficient of variation (ratio of standard deviation and mean) of temperature profiles calculated over the center half of the emission region, as a function of operating current and device age. The standard deviation shows a general increasing trend with age and current. A kink is observed in the standard deviation and coefficient of variation at 3 A current for all aging steps. A similar kink is also observed in the mean temperature rise at the facet as a function of waste heat in the device.

Based on these analyses, we conclude that facet temperatures in high power diode lasers exhibit very fine structure with large thermal gradients and distinctly hot regions. The facet temperatures generally increase with device age, but this increase may not be monotonic. The temperature distribution at the facet is found to correlate to a small degree with the optical intensity distribution, and variations in operating current significantly impact the thermal profile at the facet of the device.

CHAPTER 6

Summary and Future Work

6.1 Summary

Semiconductor lasers are the most efficient man-made narrow-band light sources with state-of-the-art devices exhibiting > 70 % efficiency in converting electrical energy to light. As power densities scale up, failures caused by heating become an ever important issue. In this work, we have developed thermal characterization methods based on CCD camera-based thermoreflectance imaging which allow high resolution, two-dimensional thermal mapping of high power diode lasers under operation. We have used this method to characterize diode laser degradation caused by absorption of light near the quantum well at the outcoupling facet. We have explored two ways in which light absorption can occur at the facets of diode lasers - through back-reflection of laser emission, and through absorption of outgoing emission incident from within the cavity.

By examining the thermal response of GaAs-based high power diode lasers subjected to back-irradiance, we concluded that heating caused by absorption and localization of back-irradiance light near the quantum well leads to large temperature rise at the facet which is detrimental to the device lifetime and reliability. Critical locations were identified on the diode laser facet, within ~ 1.5 μm of the quantum well, such that when the back-irradiance is positioned at these locations, the active region temperatures rise significantly ($\sim$3 times temperature increase compared to regular operation for 7.5% optical feedback power and ~ 4 times for 15% optical feedback power at rated current). Moreover, it was found that TM-polarized back-irradiance can get distributed along the metal edge when positioned in the solder region of the diode laser, while TE

polarized back-irradiance gets localized at the p-metal corner, leading to higher quantum well temperatures. Through thermoreflectance-based thermal mapping of diode lasers under controlled back-irradiance conditions, we identified the effect of key factors such as wavelength and polarization of laser emission, and the position of back-irradiance on the susceptibility of a diode laser to back-irradiance induced failures.

We also developed techniques to track and analyze device degradation over time in high power diode lasers through thermal mapping of their facets for a range of operating currents above and below the threshold current. The presence of an additional optical contribution to facet temperature rise was indicated by a change in the rate of increase of facet temperature per unit waste heat as the device transitioned from below-threshold to above-threshold operation. These measurements were combined with the model predictions of a two-dimensional, finite element-based heat transport model of the chip to develop a framework for quantification of facet absorption. The framework was utilized to study the evolution of facet absorption with aging, and to evaluate the effectivenss of passivation treatments in reducing the temperatures at the facet. It was found that facet temperatures increase rapidly during the first few hundred hours of aging and then exhibit a possible saturation with further aging. The passivation treatment on the device under test was found to reduce facet temperature rise by a factor of four. Through this analysis, we developed a technique to track device degradation with aging and compare the effectiveness of passivation technologies.

Using the CCD camera-based thermoreflectance technique, we also probed the temperature distribution within the active region at the facet and its evolution with aging at high spatial resolution. It was found that temperature distribution along the slow axis of these devices is highly non-uniform with large thermal gradients of up to 1.3 K/μm and temperature peaks with characteristic widths of $\sim$ 5 μm. The position and relative strength of temperature peaks were found to be strongly dependent on the injection current and also exhibited correlations with the optical intensity distributions. Moreover, the positions of high temperature regions for a fixed injection current were consistent across all steps of device aging while the mean and standard deviation of temperature profile increased by two and three times respectively over a total aging period of 200

hours. Such observations allow identification of the most vulnerable regions of the device and open up pathways for developing strategies to mitigate device failure through thermal monitoring.

6.2 Future Work

This section discusses several directions in which the current work can be extended.

6.2.1 CCD-based thermoreflectance imaging to monitor for precursors of catastrophic optical damage

As described in Chapter 1, catastrophic optical damage is the result of a thermal runaway process composed of a sequence of events. The onset of COD is quite sudden and it has been observed to happen without any prior signature. Due to the complicated nature and fast dynamics of this process, probing the early stages of COD is an active area of research. While dark spots and dark-line-defects are observed within the epitaxial layers after COD, we observed what seemed to be a precursor of these features during one of our thermoreflectance experiments.

In particular, this precursor was observed during thermoreflectance imaging of a $\sim$ 800 nm diode laser operating at 2 A current, subjected to back-irradiance with $R_{eff} = 24.3\%$ (24.3% of the optical power output ($\approx$ 0.466 W) reflected back onto the diode laser facet). The back-irradiance spot was placed at 27 different locations on the facet ranging from x = -10 μm (in the solder) to x = 40 μm (in the substrate) where x = 0 μm corresponds to the quantum well. The experiment at each BI location takes nearly two minutes with the laser operating at 4 Hz frequency with a duty cycle of 50%. Hence the BI spot dwell time for each experiment (location) was nearly 1 minute.

When the BI spot was positioned at x = -1 μm (in the solder), a small bright spot appeared within the epitaxial layers (top left panel of Fig. 6.1). No such feature was observed at the same location in the optical microscope image. Then, as the BI spot is swept closer to the quantum well in increments of 1 μm, the bright spot appears to grow larger in the thermoreflectance image,

without appearing in the microscope image. Finally, when the BI spot is positioned 2 μm away from the quantum well in the substrate, a line defect is observed in the microscope image which shows up as a bright spot on the thermoreflectance image as well.

The appearance of a hotspot in the thermoreflectance image before it shows up in the microscope image could be caused due to an actual temperature increase caused by heat diffusing from a defect within the cavity close to the facet. It could also be caused by a change in the thermoreflectance coefficient of the material at that location due to phase transformations and/or structural changes. The ability to detect precursors of COD before actual failure can be useful from the perspective of analyzing the device at the location of the hotspot to understand the changes in the device which eventually lead to COD. It could also help in developing strategies to reverse the damage and extend device lifetime.

An experimental setup to carry out such analysis was put together and used to analyze two diode laser devices by driving them to failure. The experiments were set up such that a diode laser would operate at 4 Hz frequency and 50% duty cycle at incrementally higher operating currents, while recording thermal images and optical intensity profiles, up until failure. The laser power was monitored by placing a power meter along the path along which the dichroic mirror reflects the laser emission. The system was programmed to stop the experiments when a small but significant power drop is observed. The two devices were driven to failure, however, no precursors were observed before COD. Hot spots were observed within the epitaxial layers, but they were visible in the optical images as dark spots as well.

In order to improve upon this experimental protocol, the device can be operated at a large, fixed operating current (for example, nearly 1.5$\times$ the rated current) for an extended period of time, instead of incrementing the current in steps until failure. This will emulate an accelerated device lifetime more closely than the previously described protocol. Moreover, the experiment can be programmed to stop after a large hot spot is observed in the active region, with or without a power drop. A video of the device can also be rcorded in real time (using the same camera as CCD-TR setup) to keep track of features as they appear and move within the epitaxial layers. Once a

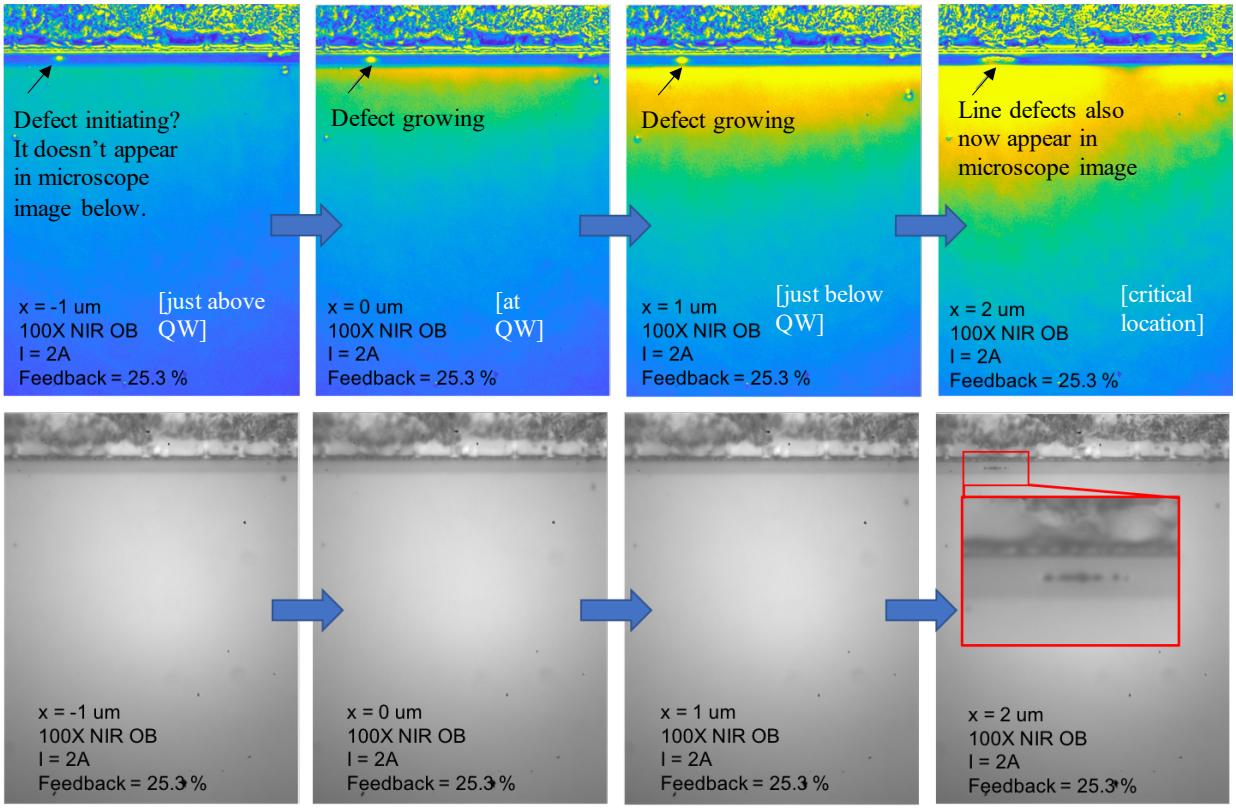

Figure 6.1: The top panels depict the thermoreflectance images where a hot spot is observed within the epi-layers while the microscope images (bottom panels) do not register any such feature at the facet until dark line defects appear in the microscope image in the last panel. This observation could be an example of a precursor to COD which manifests as a thermal perturbation, but does not appear to form at the facet itself.

precursor to COD is observed which does not appear in the microscope image, the device can be turned off and scrutinized using non-destructive methods such as scanning electron microscopy.

6.2.2 Thermoreflectance imaging of diode laser cavity through the substrate

In the current work, we have captured thermoreflectance images of diode laser facets under a wide range of operating conditions. However, these images only provide information regarding the out-coupling facet. The parts of the device near the facet in the cavity are expected to be a dynamic environment for defect generation and migration. Moreover, as the facets become more robust to damage through passivation technologies, understanding catastrophic damage that occurs in the

bulk of the device becomes increasingly important. As such, thermal imaging of the diode laser cavity will provide a wealth of information regarding bulk device degradation mechanisms and non-linear processes inherent to the device. In order to carry out such testing, thermoreflectance imaging would need to be performed through the metal contacts and the GaAs substrate. Windows can be opened up in the metal contact to allow for cavity imaging. An illumination wavelength to which GaAs is transparent ($>$ 1000 nm) can be used to image the cavity through the substrate. Confocal microscopy-based approaches, combined with lock-in amplification can allow rejection of parasitic reflections from the air/substrate interface, while enabling high resolution thermal imaging of the cavity which will provide insights into the dynamics of defect formation, migration and accumulation.

BIBLIOGRAPHY

[1] Steele, R. V., "The story of a new light source," *Nature photonics*, Vol. 1, No. 1, 2007, pp. 25–26.

[2] Pryde, J. R., Whalley, D. C., and Malalasekera, W., "A review of LED technology trends and relevant thermal management strategies," *Fourteenth Intersociety Conference on Thermal and Thermomechanical Phenomena in Electronic Systems (ITherm)*, IEEE, 2014, pp. 31–38.

[3] Wijeyasinghe, N., "Laser Diodes & Direct Diode Lasers 2019-2029: Technologies, Markets & Forecasts," https://www.idtechex.com/en/research-article/direct-diode-lasers-how-technology-evolution-is-opening-new-markets/17627, 2019, [Online].

[4] Titkov, I. E., Karpov, S. Y., Yadav, A., Zerova, V. L., Zulonas, M., Galler, B., Strassburg, M., Pietzonka, I., Lugauer, H.-J., and Rafailov, E. U., "Temperature-dependent internal quantum efficiency of blue high-brightness light-emitting diodes," *IEEE Journal of Quantum Electronics*, Vol. 50, No. 11, 2014, pp. 911–920.

[5] Tomm, J. W., Ziegler, M., Hempel, M., and Elsaesser, T., "Mechanisms and fast kinetics of the catastrophic optical damage (COD) in GaAs-based diode lasers," *Laser & Photonics Reviews*, Vol. 5, No. 3, 2011, pp. 422–441.

[6] Mills, G., Zhou, H., Midha, A., Donaldson, L., and Weaver, J., "Scanning thermal microscopy using batch fabricated thermocouple probes," *Applied physics letters*, Vol. 72, No. 22, 1998, pp. 2900–2902.

[7] Xie, Z., Han, L., Wei, F., Wang, X., Gu, Y., and Chen, H., "An application of scanning thermal microscopy: mapping near field light-emission of a QW laser diode in operation," *Materials Science and Engineering: A*, Vol. 292, No. 2, 2000, pp. 179–182.

[8] Pacific, S., "PCB Thermal Infrared Analysis," https://www.x20.org/pcb-thermal-infrared-analysis-image-128/, 2014, [Online].

[9] Katz, N., Arango, A., and Hudgings, J., "Mapping Temperature in OLED Displays Using CCD Thermoreflectance," *IEEE Photonics Technology Letters*, Vol. 26, No. 2, 2013, pp. 194–197.

[10] Pierścińska, D., Pierściński, K., Morawiec, M., Karbownik, P., Gutowski, P., and Bugajski, M., "CCD thermoreflectance spectroscopy as a tool for thermal characterization of quantum cascade lasers," *Semiconductor Science and Technology*, Vol. 31, No. 11, 2016, pp. 115006.

[11] Maize, K., Heller, E., Dorsey, D., and Shakouri, A., "Thermoreflectance CCD imaging of self heating in AlGaN/GaN high electron mobility power transistors at high drain voltage," *2012 28th Annual IEEE Semiconductor Thermal Measurement and Management Symposium (SEMI-THERM)*, IEEE, 2012, pp. 173–181.

[12] Leonhäuser, B., Kissel, H., Unger, A., Köhler, B., and Biesenbach, J., "Feedback-induced catastrophic optical mirror damage (COMD) on 976nm broad area single emitters with different AR reflectivity," *High-Power Diode Laser Technology and Applications XII*, Vol. 8965, International Society for Optics and Photonics, 2014, p. 896506.

[13] Leisher, P. O., Li, C., Jha, A. K., Pipe, K. P., Helmrich, J. D., Thiagarajan, P., Boisselle, M. C., Patra, S. K., Sezgin, S., and Deri, R. J., "Feedback-induced failure of high-power diode lasers," *IEEE Journal of Quantum Electronics*, Vol. 54, No. 6, 2018, pp. 1–13.

[14] Li, C., *Thermal Management of Electronics and Optoelectronics: From Heat Source Characterization to Heat Mitigation at the Device and Package Levels*, Ph.D. thesis, 2019.

[15] Kasap, S. and Capper, P., *Springer handbook of electronic and photonic materials*, Springer, 2017.

[16] Crawford, M. H., "LEDs for solid-state lighting: performance challenges and recent advances," *IEEE Journal of Selected Topics in Quantum Electronics*, Vol. 15, No. 4, 2009, pp. 1028–1040.

[17] Kaifuchi, Y., Yoshida, K., Yamagata, Y., Nogawa, R., Yamada, Y., and Yamaguchi, M., "Enhanced power conversion efficiency in 900-nm range single emitter broad stripe laser diodes maintaining high power operability," *High-Power Diode Laser Technology XVII*, Vol. 10900, International Society for Optics and Photonics, 2019, p. 109000F.

[18] David, A., Young, N. G., Hurni, C. A., and Craven, M. D., "Quantum efficiency of III-nitride emitters: Evidence for defect-assisted nonradiative recombination and its effect on the green gap," *Physical Review Applied*, Vol. 11, No. 3, 2019, pp. 031001.

[19] Cho, J., Schubert, E. F., and Kim, J. K., "Efficiency droop in light-emitting diodes: Challenges and countermeasures," *Laser & Photonics Reviews*, Vol. 7, No. 3, 2013, pp. 408–421.

[20] Wenzel, H., Crump, P., Pietrzak, A., Wang, X., Erbert, G., and Tränkle, G., "Theoretical and experimental investigations of the limits to the maximum output power of laser diodes," *New Journal of Physics*, Vol. 12, No. 8, 2010, pp. 085007.

[21] Crump, P., Blume, G., Paschke, K., Staske, R., Pietrzak, A., Zeimer, U., Einfeldt, S., Ginolas, A., Bugge, F., Häusler, K., et al., "20W continuous wave reliable operation of 980nm broad-area single emitter diode lasers with an aperture of 96um," *High-Power Diode Laser Technology and Applications VII*, Vol. 7198, International Society for Optics and Photonics, 2009, p. 719814.

[22] Fujiwara, K., Jimi, H., and Kaneda, K., "Temperature-dependent droop of electroluminescence efficiency in blue (In, Ga) N quantum-well diodes," *physica status solidi c*, Vol. 6, No. S2 2, 2009, pp. S814–S817.

[23] Hader, J., Moloney, J. V., and Koch, S. W., "Temperature-dependence of the internal efficiency droop in GaN-based diodes," *Applied Physics Letters*, Vol. 99, No. 18, 2011, pp. 181127.

[24] Galler, B., Drechsel, P., Monnard, R., Rode, P., Stauss, P., Froehlich, S., Bergbauer, W., Binder, M., Sabathil, M., Hahn, B., et al., "Influence of indium content and temperature on Auger-like recombination in InGaN quantum wells grown on (111) silicon substrates," *Applied Physics Letters*, Vol. 101, No. 13, 2012, pp. 131111.

[25] Rattunde, M., Mermelstein, C., Schmitz, J., Kiefer, R., Pletschen, W., Walther, M., and Wagner, J., "Comprehensive modeling of the electro-optical-thermal behavior of (AlGaIn)(AsSb)-based 2.0 μm diode lasers," *Applied Physics Letters*, Vol. 80, No. 22, 2002, pp. 4085–4087.

[26] Coldren, L. A., Corzine, S. W., and Mashanovitch, M. L., *Diode lasers and photonic integrated circuits*, Vol. 218, John Wiley & Sons, 2012.

[27] Kaul, T., Erbert, G., Klehr, A., Maaßdorf, A., Martin, D., and Crump, P., "Impact of carrier nonpinning effect on thermal power saturation in GaAs-based high power diode lasers," *IEEE Journal of Selected Topics in Quantum Electronics*, Vol. 25, No. 6, 2019, pp. 1–10.

[28] Avrutin, E. A. and Ryvkin, B. S., "Effect of spatial hole burning on output characteristics of high power edge emitting semiconductor lasers: A universal analytical estimate and numerical analysis," *Journal of Applied Physics*, Vol. 125, No. 2, 2019, pp. 023108.

[29] De Loach, B., Hakki, B., Hartman, R., and D'asaro, L., "Degradation of CW GaAs double-heterojunction lasers at 300 K," *Proceedings of the IEEE*, Vol. 61, No. 7, 1973, pp. 1042–1044.

[30] Petroff, P. and Hartman, R., "Defect structure introduced during operation of heterojunction GaAs lasers," *Applied Physics Letters*, Vol. 23, No. 8, 1973, pp. 469–471.

[31] Yuasa, T., Ogawa, M., Endo, K., and Yonezu, H., "Degradation of (AlGa) As DH lasers due to facet oxidation," *Applied Physics Letters*, Vol. 32, No. 2, 1978, pp. 119–121.

[32] Kressel, H. and Ladany, I., "Reliability aspects and facet damage in high-power emission from (AlGa) As cw laser diodes at room temperature," *RCA Review*, Vol. 36, No. 2, 1975, pp. 230–239.

[33] Pierścińska, D., "Thermoreflectance spectroscopy—Analysis of thermal processes in semiconductor lasers," *Journal of Physics D: Applied Physics*, Vol. 51, No. 1, 2017, pp. 013001.

[34] Jiménez, J., "Laser diode reliability: crystal defects and degradation modes," *Comptes Rendus Physique*, Vol. 4, No. 6, 2003, pp. 663–673.

[35] O'hara, S., Hutchinson, P., and Dobson, P., "The origin of dislocation climb during laser operation," *Applied Physics Letters*, Vol. 30, No. 8, 1977, pp. 368–371.

[36] Hopgood, A., "Vacancy-controlled model of degradation in InGaAs/AlGaAs/GaAs heterostructure lasers," *Journal of applied physics*, Vol. 76, No. 7, 1994, pp. 4068–4071.

[37] Tomm, J. W. and Jimenez, J., *Quantum-Well Laser Array Packaging: Nanoscale Pckaging Techniques*, McGraw Hill Professional, 2007.

[38] Nakano, K. and Ishibashi, A., "Degradation in II-VI laser diodes," *Materials Science Forum*, Vol. 258, Trans Tech Publ, 1997, pp. 1329–1334.

[39] Weeks, J. D., Tully, J. C., and Kimerling, L., "Theory of recombination-enhanced defect reactions in semiconductors," *Physical Review B*, Vol. 12, No. 8, 1975, pp. 3286.

[40] Kimerling, L., "Recombination enhanced defect reactions," *Solid-State Electronics*, Vol. 21, No. 11-12, 1978, pp. 1391–1401.

[41] Kressel, H. and Mierop, H., "Catastrophic degradation in GaAs injection lasers," *Journal of Applied Physics*, Vol. 38, No. 13, 1967, pp. 5419–5421.

[42] Eliseev, P. G., "Optical strength of semiconductor laser materials," *Progress in quantum electronics*, Vol. 20, No. 1, 1996, pp. 1–82.

[43] Zhang, Q., Xiong, Y., An, H., Boucke, K., and Treusch, G., "Unveiling laser diode "fossil" and the dynamic analysis for heliotropic growth of catastrophic optical damage in high power laser diodes," *Scientific reports*, Vol. 6, No. 1, 2016, pp. 1–12.

[44] Henry, C., Petroff, P., Logan, R., and Merritt, F., "Catastrophic damage of Al x Ga1- x As double-heterostructure laser material," *Journal of applied physics*, Vol. 50, No. 5, 1979, pp. 3721–3732.

[45] Tang, W., Rosen, H., Vettiger, P., and Webb, D., "Raman microprobe study of the time development of AlGaAs single quantum well laser facet temperature on route to catastrophic breakdown," *Applied physics letters*, Vol. 58, No. 6, 1991, pp. 557–559.

[46] Ziegler, M., Talalaev, V., Tomm, J. W., Elsaesser, T., Ressel, P., Sumpf, B., and Erbert, G., "Surface recombination and facet heating in high-power diode lasers," *Applied Physics Letters*, Vol. 92, No. 20, 2008, pp. 203506.

[47] Tang, W., Rosen, H., Vettiger, P., and Webb, D., "Evidence for current-density-induced heating of AlGaAs single-quantum-well laser facets," *Applied physics letters*, Vol. 59, No. 9, 1991, pp. 1005–1007.

[48] Moser, A., Latta, E.-E., and Webb, D., "Thermodynamics approach to catastrophic optical mirror damage of AlGaAs single quantum well lasers," *Applied physics letters*, Vol. 55, No. 12, 1989, pp. 1152–1154.

[49] Ueda, O., "Device-Degradation in III-V Semiconductor Lasers and Led's—Influence of Defects on the Degradation—," *MRS Online Proceedings Library Archive*, Vol. 184, 1990.

[50] Hashimoto, J.-i., Yoshida, I., Murata, M., and Katsuyama, T., "Aging time dependence of catastrophic optical damage (COD) failure of a 0.98-/spl mu/m GaInAs-GaInP strained quantum-well laser," *IEEE journal of quantum electronics*, Vol. 33, No. 1, 1997, pp. 66–70.

[51] Fukushima, T., Furuya, A., Kito, Y., Sudo, H., Sugano, M., and Tanahashi, T., "Catastrophic optical damage of algalnp visible laser diodes under high-power operation," *Electronics and Communications in Japan (Part II: Electronics)*, Vol. 78, No. 7, 1995, pp. 11–19.

[52] Shi, L., Kwon, O., Miner, A. C., and Majumdar, A., "Design and batch fabrication of probes for sub-100 nm scanning thermal microscopy," *Journal of Microelectromechanical systems*, Vol. 10, No. 3, 2001, pp. 370–378.

[53] Marone, M. and Payne, J., "An ac microcalorimeter employing a diode laser as a heater," *Review of scientific instruments*, Vol. 68, No. 12, 1997, pp. 4516–4520.

[54] Luo, K., Herrick, R., Majumdar, A., and Petroff, P., "Scanning thermal microscopy of a vertical-cavity surface-emitting laser," *Applied Physics Letters*, Vol. 71, No. 12, 1997, pp. 1604–1606.

[55] Zhou, J. and Shi, L., "Scanning thermal microscopy of carbon nanotube electronic devices," *Semiconductor Thermal Measurement and Management IEEE Twenty First Annual IEEE Symposium, 2005.*, IEEE, 2005, pp. 303–306.

[56] Fiege, G., Niedernostheide, F.-J., Schulze, H.-J., Barthelmeß, R., and Balk, L., "Thermal characterization of power devices by scanning thermal microscopy techniques," *Microelectronics reliability*, Vol. 39, No. 6-7, 1999, pp. 1149–1152.

[57] Ziegler, M., Tomm, J. W., Elsaesser, T., Matthiesen, C., Bou Sanayeh, M., and Brick, P., "Real-time thermal imaging of catastrophic optical damage in red-emitting high-power diode lasers," *Applied Physics Letters*, Vol. 92, No. 10, 2008, pp. 103514.

[58] Epperlein, P., Bona, G., and Roentgen, P., "Local mirror temperatures of red-emitting (Al) GaInP quantum-well laser diodes by Raman scattering and reflectance modulation measurements," *Applied physics letters*, Vol. 60, No. 6, 1992, pp. 680–682.

[59] Brugger, H. and Epperlein, P. W., "Mapping of local temperatures on mirrors of GaAs/AlGaAs laser diodes," *Applied Physics Letters*, Vol. 56, No. 11, 1990, pp. 1049–1051.

[60] Puchert, R., Tomm, J., Jaeger, A., Bärwolff, A., Luft, J., and Späth, W., "Emitter failure and thermal facet load in high-power laser diode arrays." *Applied Physics A: Materials Science & Processing*, Vol. 66, No. 5, 1998.

[61] Epperlein, P. and Bona, G., "Influence of the vertical structure on the mirror facet temperatures of visible GaInP quantum well lasers," *Applied physics letters*, Vol. 62, No. 24, 1993, pp. 3074–3076.

[62] Schaub, E., "Optical absorption rate determination, on the front facet of high-power GaAs laser diodes, by means of thermoreflectance technique," *Japanese Journal of Applied Physics*, Vol. 40, No. 4S, 2001, pp. 2752.

[63] Ezzahri, Y., Dilhaire, S., Grauby, S., Rampnoux, J.-M., Claeys, W., Zhang, Y., Zeng, G., and Shakouri, A., "Study of thermomechanical properties of Si/ Si Ge superlattices using femtosecond transient thermoreflectance technique," *Applied Physics Letters*, Vol. 87, No. 10, 2005, pp. 103506.

[64] Paddock, C. A. and Eesley, G. L., "Transient thermoreflectance from thin metal films," *Journal of applied physics*, Vol. 60, No. 1, 1986, pp. 285–290.

[65] Smith, A. N. and Norris, P. M., "Influence of intraband transitions on the electron thermoreflectance response of metals," *Applied Physics Letters*, Vol. 78, No. 9, 2001, pp. 1240–1242.

[66] Stevens, R. J., Smith, A. N., and Norris, P. M., "Measurement of thermal boundary conductance of a series of metal-dielectric interfaces by the transient thermoreflectance technique," *J. Heat Transfer*, Vol. 127, No. 3, 2005, pp. 315–322.

[67] Varshni, Y. P., "Temperature dependence of the energy gap in semiconductors," *physica*, Vol. 34, No. 1, 1967, pp. 149–154.

[68] Pankove, J. I., *Optical processes in semiconductors*, Courier Corporation, 1975.

[69] Ozaki, S. and Adachi, S., "Spectroscopic ellipsometry and thermoreflectance of GaAs," *Journal of applied physics*, Vol. 78, No. 5, 1995, pp. 3380–3386.

[70] Farzaneh, M., Maize, K., Lüerßen, D., Summers, J., Mayer, P., Raad, P., Pipe, K., Shakouri, A., Ram, R., and Hudgings, J. A., "CCD-based thermoreflectance microscopy: principles and applications," *Journal of Physics D: Applied Physics*, Vol. 42, No. 14, 2009, pp. 143001.

[71] Williams, E., Bebb, H. B., et al., "Semiconductors and semimetals," *RK Willardson ed*, Vol. 8, 1972, pp. 336.

[72] Dilhaire, S., Grauby, S., and Claeys, W., "Thermoreflectance calibration procedure on a laser diode: Application to catastrophic optical facet damage analysis," *IEEE electron device letters*, Vol. 26, No. 7, 2005, pp. 461–463.

[73] Luerssen, D., Hudgings, J. A., Mayer, P. M., and Ram, R. J., "Nanoscale thermoreflectance with 10mK temperature resolution using stochastic resonance," *Semiconductor Thermal Measurement and Management IEEE Twenty First Annual IEEE Symposium, 2005.*, IEEE, 2005, pp. 253–258.

[74] Chan, P., Pipe, K., Mi, Z., Yang, J., Bhattacharya, P., and Lüerßen, D., "Thermal relaxation time and heat distribution in pulsed InGaAs quantum dot lasers," *Applied physics letters*, Vol. 89, No. 1, 2006, pp. 011110.

[75] Cahill, D. G., "Analysis of heat flow in layered structures for time-domain thermoreflectance," *Review of scientific instruments*, Vol. 75, No. 12, 2004, pp. 5119–5122.

[76] Minnich, A. J., Johnson, J. A., Schmidt, A. J., Esfarjani, K., Dresselhaus, M. S., Nelson, K. A., and Chen, G., "Thermal conductivity spectroscopy technique to measure phonon mean free paths," *Physical review letters*, Vol. 107, No. 9, 2011, pp. 095901.

[77] Regner, K. T., Sellan, D. P., Su, Z., Amon, C. H., McGaughey, A. J., and Malen, J. A., "Broadband phonon mean free path contributions to thermal conductivity measured using frequency domain thermoreflectance," *Nature communications*, Vol. 4, No. 1, 2013, pp. 1–7.

[78] Madrid-Wolff, J. and Forero-Shelton, M., "4f Koehler Transmitted Illumination Condenser for Teaching and Low-Cost Microscopic Imaging," *The Biophysicist*, Vol. 1, No. 2, 2020.

[79] Pfeiffer, H.-U., Arlt, S., Jacob, M., Harder, C. S., Jung, I. D., Wilson, F., Oldroyd, T., and Hext, T., "Reliability of 980 nm pump lasers for submarine, long-haul terrestrial, and low cost metro applications," *Optical Fiber Communication Conference*, Optical Society of America, 2002, p. ThN4.

[80] Takeda, A., Shogenji, R., and Ohtsubo, J., "Dynamics and pulse-package oscillations in broad-area semiconductor lasers with short optical feedback," *Applied Physics Letters*, Vol. 101, No. 23, 2012, pp. 231105.

[81] Tachikawa, T., Shogenji, R., and Ohtsubo, J., "Observation of multi-path interference in broad-area semiconductor lasers with optical feedback," *Optical review*, Vol. 16, No. 5, 2009, pp. 533–539.

[82] Leonhäuser, B., Kissel, H., Tomm, J. W., Hempel, M., Unger, A., and Biesenbach, J., "High-power diode lasers under external optical feedback," *High-Power Diode Laser Technology and Applications XIII*, Vol. 9348, International Society for Optics and Photonics, 2015, p. 93480M.

[83] Takiguchi, Y., Asatsuma, T., and Hirata, S., "Effect of the threshold reduction on a catastrophic optical mirror damage in broad-area semiconductor lasers with optical feedback," *High-Power Diode Laser Technology and Applications IV*, Vol. 6104, International Society for Optics and Photonics, 2006, p. 61040X.

[84] Hempel, M., Chi, M., Petersen, P. M., Zeimer, U., and Tomm, J. W., "How does external feedback cause AlGaAs-based diode lasers to degrade?" *Applied Physics Letters*, Vol. 102, No. 2, 2013, pp. 023502.

[85] Leisher, P. O., Pope, D., Platz, L., Boisselle, M., Runkel, M., Deri, R. J., Smith, S., Helmrich, J. D., Crawford, D. E., Thiagarajan, P., et al., "Root cause investigation of back-irradiance-induced failure of high power diode lasers," *2017 IEEE High Power Diode Lasers and Systems Conference (HPD)*, IEEE, 2017, pp. 53–54.

[86] Rauch, S., Holly, C., and Zimer, H., "Catastrophic optical damage in 950-nm broad-area laser diodes due to misaligned optical feedback and injection," *IEEE Journal of Quantum Electronics*, Vol. 54, No. 4, 2018, pp. 1–7.

[87] Epperlein, P.-W., "Micro-temperature measurements on semiconductor laser mirrors by reflectance modulation: A newly developed technique for laser characterization," *Japanese journal of applied physics*, Vol. 32, No. 12R, 1993, pp. 5514.

[88] Mansanares, A., Roger, J., Fournier, D., and Boccara, A., "Temperature field determination of InGaAsP/InP lasers by photothermal microscopy: Evidence for weak nonradiative processes at the facets," *Applied physics letters*, Vol. 64, No. 1, 1994, pp. 4–6.

[89] Lambert, R. W., Ayling, T., Hendry, A. F., Carson, J. M., Barrow, D. A., McHendry, S., Scott, C. J., McKee, A., and Meredith, W., "Facet-passivation processes for the improvement of Al-containing semiconductor laser diodes," *Journal of lightwave technology*, Vol. 24, No. 2, 2006, pp. 956.